



저작자표시-비영리-변경금지 2.0 대한민국

이용자는 아래의 조건을 따르는 경우에 한하여 자유롭게

- 이 저작물을 복제, 배포, 전송, 전시, 공연 및 방송할 수 있습니다.

다음과 같은 조건을 따라야 합니다:



저작자표시. 귀하는 원저작자를 표시하여야 합니다.



비영리. 귀하는 이 저작물을 영리 목적으로 이용할 수 없습니다.



변경금지. 귀하는 이 저작물을 개작, 변형 또는 가공할 수 없습니다.

- 귀하는, 이 저작물의 재이용이나 배포의 경우, 이 저작물에 적용된 이용허락조건을 명확하게 나타내어야 합니다.
- 저작권자로부터 별도의 허가를 받으면 이러한 조건들은 적용되지 않습니다.

저작권법에 따른 이용자의 권리는 위의 내용에 의하여 영향을 받지 않습니다.

이것은 [이용허락규약\(Legal Code\)](#)을 이해하기 쉽게 요약한 것입니다.

[Disclaimer](#)

Ph.D. DISSERTATION

**Developing the bi-layered Self-rectifying Resistive
Switching Device and Improving Resistive Switching
Parameters for ReRAM Applications**

by

Jung Ho Yoon

February 2015

DEPARTMENT OF MATERIALS SCIENCE AND ENGINEERING

COLLEGE OF ENGINEERING

SEOUL NATIONAL UNIVERSITY

ABSTRACT

Resistance switching random access memory (ReRAM) is attracting a great deal of attention as one of the most promising next-generation non-volatile memory devices due to its exclusive properties like scalability, low cost, fast operation speed and simple structure. Although there have been huge improvements in the development of ReRAM during the past decade, there are still several key concerns remaining with RS materials. There are two most important problems. One is the non-uniformity problem of the switching performance and the other is the necessity of unprecedented concept ReRAM structure which is suitable for the 3D type planar or vertical CBA structure device.

Among the research part of ReRAM, the understanding of resistance switching (RS) mechanisms in many oxide materials and its application to ReRAM have been greatly improved over the last decade. This has mainly been attributed to the improvement in the device fabrication methods and application of various state-of-the-art analysis techniques. In ionic type RS switching phenomena, while there are detailed variations in the nature, shape, electrical properties, and distribution across the RS layer, the RS behaviors of many RS materials are closely related to the presence of nano-scale conducting filament (CF), where the repeated formation and rupture of CFs are controlled by the thermally-assisted electromigration of defects, mainly

oxygen vacancies in oxides. The inappropriate repeatability of the RS parameters and low reliability issue are material-property-related problems especially originated from the random formation of CFs. The non-uniform RS performance with the increasing number of RS cycles or memory cells is generally related to the non-uniform and uncontrolled formation and rupture of CFs over a large area of the memory cell, which are caused by their random nucleation and uncontrolled growth. This suggests that confining the location where the CFs form to a certain region of the memory cell would improve the repeatability problem. In this work, as for the solution of non-uniformity problem, Ru-nanodots (Ru-NDs) are embedded in TiO₂ which is the most representative resistance switching film, which essentially eliminates concerns with non-uniformity. It was concluded that limiting the location where the electron injection occurs at the cathode interface to a narrower region was the key factor for achieving the highly improved RS performance, while the phases of TiO₂ can hardly influence the RS performances. The position of the Ru-NDs relative to the cathode played an important role in limiting the field concentration area to a narrow region.

In the crossbar array (CBA) configuration, it currently has several obstacles to overcome, such as the high variability in electrical performances, the requirement of an electroforming step, and the necessary integration of a memory cell with selector devices to alleviate the sneak currents in CBA. These problems become even more serious when a three-dimensional (vertical) CBA structure is to be fabricated. In this respect, the development of RS

memory cell which contains rectification functionality in itself, highly reproducible RS performance, multi-level functionality, and electroforming-free characteristics are the impending tasks for development of ReRAM. In this work, two-layered dielectric structure consisted with HfO₂ and Ta₂O₅ layer which are in contact with the TiN, Ti and Pt electrode is presented for achieving these tasks simultaneously in one sample configuration. HfO₂ layer works as the resistance switching layer by trapping or detrapping of electronic carriers, while Ta₂O₅ layer remained intact during the whole switching cycle, which provides the rectification. With the optimized structure and operation conditions for the given materials, excellent RS uniformity, electroforming-free and self-rectifying functionality could be simultaneously achieved from the Pt/Ta₂O₅/HfO₂/TiN and Pt/Ta₂O₅/HfO₂/TiN structure.

Keywords: Resistive Switching Random Access Memory, Uniformity, Ru Nano-dots, Self-rectification, Electroforming-free, Multi level switching
Student Number: 2010-20619

Jung Ho Yoon

CONTENTS

Abstract	i
Contents	v
List of Figures	ix
1. Introduction.....	1
1.1. Overview of resistive switching phenomena	1
1.2. Technical issues of resistive switching memory	6
1.3. Research scope and objective	12
1.4. Bibliography	13
2. Improving Uniformity in the Resistive Switching Parameters of TiO ₂ Thin Films by Inserting Ru Nano-Dots[1]	15
2.1. Introduction.....	15
2.2. Experiment.....	18
2.3. Structural Properties of Pt/TiO ₂ /Pt Resistive Switching Cell with Ru Nano-Dots	19
2.4. Electrical Performances of the Memory Cell and Switching Mechanism.....	26
2.5. Summary	56
2.6. Bibliography	56

3.	Self-rectifying Resistive Switching Phenomena in Pt/Ta ₂ O ₅ /HfO ₂ /TiN structure[2]	59
3.1.	Introduction.....	59
3.2.	Experiment.....	63
3.3.	Structural Properties of the Ta ₂ O ₅ /HfO ₂ /TiN Thin-Film Stack	65
3.4.	Electrical Performances of the Memory Cell and Switching Mechanism.....	71
3.5.	Summary	102
3.6.	Bibliography	103
4.	Self-rectifying Resistive Switching Phenomena in Pt/Ta ₂ O ₅ /HfO ₂ /Ti structure	109
4.1.	Introduction.....	109
4.2.	Experiment.....	112
4.3.	Structural Properties of the Ta ₂ O ₅ /HfO ₂ /Ti Thin-Film Stack	113
4.4.	Electrical Performance of the Memory Cell	122
4.5.	Switching Mechanism of the Memory Cell	134
4.6.	Summary	144
4.7.	Bibliography	145
5.	Conclusions.....	147

Curriculum Vitae	151
List of publications	158
Abstract (in Korean).....	171

- [1] **Jung Ho Yoon**, Jeong Hwan Han, Ji Sim Jung, Woojin Jeon, Gun Hwan Kim, Seul Ji Song, Jun Yeong Seok, Kyung Jean Yoon, Min Hwan Lee and Cheol Seong Hwang, "Highly Improved Uniformity in the Resistive Switching Parameters of TiO₂ Thin Films by Inserting Ru Nanodots", *Adv. Mat.*, 25, 1987-1992 (2013)
- [2] **Jung Ho Yoon**, Seul Ji Song, Il-Hyuk Yoo, Jun Yeong Seok, Kyung Jean Yoon, Dae Eun Kwon, Tae Hyung Park and Cheol Seong Hwang, "Highly Uniform, Electroforming-Free, and Self-Rectifying Resistive Memory in the Pt/Ta₂O₅/HfO_{2-x}/TiN Structure", *Adv. Funct. Mat.*, 24, 5086–5095 (2014)

LIST OF FIGURES

Figure 1. 1. Classification of resistive switching mechanism	4
Figure 1. 2. The general switching operation schemes of (a) URS and (b) BRS	5
Figure 1. 3. Expected ReRAM position and required memory specs of each type of memry	9
Figure 1. 4. The storage capacity of NAND flash and several next-generation new memory	10
Figure 1. 5. Direction of development of the ultra high density memory	10
Figure 1. 6. Direction of development of the ReRAM structure concept	11
Figure 2. 1. (a) Layer density depending on the Ru ALD cycles and the surface morphology over $1\mu\text{m} \times 1\mu\text{m}$ area of (b) 150, (c) 200 (c), and (d) 250 Ru ALD cycles.....	21
Figure 2. 2. X-ray diffraction patterns of n-Ru and b-Ru (150cy, 200cy, and 250cy) samples.....	22
Figure 2. 3. HRTEM images of n-Ru (a) before and (b) after electro-forming process. HRTEM images of (c) formation of an elliptical shaped Ru nanodots and (d) conducting filament formed on the Ru nanodot in b-Ru. (e) Lower and (f) higher magnification TEM images of the t-Ru sample.	25
Figure 2. 4. The cumulative probability graphs of high resistance state (HRS) current, the set voltage, the reset power, respectively, for the n-Ru,	

b-Ru (a) ~ (d), and t-Ru (e) ~ (h) samples with nRu of 150, 200, and 250 when the cell size is $\sim 60,000\mu\text{m}^2$. The sample structure of b-Ru (inset figure of (c)) and t-Ru (inset figure of (g))..... 28

Figure 2. 5. Current-voltage (I-V) curves of unipolar resistive switching of the

(a) n-Ru, b-Ru (b) ~ (d), and t-Ru (f) ~ (h) samples with nRu of 150, 200, and 250 when the cell size is $\sim 60,000\mu\text{m}^2$. (e) Schematic image of the measurement system of this device 29

Figure 2. 6. The cumulative probability graphs of high resistance state (HRS)

current, the set voltage, the reset power, respectively, for the n-Ru, b-Ru (nRu = 150) (a) ~ (d), and t-Ru (nRu = 250) (e) ~ (h) samples when cell sizes are $2 \times 2 \sim 10 \times 10 \mu\text{m}^2$. Area dependency of resistance in HRS and LRS (inset figure of (c)) and the morphology of crossbar type sample (inset figure of (f))..... 32

Figure 2. 7. Variation of resistance values in HRS and LRS with the switching

cycle number of the n-Ru, b-Ru (nRu = 150), and t-Ru (nRu = 250) 33

Figure 2. 8. (a) The digitized topographic images of the t-Ru samples with

nRu of 150 (left), 200 (middle), and 250 (right), and (b) the corresponding local current images. (c) The high-resolution overlapped topographic and current images of t-Ru250 in (a) and (b). (d) The schematic diagram of the bias application, and electric field distribution across the cross-section of the film containing one Ru-ND for this CAFM experiment..... 36

Figure 2. 9. Original topographical and unfiltered CAFM images shown in

figure 2.8	37
Figure 2. 10. Three-dimensional image of CAFM of the figure 2.8 (b).....	38
Figure 2. 11. (a) The digitized topographic images of the b-Ru samples with nRu of 150 (left), 200 (middle), and 250 (right), and (b) the corresponding local current images. (c) The high-resolution overlapped topographic and current images of b-Ru250 in (a) and (b). The schematic diagram of the bias application, and electric field distribution across the cross-section of the film containing one Ru-ND for this CAFM experiment.....	41
Figure 2. 12. Original topographical and unfiltered CAFM images shown in figure 2.11	42
Figure 2. 13. The electric field distribution of (a) b-Ru and (b) t-Ru samples having the density of Ru nano-dots with 20 dots/ μm^2 and 80 dots/ μm^2 . The field distribution along the bottom interface (marked by the yellow band in the figures) is highlighted in the low panels of each figure. Inset figures of (a) and (b) show electric field distribution near one Ru nano-dot.....	46
Figure 2. 14. The electric field distribution of (a) b-Ru and (b) t-Ru samples, where the protrusion on the TiO_2 surface by the presence of embedded Ru ND was considered or not. The field distribution along the bottom interface (marked by the yellow band in the figures) is highlighted in the lower panels of each figure. Inset figures of (a) and (b) show electric field distribution near one Ru nano-dot.....	48

Figure 2. 15. (a) The typical bipolar resistive switching behavior and (b) endurance data of n-Ru, bRu and t-Ru samples. The I-V curve of (c) b-Ru and (d) n-Ru depending on the switching cycles	50
Figure 2. 16. (a) The sample configuration for the I-V measurement and (b) schematic diagram for the oxygen movement during the electroforming with either negative or positive bias. The I-V curve of pristine state in b-Ru ((c) : negative bias, (d) – positive bias) and t-Ru ((e) : negative bias, (f) – positive bias)	52
Figure 2. 17. AFM topographic images of an n-Ru sample with a 4 x 4 μm^2 dimension (a) before and (b) after electrical forming	53
Figure 2. 18. Switching I-V curves taken from 20 different cells of (a) n-Ru, (b) b-Ru (nRu = 150), and (c) t-Ru (nRu = 250) samples with the large capacitor type	55
Figure 3. 1. (a) Cross-section TEM images and (b) depth profiling AES data of the Pt/Ta ₂ O ₅ (10nm)/HfO ₂ (10nm)/TiN sample	68
Figure 3. 2. (a) Ta 4f/ Hf 4f, (b) O 1s, (c) N 1s and (d) Ti 2p core levels in the XPS depth profile results of the Ta ₂ O ₅ (5nm)/HfO ₂ (10nm)/TiN sample	70
Figure 3. 3. Resistive switching I-V curves of the (a) Pt/10-nm-thick HfO ₂ /TiN, (b) Pt/5-nm-thick Ta ₂ O ₅ /10-nm-thick HfO ₂ /TiN, (c) Pt/10-nm-thick Ta ₂ O ₅ /5-nm-thick HfO ₂ /TiN, and (d) Pt/10-nm-thick Ta ₂ O ₅ /10-nm-thick HfO ₂ /TiN samples. Schematic diagrams of the samples with (inset figure of (a)) single and (inset figure of	

(b) stacked dielectric layers. (inset figure of (d)) Resistance ratio between HRS and LRS, and rectification ratio (current ratio between the positive (LRS) and negative voltages) as a function of absolute voltage. (e) The conventional bipolar resistive switching behavior in the Pt/Ta₂O₅(10nm)/HfO₂(10nm)/TiN sample. The electroforming was initially performed in the negative bias voltage region with the typical electroforming voltage and the current levels of ~-10 V and 1 μA. This was not the desired switching operation in this work..... 76

Figure 3. 4. Exceptionally high uniformity of the RS performances within (a) one dot (300 μm diameter) up to 100 I-V sweep cycles, and (b) 20 dots in a single sample; (c) cumulative probability of the current levels of LRS and HRS in the positive and negative voltage regions at particular read voltages (6, 7, and 8 V); and (d) retention data of the LRS and HRS at room temperature and 85°C up to 10⁶s (measured at 6 V) 80

Figure 3. 5. Variations of the current level in the HRS and LRS, measured at 5, 6, and 7 V, respectively, as a function of the (a) I_{cc} during the set switching, and (b) reset voltage during the reset switching. The switching I-V curves with different (c) I_{cc} values, and (d) reset voltage 84

Figure 3. 6. (a) I-V curves of the LRS (dashed lines) and HRS (solid lines) samples measured at different temperatures ranging from 30 to 100°C. Arrhenius form (Ln I vs. 1/T) plot in (b) HRS and (c) LRS,

and (inset figures of (b) and (c)) activation energies (E_a) extracted at each voltage from the best-linear-fitting of the data in HRS and LRS 87

Figure 3. 7. P-F fitting and the plots in the form of $\ln(I/(E \cdot T^{3/2}))$ vs. $1/T$ according to the P-F equation for the voltages ranging from 5 to 6 V in (a) HRS and 5 to 8 V in (b) LRS. (Upper panels of (c)) Activation energy, corresponding to the trap depth at each voltage in HRS and LRS (left for HRS and right for LRS), and (lower panels of (d)) dielectric constant at each temperature. P-F plots in the form of $\ln(I/E)$ vs. $E^{1/2}$ according to the P-F equation in (d) HRS and (e) LRS, respectively 91

Figure 3. 8. (a) I-V curves and (b) Arrhenius form ($\ln J$ vs. $1/T$) plot under a negatively biased condition measured at different temperatures ranging from 30 to 100°C. (Inset figures of (b)) activation energies (E_a) extracted at each voltage from the best-linear-fitting of the data. (c) Schottky type form $\ln(I/T^2)$ vs. $1/T$ plot at voltages ranging from 8.3 to 8.7 V. (Inset figure of (c)) $\psi_0 - \beta_s E^{1/2}$ values plotted as a function of $E^{1/2}$ 94

Figure 3. 9. Schematic diagram showing the switching mechanism: (a) Schematic diagrams of band structure for zero bias condition (left panel figure). The bulk of HfO_2 has the 1.0eV traps, which has coincided with the energy distance between V_O from the CB edge, while local portion of HfO_2 has the 0.6eV traps in addition to the 1.0eV traps (right panel figure). (b) Under the low positive bias

(<~3V), the injected electrons transported through the hopping mechanism. (c) As the traps with 1.0eV were filled with electrons, P-F effect started to show up where the effective trap depth decreased at the higher positive bias. (d) The carrier transport could occur via P-F mechanism mediated by 0.6eV traps after the deeper trap level was fully filled with carriers and the system switched to LRS. (e) When the low negative bias was applied to system, the electrons in the HfO₂ traps were detrapped. At the same time, carrier injection from the Pt electrode was suppressed by the Schottky barrier while the electrons from all the trap sites detrapp switching back the sample to HRS. (f) Even under no bias condition, some of the electrons accumulated at the Ta₂O₅/HfO₂ interface could be transported to the empty deep traps and degrade the HRS with time especially at high temperature (85 °C)

..... 101

Figure 4. 1. (a) Cross-section TEM images and (b) depth profiling AES data of the Pt/Ta₂O₅(10nm)/HfO₂(10nm)/Ti sample 117

Figure 4. 2. (a) Ta 4*f*/ Hf 4*f*, (b) O 1*s*, (c) N 1*s* and (d) Ti 2*p* core levels in the XPS depth profile results of the Ta₂O₅(10nm)/HfO₂(10nm)/Ti sample 119

Figure 4. 3. Depth profiling atomic concentration data of (a) HfO₂/Ti and (b) HfO₂/TiN measured by MEIS 120

Figure 4. 4. SIMS data of HfO₂/Ti and HfO₂/TiN..... 121

Figure 4. 5. (a) Resistive switching I-V curves, (b) on/off and F/R ratio, (c) cumulative probabilities at LRS and HRS and (d) retention properties of the Pt/10-nm-thick Ta₂O₅/10-nm-thick HfO₂/TiN structure. (Inset figure of figure (b)) AFM image of CBA type sample and (inset figure of figure (d)) retention time vs. 1/kT graph..... 127

Figure 4. 6. I - V curves of (a) HfO₂/TiN and (b) HfO₂/Ti..... 128

Figure 4. 7. Retention data at RT of Pt/Ta₂O₅/HfO₂/Ti structure sample 129

Figure 4. 8. Conventional bipolar RS I – V graph of Pt/Ta₂O₅/HfO₂/Ti structure sample..... 130

Figure 4. 9. (a) The mean value and distribution of current level at read voltage 2V in several intermediate LRS and (b) I – V curves at each intermediate LRS. Area dependency of (c) HRS and LRS and (inset figure of (c)) intermediate LRS 134

Figure 4. 10. (a) I-V curves of the HRS samples measured at different temperatures ranging from 30 to 100°C. Arrhenius form (Ln I vs. 1/T) plot in (b) HRS, and (inset figures of (b)) activation energies (E_a) extracted at each voltage from the best-linear-fitting of the data in HRS. (c) P-F fitting and (d) the plots in the form of Ln(I/(E*T^{3/2})) vs. 1/T according to the P-F equation for the voltages ranging from 3.5 to 3.8 V in HRS. (inset figure of (c)) dielectric constant at each temperature and (inset figure of (d)) Activation energy, corresponding to the trap depth at each voltage in HRS..... 138

Figure 4. 11. (a) I-V curves of the LRS samples measured at different temperatures ranging from 50 to 90°C. Arrhenius form ($\ln I$ vs. $1/T$) plot in (b) LRS, and (inset figures of (b)) activation energies (E_a) extracted at each voltage from the best-linear-fitting of the data in LRS..... 140

Figure 4. 12. (a) I-V curves and under a negatively biased condition measured at different temperatures ranging from 110 to 150°C. (b) Schottky type form $\ln(I/T^2)$ vs. $1/T$ plot at voltages ranging from 8 to 8.5 V. (Inset figure of (c)) $\psi_0 - \beta_s E^{1/2}$ values plotted as a function of $E^{1/2}$ 143

1. Introduction

1.1. Overview of resistive switching phenomena

Modern memory technology reaches the technical limits of development of faster, denser, low energy consuming and low cost non-volatile memory (NVM).[1] Charge-based memories, such as dynamic random access memory (DRAM) and flash memory, suffers from the performance degradation as the scaling limit which includes high aspect ratio, complexity of structure, necessity of minimum charge carriers and etc. is approached.[2] To overcome the problems of current NVM concepts, a variety of alternative memory concepts is proposed. Ferroelectric random access memory (FeRAM), magnetoresistive random access memory (MRAM), phase change random access memory (PRAM) are proposed in early stage as strong candidates for next generation NVM to replace the conventional charge-based memories. However, these device has inevitable problems which are technological and inherent problems in the scalability and insufficient properties like low reliability, low speed and high power consumption. So, among the many candidates for next-generation NVM based on a non-charge memories, resistance switching random access memory (ReRAM) is attracting a great deal of attention as one of the most promising next-generation non-volatile memory devices due to its exclusive properties. Implementation of ReRAM

device and understanding of resistance switching (RS) mechanisms in many oxide materials were reported over the last decade.[3-5] Most early researches were done on the RS phenomena and mechanisms in a variety of materials like NiO, TiO₂, HfO₂, Ta₂O₅ and etc. with simple metal-insulator-metal (MIM) structure. [6-8] This has mainly been attributed to the improvement in the device fabrication ways and application of various analysis techniques. In general, ReRAM can be classified based on the physical driving force and operation method. Figure 1.1 shows the classification of resistive switching (RS) mechanism.[4] A large variety of physical driving force which induced RS phenomena are reported. First, electrochemical metallization mechanism is originated from the drift of the highly mobile Ag⁺ or Cu⁺ cations which formed through redox reaction at active electrode metal in the ion conducting insulating layer.[9] These mobile cations form a highly conductive filament when negative bias is induced at active electrode and reversibly when the reversal polarity of the voltage is applied dissolution of filament is induced. Second, phase change mechanism relies on the transition between crystalline and amorphous phase of specific material like GST (Ge_xSb_yTe_z).[10] Heat generated during operation sequence is the major driving force to induce phase change phenomena and resistance state is reversibly switchable. Third, valence change mechanism and thermo-chemical mechanism occurs in transition metal oxides and is induced by a migration of ions, such as oxygen ions.[11-13] In the valence change mechanism, the creation and electromigration of oxygen vacancies induces the distribution of the carrier

density and the valence states of cations. Thermo-chemical mechanism is highly related on the thermal effect and redox reaction in the conducting filament and electrode where active carriers are injected. Metallic filaments are formed through the insulator during the electroforming process and ruptured as a result of joule heating. Discussed mechanisms so far can be grouped into ionic type switching mechanism. Last thing is electrostatic/electronic mechanism which could be mostly attributed to the trapping and detrapping of carriers depending on the bias polarities.[14] In contrast to other ionic RS mechanisms, such electronic switching mechanisms induce no or minimal movement of ionic species. Although a large variety of RS mechanism are proposed, there are only two type of operation mode. One is unipolar resistive switching mode (URS) and the other is bipolar resistive switching mode (BRS). Figure 1.2 shows the typical current-voltage schemes in unipolar and bipolar mode of RS memory cells. In URS mode, the state can be switched with regardless of voltage polarities, whereas opposite polarities of voltage is necessary to operate BRS mode. The general switching operation schemes are indicated by the numbers included in figure 1.2. : the I-V curves of the pristine state (curve 1); the low resistance state (LRS) (curve 2), which was induced by the first voltage sweep with I_{cc} ; the resetting curve (curve 3), where the voltage was swept up or swept down in URS and BRS, respectively; the high resistance state (HRS) (curve 4), which was induced by the previous voltage sweep into the positive (URS) or negative (BRS) voltage direction, respectively; and the setting curve (curve 5) in the positive voltage region,

which set the sample to low resistance state again.

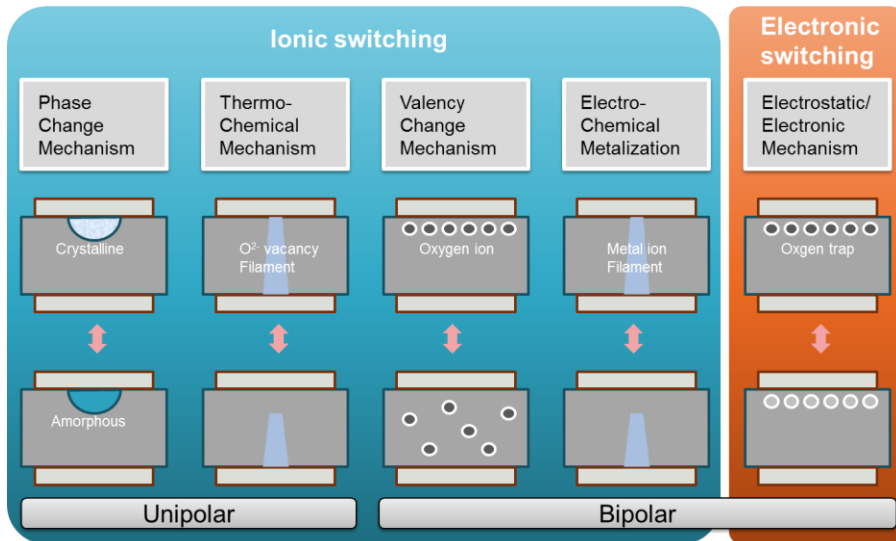


Figure 1. 1. Classification of resistive switching mechanism. [4]

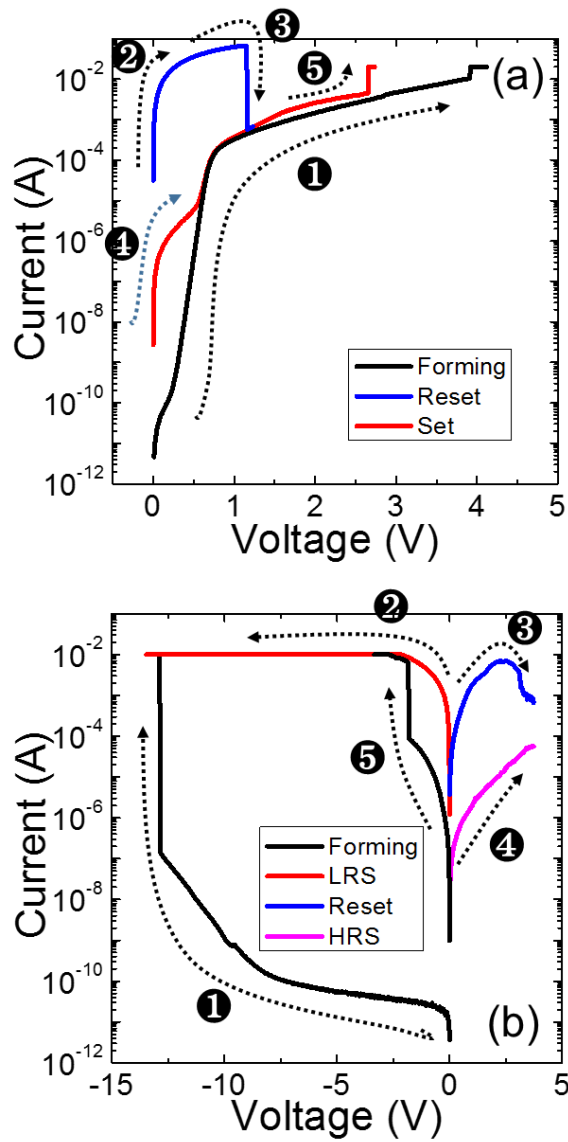


Figure 1. 2. The general switching operation schemes of (a) URS and (b) BRS

1.2. Technical issues of resistive switching memory

ReRAM is attracting a great deal of attention as one of the most promising next-generation non-volatile memory devices due to its many potential advantages like low power, fast operation speed, high density, scalability, good reliability and etc.. Figure 1.3 shows the expected ReRAM position.[15] ReRAM cell properties are satisfactory for data storage or storage class memory (SCM). Over the past 10 years, the potential of ReRAM is showing the steepest rise in the storage capacity and ReRAM is expected as a strong candidate of the successor of NAND flash. The storage capacity of NAND flash and several next-generation new memory is shown in figure 1.4.[16] As the scaling of a memory device proceeds down to the design rule of ~ 10 nm, architectures with a vertically integrated structure are attracting great interest. Figure 1.5 shows the direction of development of the ultra high density memory.[17] Although planar type NAND flash memory is currently used and produced, Toshiba Company suggested vertically aligned chains of charge-trap-flash memory cells which comprise the 3D NAND flash memory cell array in order to solve the limit of planar NAND flash memory.[18] Since the first propose of 3D type vertical NAND flash memory, variant concepts of 3D NAND have been suggested. In fact, these are the main stream of ultrahigh density memory, however these have common problems which are channel issues and limit of scalability issue. Considering the scalability, fabrication complexity and cost, perhaps 3D type planar or vertical crossbar array (CBA)

ReRAM is the only way to solve this problem. Figure 1.6 shows the most potent direction which is the way ReRAM device should go.

Before discussing about the implementation of 3D type CBA ReRAM, however, the most appropriate concept of RS cell with selector must be suggested. Many groups are struggling to develop ReRAM cell with sufficient properties and report their own results. On the other hand, since there are detailed variations in the origin, shape and electrical properties of RS layer, it is very hard work to develop an appropriate selection device considering the compatibility with the RS layer in order to apply to memory devices especially in the planar type or further vertical type CBA configuration. The fabrication of ReRAM device with discrete selector which is only suitable for the planar type CBA, such as the transistor, Schottky diode and nonlinear I – V device were reported in many groups but there is a common problem of difficulty in the vertically integration.[19-23] This problems become even more worsen when a vertical CBA structure is to be fabricated.

In addition to device integration and architecture issues, it currently has several key concerns remaining including the necessity of electroforming-step, inappropriate repeatability of the RS parameters and insufficient properties to apply memory devices especially low operation voltage, high on/off ratio, multi-level functionality and low power. Actually, the non-uniformity RS behavior while repeated RS operation is highly related to the non-uniform formation of conducting filaments (CF) or paths which is induced during electroforming step over a whole area of the memory cell. And it has been

granted that the electroforming step must be necessary in ionic type RS behavior. This suggests that random fluctuation of RS parameters in ionic type RS memory cell, such as the operation voltages and current levels at each states, are somewhat inevitable. Therefore, designing a new concept of RS memory cell or adopting new RS operation scheme are impending tasks for the further application of planar or vertical type CBA devices.

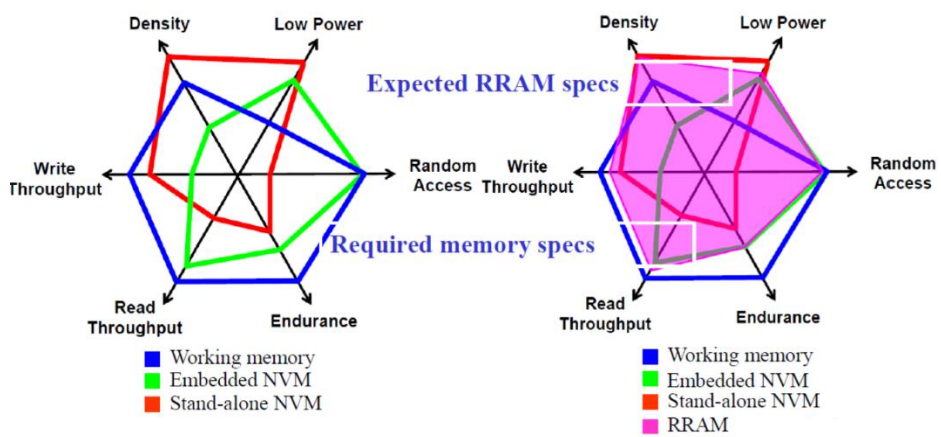


Figure 1. 3. Expected ReRAM position and required memory specs of each type of memory. [15]

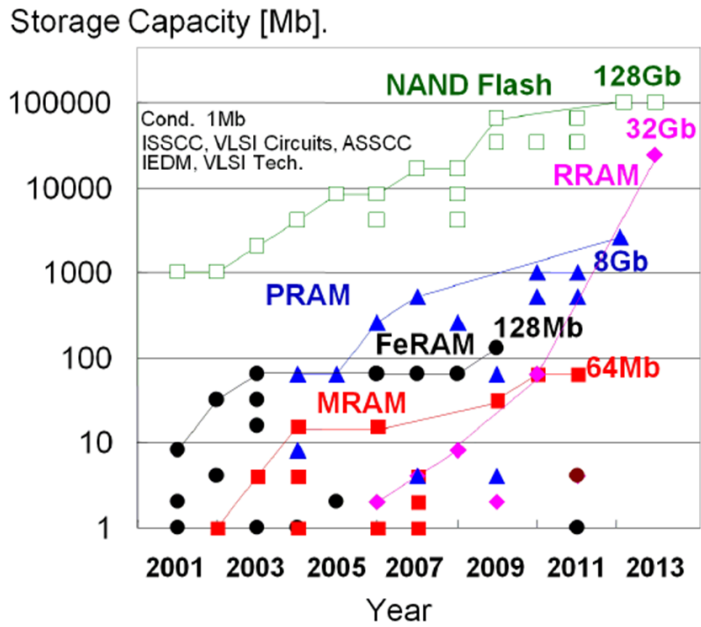


Figure 1. 4. The storage capacity of NAND flash and several next-generation new memory. [16]

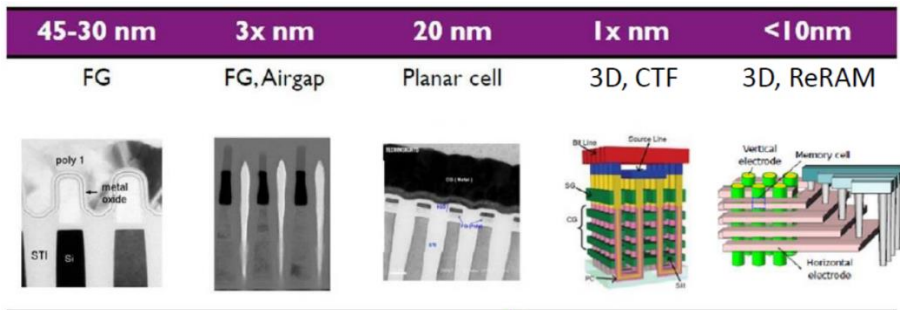


Figure 1. 5. Direction of development of the ultra high density memory. [17]

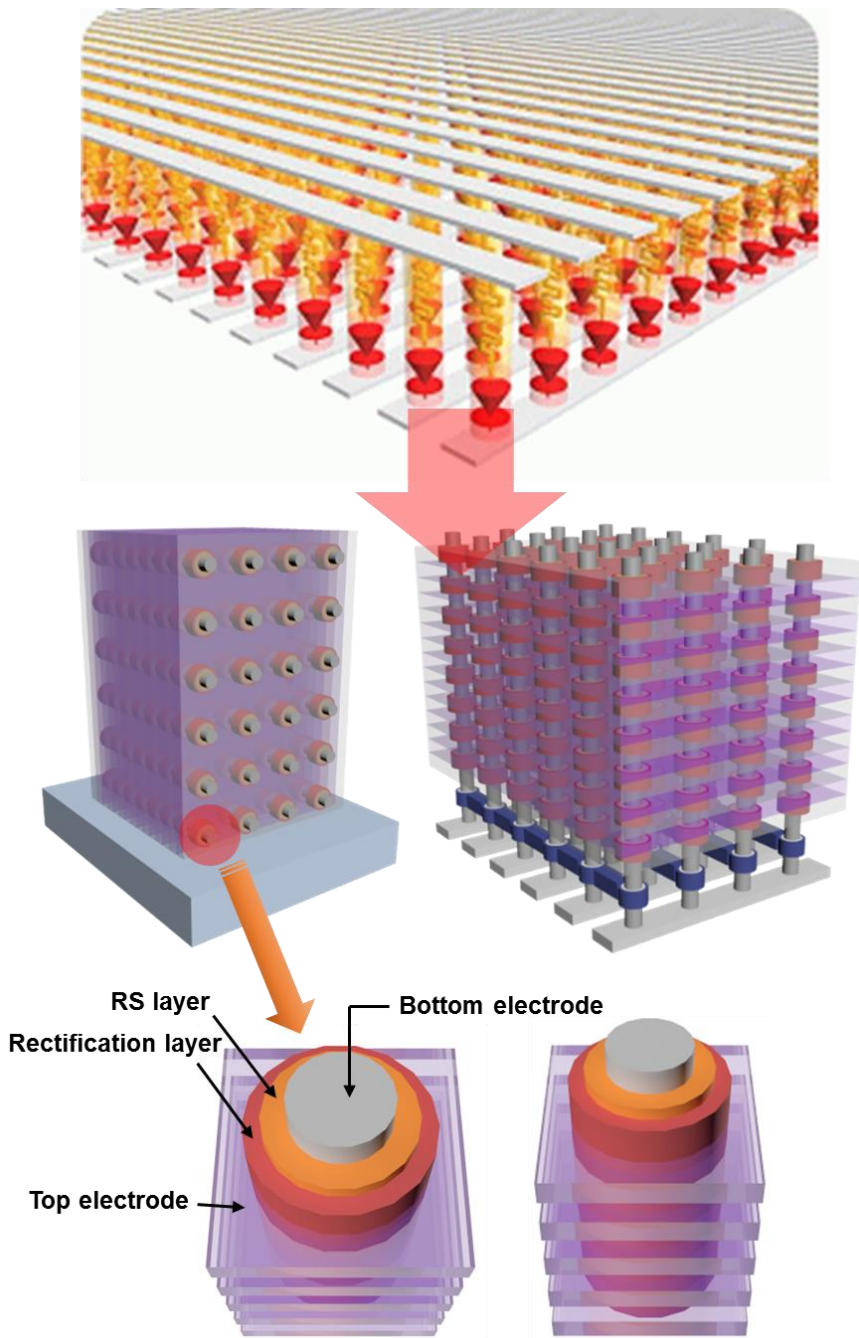


Figure 1. 6. Direction of development of the ReRAM structure concept

1.3. Research scope and objective

In this work, a feasible method which applied to planar or vertical type CBA ReRAM is presented. The non-uniform RS performance which is critical problem of ionic type RS memory is highly improved by Ru nano-dots embedded in TiO₂ film. The new concept of self-rectifying RS memory with excellent uniformity, electroforming-less property and multi-level switching functionality in order to apply to the planar or vertical type 3D ReRAM is presented in chapter 3 and 4.

In chapter 2, the RS memory cells consisting of TiO₂ film and Pt electrodes with the configurations of a planar capacitor and crossbar arrays are fabricated. In order to control the locations where the conducting filaments are formed and achieve excellent uniformity of RS parameters, Ru nano-dots with varying sizes and densities are embedded in the TiO₂ film. Ru nano-dots plays a role as an electricfield concentrator or suppressor depending on the positions along the film thickness direction.

In chapter 3 and 4, the self-rectifying RS memory cells consisting of HfO₂ and Ta₂O₅ bi-layered structure with Pt (top) and TiN, Ti (bottom) electrodes as the configurations of dot pattern and crossbar arrays which can provide excellent uniformity in the switching parameters and obtain electroforming-free, self-rectifying, self-limited current and multi-level switching functionality are fabricated. The key point of the idea is related to the role of each layer of HfO₂ and Ta₂O₅. The fluent RS behavior is highly related to the

HfO₂ layer which is connected to the bottom TiN, Ti electrode while the Ta₂O₅ plays the role of rectifying layer which is connected to top Pt electrode. So, in this self-rectifying I-V characteristics of these materials systems, the feasible RS behavior is observed in one bias polarity while the current flow in the opposite bias polarity is highly suppressed. Also, the functional films were grown by atomic layer deposition (ALD) and thus it is very friendly to the future vertical type CBA structure and further applications.

1.4. Bibliography

- [1] R. Waser, Nanotechnology, Vol. 3, **2008**, Wiley-VCH.
- [2] R. Waser, Nanoelectronics and Information Technology Ch. 4, **2003**, Wiley-VCH.
- [3] R. Waser, M. Aono, Nat. Mater. **2007**, 6, 833.
- [4] R. Waser et al., Adv. Mater., **2009**, 21, 2632-2663.
- [5] A. Sawa, Materialstoday, **2008**, 11, 6.
- [6] B. J. Choi et al., J. Appl. Phys., **2005**, 98, 033715.
- [7] W. W. Zhuang, et al., Tech. Dig. IEDM, **2002**, 193.
- [8] I. G. Baek, et al., Tech, Dig, IEDM, **2004**, 587.
- [9] M. N. Kozicki, M. Mitkova, in Nanotechnoly, Vol. 3, **2008**, Wiley-VCH.
- [10] M. Wutting, N. Yamada, Nat. mater., **2007**, 6, 824.
- [11] A. Asamitsu, et al., Nature, **1997**, 388, 50.

- [12] A. Beck, et al., *Appl. Phys. Lett.*, **2000**, 77, 139.
- [13] M. N. Kozicky, et al., *J. Electrochem. Soc.*, **1999**, 146, 298.
- [14] K. M. Kim, et al., *Nanotechnology*, **2010**, 21, 305203.
- [15] M. Liu, *TIT*, **2012**.
- [16] T. -Yi Liu et al., *IEEE Solid-State Circuits Conference Digest of Technical Papers*, **2013**, 210.
- [17] S. G. Park, *5th Workshop on Innovative Memory Technology*, **2013**.
- [18] H. Tanaka, et al., in *Proc. IEEE Symp, on VLSI Technology*, **2007**, 14.
- [19] G. H. Kim, J. H. Lee, J. H. Hwan, S. J. Song, J. Y. Seok, J. H. Yoon, K. J. Yoon, M. H. Lee, T. J. Park, C. S. Hwang, *Appl. Phys. Lett.*, **2012**, 100, 213508.
- [20] W. Y. Park, G. H. Kim, J. Y. Seok, K. M. Kim, S. J. Song, M. H. Lee, and C. S. Hwang, *Nanotechnology*, **2010**, 21, 195201.
- [21] J. Huang, Y. Tseng, C. Hsu, and T. Hou, *IEEE Electron Device Letters*, **2011**, 32, 1427-1429.
- [22] W. Lee, J. Park, S. Kim, J. Woo, J. Shin, G. Choi, S. Park, D. Lee, E. Cha, B. h. Lee, and H. Hwang, *ACS NANO*, **2012**, 6, 8166-8172.
- [23] M. Son, J. Lee, J. Park, J. Shin, G. Choi, S. Jung, W. Lee, S. Kim, S. Park, and H. Hwang, *IEEE Electron Device Letters*, **2011**, 32, 1579-1581.

2. Improving Uniformity in the Resistive Switching Parameters of TiO₂ Thin Films by Inserting Ru Nano-Dots

2.1. Introduction

The understanding of resistance switching (RS) mechanisms in many oxide materials and its application to resistance switching random access memory (ReRAM) have been greatly improved over the last decade.[1-5] This has mainly been attributed to the improvement in the device fabrication methods and application of various state-of-the-art analysis techniques, such as in-situ transmission electron microscopy[6-10], X-ray imaging[11], and atomic force microscopy[12-13]. While there are detailed variations in the nature, shape, electrical properties, and distribution across the RS layer, the RS behaviors of many RS materials are closely related to the presence of nano-scale conducting filament (CF), where the repeated formation and rupture of CFs are controlled by the thermally-assisted electromigration of defects, mainly oxygen vacancies in oxides.[1-5]

There are still several key concerns remaining with these materials in addition to device integration and architecture issues, including inappropriate repeatability of the RS parameters and insufficient endurance (number of writing cycles), which are material-property-related problems. The possible

influence of various crystallographic phases of the oxide materials on the RS performance has not been clarified either. The non-uniform RS performance with the increasing number of RS cycles or memory cells is generally related to the non-uniform and uncontrolled formation and rupture of CFs over a large area of the memory cell, which are caused by their random nucleation and uncontrolled growth. This suggests that confining the location where the CFs form to a certain region of the memory cell would improve the repeatability problem. In fact, the locations where the CFs are formed appeared to change with increasing number of cycles,[14] which is closely related to the uncontrolled rupture and rejuvenation of CFs.

TiO₂ is one of the prototype RS materials among the binary oxides due to the easy migration of oxygen ions by its relatively low bonding energy compared with other oxides, such as HfO₂ and ZrO₂, and the presence of electrically conducting Magnéli phases (Ti_nO_{2n-1}, n = 2, 3, 4...).[6] However, these characteristics also cause reliability and power consumption issues related to the evident phase transition between the insulating mother phases (anatase, rutile or even amorphous) and the Magnéli phases. Magnéli phases are derived structures from rutile TiO₂, where the accumulated oxygen vacancies on the (121) rutile crystallographic plane comprise the Magnéli phases. Therefore, it could be conjectured that the different TiO₂ phases may influence the RS performance of the film.

In this work, the RS memory cells consisting of TiO₂ film and Pt electrodes (metal-insulator-metal (MIM) configuration) with the

configurations of a planar capacitor and crossbar arrays[15] are fabricated. In order to control the locations where the CFs are formed and achieve different phases of the TiO₂ film (anatase or rutile), Ru nano-dots (Ru-ND) with varying sizes and densities are embedded in the film at two different positions along the film thickness direction. All the functional films and NDs were grown by atomic layer deposition (ALD). It was found that embedded Ru-NDs greatly improved the RS uniformity. The electrode area also played a certain role, but it was relatively minor. There were several works regarding the role of metal NDs on the RS properties of several oxide thin films. Guan et al. embedded Au NDs in ZrO₂ film and found that the device yield was largely improved.[16] Chang et al. reported the improvement in the switching uniformities of TiO₂ film by embedding Pt NDs.[17] However, these works still lack of rigorous analysis on the reason for such improvements. The authors also have reported the improved uniformity of RS parameters in TiO₂ films by adopting the similar Ru-NDs, and concluded that the improvement can be ascribed to the localized rutile phase formation and increased background leakage.[18] However, it was clarified, in this work, that the phases of TiO₂ barely had any control over the RS performance, meaning that the geometry effect, i.e. confining the CF formation to a certain limited area, overwhelms the RS performance by changing the density and location of the Ru-NDs along the TiO₂ film thickness direction. A similar conclusion has been drawn from a quite different set of samples, where the localized defective spots formed by the diffusion of adhesion Ti onto the bottom Pt

electrode surface have improved the switching uniformity.[19]

2.2. Experiment

TiO₂ film and Ru-NDs were deposited at 250 and 230°C by plasma-enhanced ALD using Ti(O-iC₃H₇)₄ and plasma O₂, and thermal ALD using 2,4-(dimethylpentadienyl)(ethylcyclopentadienyl)Ru and O₂, respectively. The details for the ALD of TiO₂ [20], and Ru [18] were reported elsewhere. The Ru layer density was estimated using an X-ray fluorescence analyzer (XRF, ARL Quant'X EDXRF). Conductive atomic force microscopy (CAFM, JSPM-5200) was used for contact mode atomic force microscopy. The crystallographic phases of the TiO₂ films were examined using an X-ray diffractometer (XRD, PANalytical) in θ - 2θ mode. For the capacitor type sample fabrication, circular Pt top electrodes were fabricated by electron beam evaporation through a metal shadow mask, while the standard photolithography and lift off process for top and bottom Pt electrodes were used for the crossbar type sample fabrication. Details for the crossbar pattern fabrication were reported elsewhere.[15] The unipolar RS was examined by a voltage sweep with a compliance current of 20mA during the electroforming step and set process at room temperature using a semiconductor parameter analyzer (SPA, HP 4145B). The electric field concentration simulation data at each sample was obtained by ATLAS.

2.3. Structural Properties of Pt/TiO₂/Pt Resistive Switching Cell with Ru Nano-Dots

Three types of the RS memory samples were fabricated. Pt/TiO₂/Pt structures with no Ru-NDs, designated n-Ru, were used as the reference, and the same structures but with Ru-NDs near the bottom Pt interface designated b-Ru (bottom Ru), and another sample with Ru-NDs near the top Pt interface, designated t-Ru (top Ru) were fabricated. The geometrical configuration for the three types of samples is either capacitor type, in which a continuous 50-nm-thick bottom Pt electrode and a 50-nm-thick TiO₂ film are grown on SiO₂/Si substrate with 300 μ m-diameter circular top Pt electrodes; or crossbar type, in which continuous TiO₂ films intervene between two crossing 50-nm-thick Pt metal lines with widths (W) of 2, 4, 6, 8, and 10 μ m.[15] In order to alleviate the cross-talk effect in the crossbar array, a 1 x 32 configuration was adopted. For the b-Ru and t-Ru sample fabrication, the Ru-NDs are deposited on 5-nm-thick TiO₂/Pt and 45-nm-thick TiO₂/Pt structures, respectively, via another ALD technique with different numbers of ALD cycles (n_{Ru} , 150, 200 and 250) to achieve different densities of Ru-NDs. 45-nm- and 5-nm-thick TiO₂ films, respectively, were subsequently grown before the Pt top electrode fabrication. Specific range of Ru ALD cycles for obtaining Ru NDs with different size and density was examined. Figure 2.1 (a) shows a correlation between the layer density of deposited Ru measured by X-ray fluorescence spectroscopy and number of Ru ALD cycles on the surface of 45nm-thick

TiO₂ film. In addition, the surface morphology over 1 μm x 1 μm area obtained using atomic force microscopy are shown in figures 2.1 (b) ~ (d), where the surface protrusions with height > 5.5 nm are highlighted. From these analysis, the cycle condition for generating Ru-NDs on TiO₂ surface is attained. The height of 5 nm corresponds to the height of Ru nano-dots as confirmed from HRTEM image at figures 3.3 (c). As can be seen in figures 2.1 (b) ~ (d), density of Ru NDs increases as the Ru ALD cycle increases. Once the value of ALD cycle exceed over ~300, the deposited layer resembles more thin film shape since the small Ru particles agglomerate. Therefore, the appropriate cycle number range was from 150 to 250 to generate Ru-NDs without forming the continuous film. Even on 5nm-thick TiO₂ surface, although it is not shown here, the tendency of Ru-ND size and their dispersion with respect to the Ru ALD cycle number are almost identical to that of the results on the 45nm-thick TiO₂.

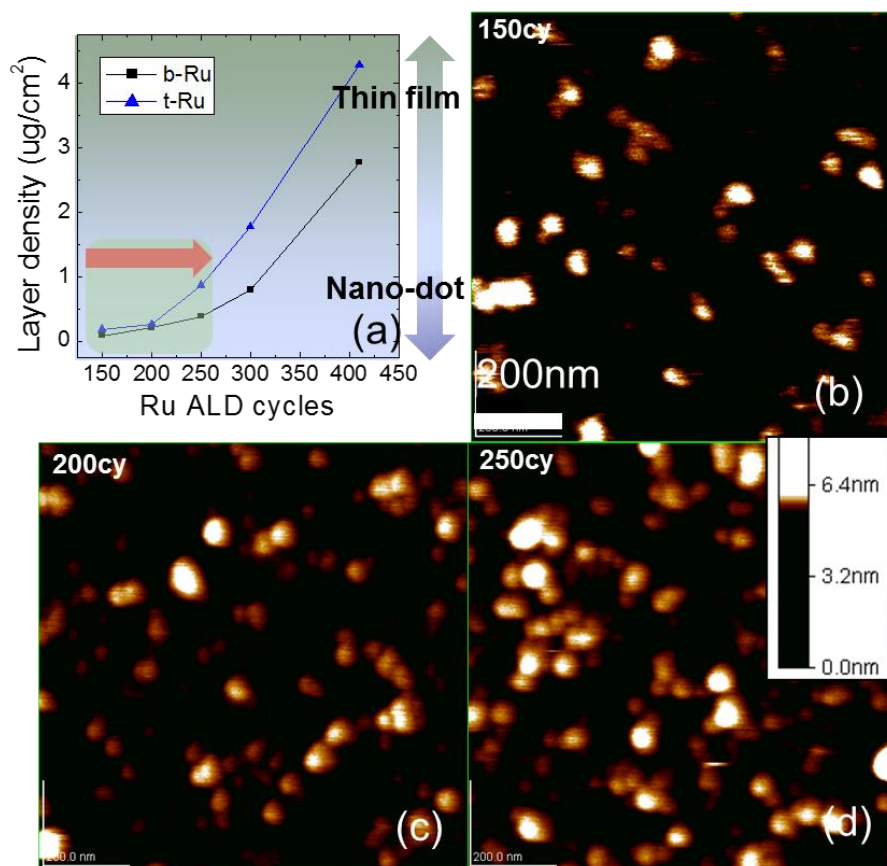


Figure 2. 1. (a) Layer density depending on the Ru ALD cycles and the surface morphology over 1 $\mu\text{m} \times 1 \mu\text{m}$ area of (b) 150, (c) 200 (c), and (d) 250 Ru ALD cycles

Figure 2.2 shows the X-ray diffraction patterns of n-Ru and b-Ru (150cy, 200cy and 250cy) samples. In n-Ru case, there are no diffraction peaks that correspond either anatase or rutile phase TiO_2 . As the Ru ALD cycle number increases, the result starts to show the diffractions peaks corresponding to the anatase ($2\theta \sim 25^\circ$) and rutile ($2\theta \sim 27^\circ$) phases. This suggests that the TiO_2 film on Ru NDs are crystallized into the rutile structure, while other parts of the TiO_2 on Pt substrate crystallized into the anatase structure.

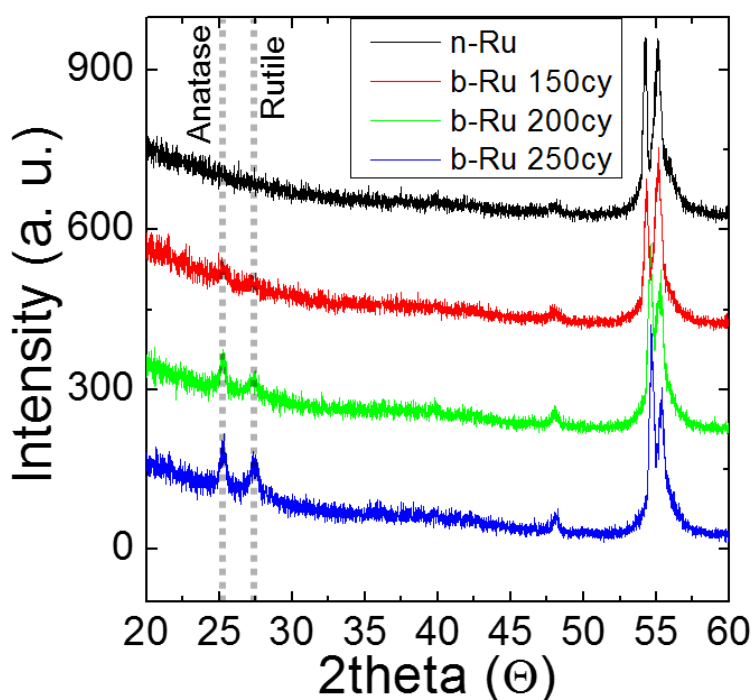


Figure 2. 2. X-ray diffraction patterns of n-Ru and b-Ru (150cy, 200cy, and 250cy) samples

Figure 2.3 (a) shows the microstructure of pristine n-Ru sample obtained using cross-section HRTEM. Mixture of amorphous and anatase phase TiO_2 is formed on Pt substrate as readily expected from the results in previous studies.[22] As an electrical forming process is performed, conducting filaments of the Magnéli phase are formed as can be shown in figure 2.3 (b). These Magnéli phase are randomly dispersed because there are no preferable regions for the formation of conducting filaments. Figure 2.3 (c) shows the formation of an elliptical shaped Ru nanodot in anatase TiO_2 matrix which was taken from the b-Ru sample with n_{Ru} of 150. The height and diameter of the Ru-ND are $\sim 5\text{nm}$ and $\sim 7\text{ nm}$. As discussed in the later part, the formation of conducting filament is highly affected by the presence of Ru-NDs which play as an electric field concentrator. Therefore, a conducting filament formed on the Ru nanodot is found in figure 2.3 (d) which is consistent with the electric field simulation and CAFM measurement result.

Figures 2.3 (e) and (f) show a higher and lower magnification TEM images of the t-Ru ($n_{\text{Ru}} = 250$) sample. They show that the t-Ru NDs (indicated by black arrows) are well covered by the 5-nm-thick TiO_2 film. Especially, the right hand portion of figure 2.3 (e) clearly shows a single grain image throughout the 45-nm-thick bottom TiO_2 and 5-nm-thick top TiO_2 layers suggesting that even the local epitaxial growth was obtained although there was a growth break. Some part of the top TiO_2 seems (indicated by white arrows) to be quite thinner compared with other parts and may raise a concern that these parts are not well covered with the TiO_2 , but this is due to the TEM

artifact where the overlapped images along the TEM foil thickness due to the presence of surface (interface) roughness.

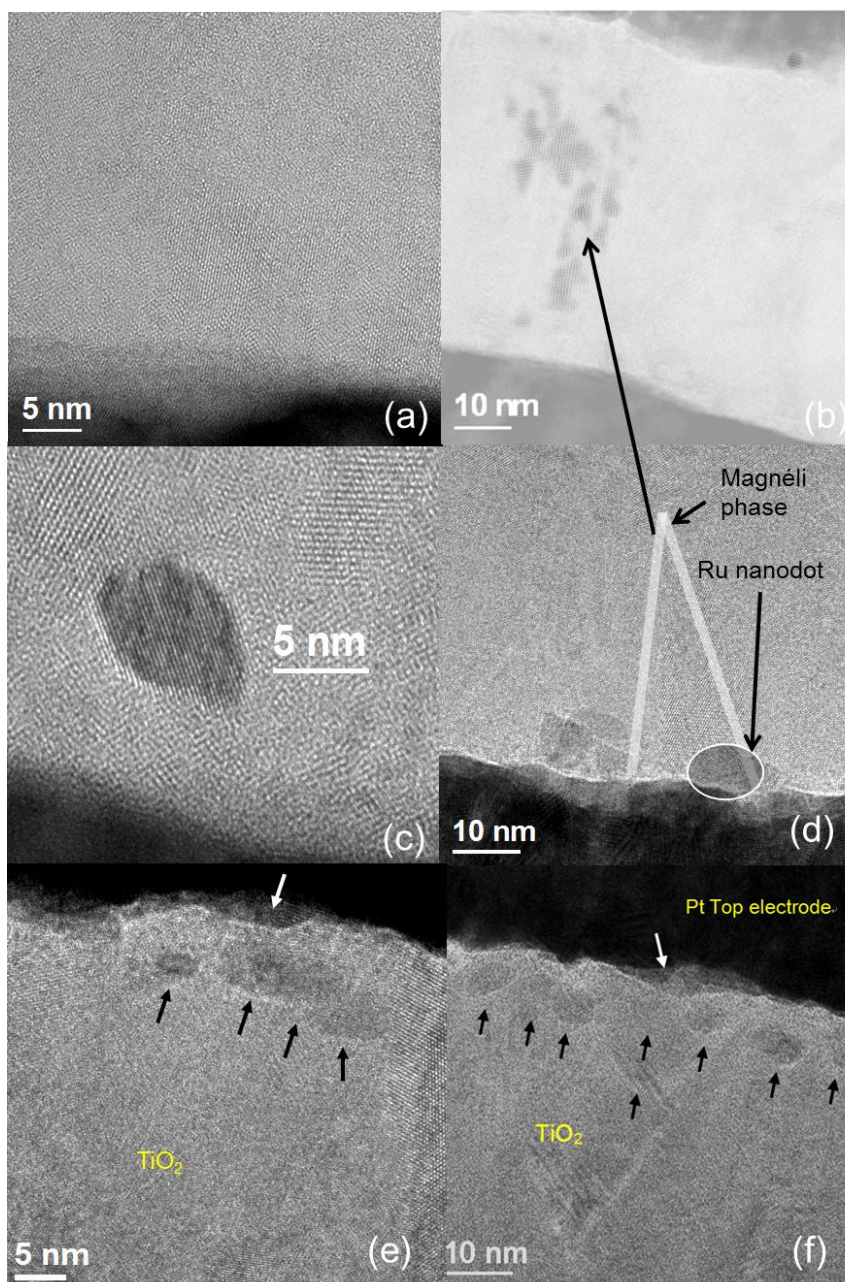
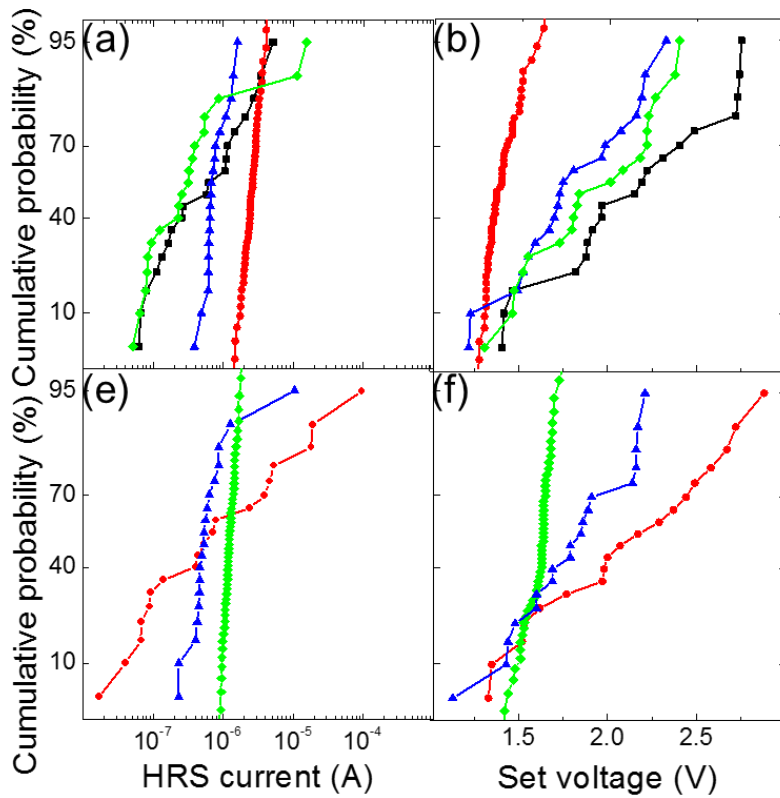


Figure 2. 3. HRTEM images of n-Ru (a) before and (b) after electro-forming process. HRTEM images of (c) formation of an elliptical shaped Ru nanodots and (d) conducting filament formed on the Ru nanodot in b-Ru. (e) Lower and (f) higher magnification TEM images of the t-Ru sample.

2.4. Electrical Performances of the Memory Cell and Switching Mechanism

Figures 2.4 (a) – (d) shows the distributions of high resistance state (HRS) current (measured at 0.2 V), the set voltage (V_{set}), the reset power, and the reset voltage (V_{reset}), respectively, for the n-Ru ($n_{\text{Ru}} = 0$) and b-Ru samples with n_{Ru} of 150, 200, and 250. Here, the samples were of capacitor geometry, and one memory cell from each sample was taken, and measured by 50 times. Figures 2.4 (e) – (h) show the same for the t-Ru samples with n_{Ru} of 150, 200, and 250. The inset figures in Figures 2.4 (c) and (g) show the schematic structure of the b-Ru and t-Ru samples, respectively. The I-V curves for these samples are shown in Figure 2.5. Here, the RS was tested in voltage controlled I-V sweep mode with an appropriate compliance current of 20mA and the bias polarity is depicted in figure 2.5 (e). Although not shown here, the electroforming of both samples was achieved at $\sim 4 - 5$ V. The black lines in the figures show the I-V curves of pristine samples showing their leakage characteristics. It is shown that n-Ru, b-Ru and t-Ru samples have quite similar leakage current values at their pristine states. It can be immediately understood that the inclusion of Ru-NDs largely influences the uniformity of the various RS parameters; the n-Ru sample shows very large variations, but the b-Ru sample with n_{Ru} of 150, called b-Ru150, and t-Ru sample with n_{Ru} of 250, called t-Ru250, showed very narrow distributions of the parameters. While the b-Ru150 showed a slightly larger variation in V_{set} , t-Ru250 showed

an extremely small spread of all the tested parameters. Another notable finding is that the trend of improvement in the uniformity is opposite in b-Ru and t-Ru samples; for the case of b-Ru, the smaller n_{Ru} results in the better uniformity, while the opposite was the case for the t-Ru.



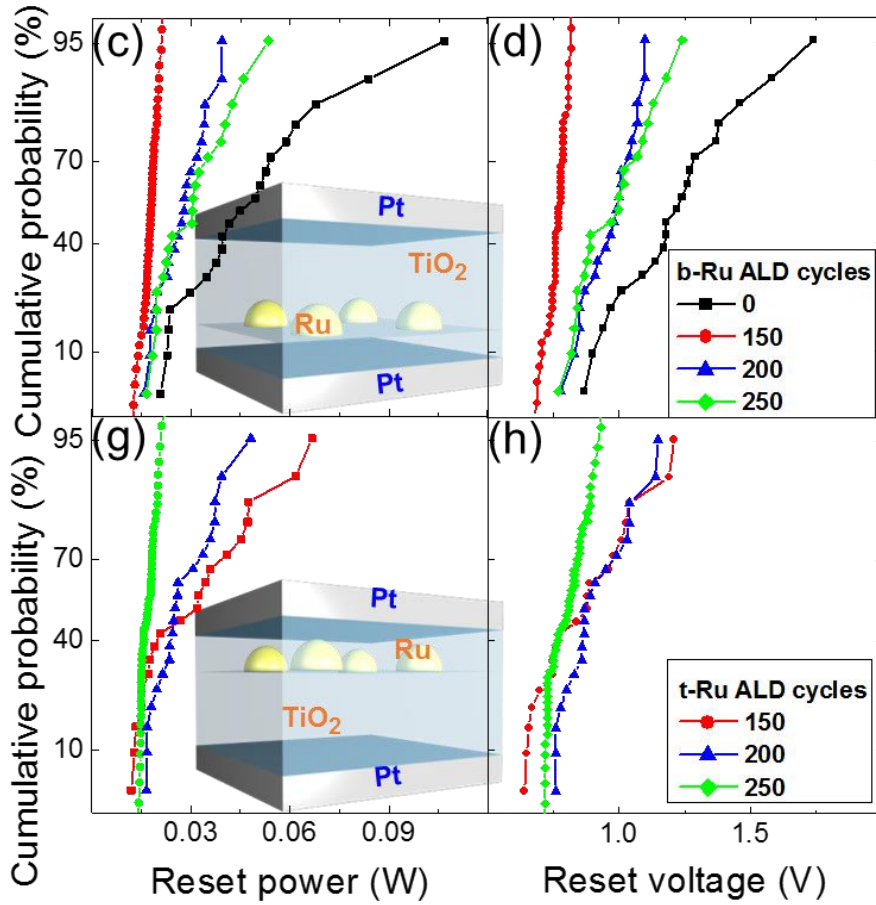


Figure 2. 4. The cumulative probability graphs of high resistance state (HRS) current, the set voltage, the reset power, respectively, for the n-Ru, b-Ru (a) ~ (d), and t-Ru (e) ~ (h) samples with nRu of 150, 200, and 250 when the cell size is $\sim 60,000\mu\text{m}^2$. The sample structure of b-Ru (inset figure of (c)) and t-Ru (inset figure of (g))

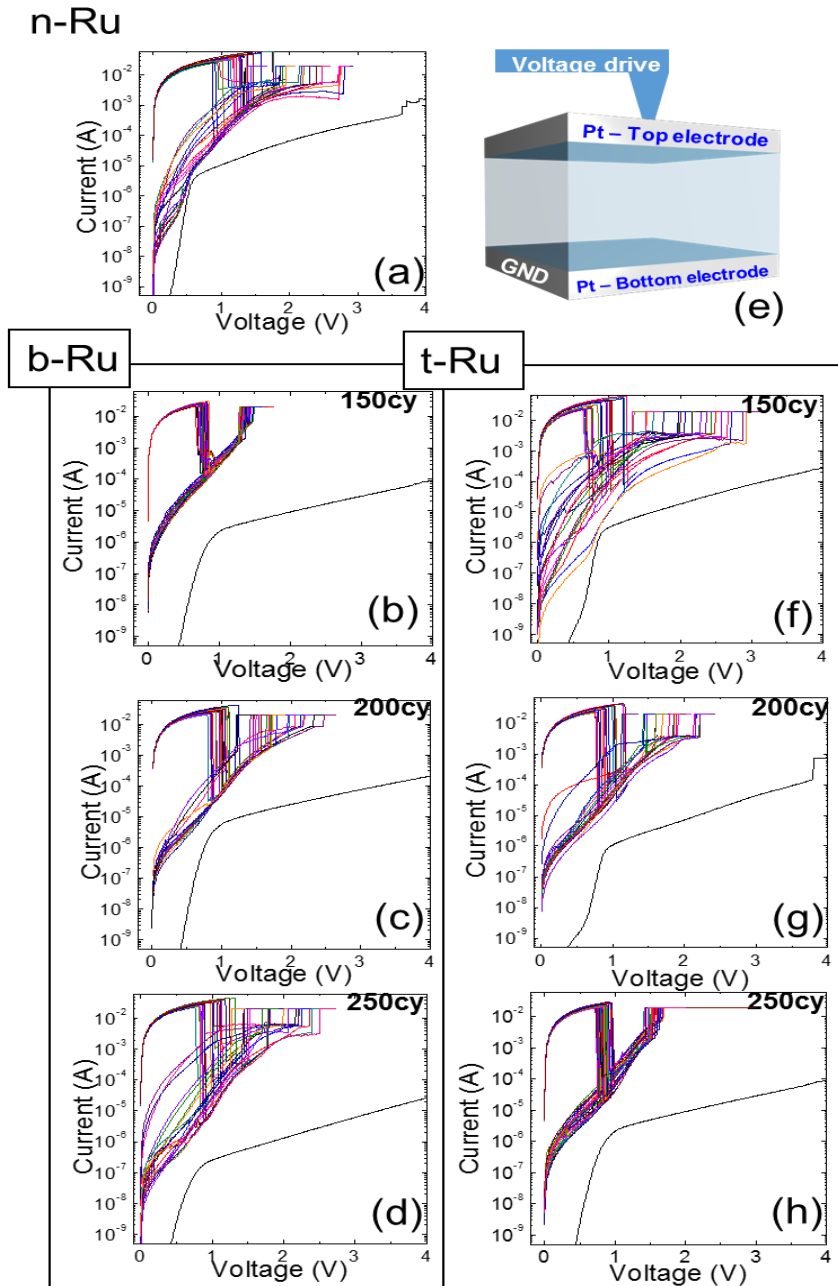
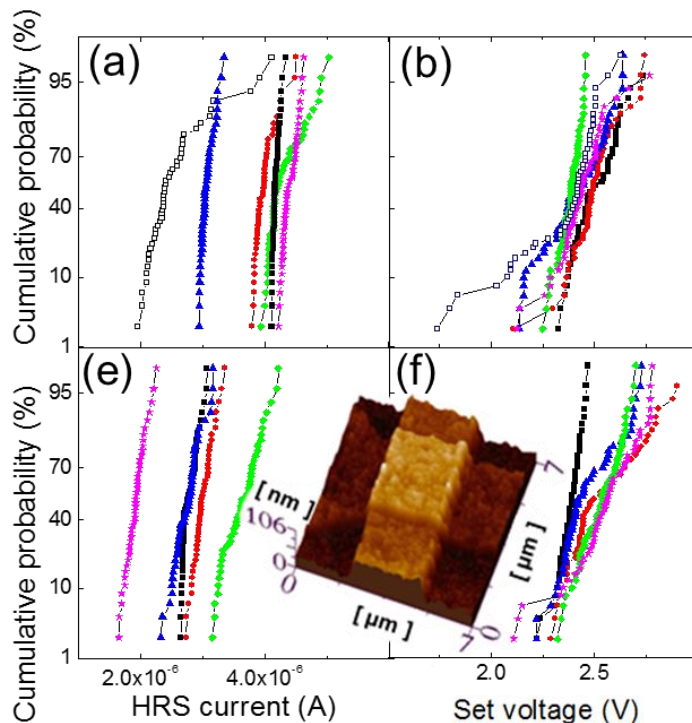


Figure 2. 5. Current-voltage (I-V) curves of unipolar resistive switching of the (a) n-Ru, b-Ru (b) ~ (d), and t-Ru (f) ~ (h) samples with nRu of 150, 200, and 250 when the cell size is $\sim 60,000\mu\text{m}^2$. (e) Schametic image of the measurement system of this device

It is evident in figure 2.4 that the inclusion of discrete Ru-NDs caused a drastic variation in the uniformities of RS performances, so it is important to confirm that the same trend holds even though the electrode area was scaled down. Despite the cell size is reduced to almost 1/10,000, the same trend was observed from the crossbar type samples after 50 measurements from each sample, as shown in figure 2.6. Here, the minimum electrode area in the crossbar configuration is limited to $4 \mu\text{m}^2$, so the results shown in figure 2.6 may not represent the genuine nano-scale devices. However, as can be understood from figures 2.8 and 2.11, the average size and distances between the Ru-NDs are on the order of a few tens of nanometers, making the adoption of even smaller electrode area less statistically meaningful. For the truly nano-scale devices, the Ru-ND size and distribution must be on the scale of only a few nm, which is beyond the scope of this work.

The scaling of the electrode area of the n-Ru sample down to $16 \mu\text{m}^2$ from the large capacitor type sample ($60,000 \mu\text{m}^2$) already reduced the spread quite largely as can be seen in figures 2.6 (a) – (d) (open square symbol). However, the inclusion of Ru-NDs essentially removed the largely tailed distributions as shown in figures 2.6 (a) – (d) where the b-Ru ($n_{\text{Ru}} = 150$) structure was adopted, and Figs. 3.6 (e) – (h) where the t-Ru ($n_{\text{Ru}} = 250$) structure was adopted. The inset figure of figure 2.6 shows the AFM image of the $4 \times 4 \mu\text{m}^2$ crossbar sample with t-Ru structure. When the optimized n_{Ru} (150 for b-Ru and 250 for t-Ru) was adopted in each case, the smaller W tended to show slightly better uniformity in the parameters, but the trend was not so evident.

The inset figure in figure 2.6 (c) shows the variations in set and reset state resistances, measured at 0.2 V, as a function of the electrode area of the crossbar structure. It is evident that the resistances are independent of the area of all types of samples, suggesting highly localized CF formation and rupture irrespective of the presence of the Ru-NDs. Figure 2.7 shows the improved switching uniformity as a function of number of switching cycles for the different samples. The variation of resistance values in HRS and LRS with the switching cycle number of the various samples is described. Although the samples with smaller electrode area ($16 \mu\text{m}^2$) generally show better uniformity than the samples with the large electrode area ($\sim 60,000\mu\text{m}^2$), the b-Ru with n_{Ru} of 150 and t-Ru with n_{Ru} of 250 samples show excellent uniformity in both values.



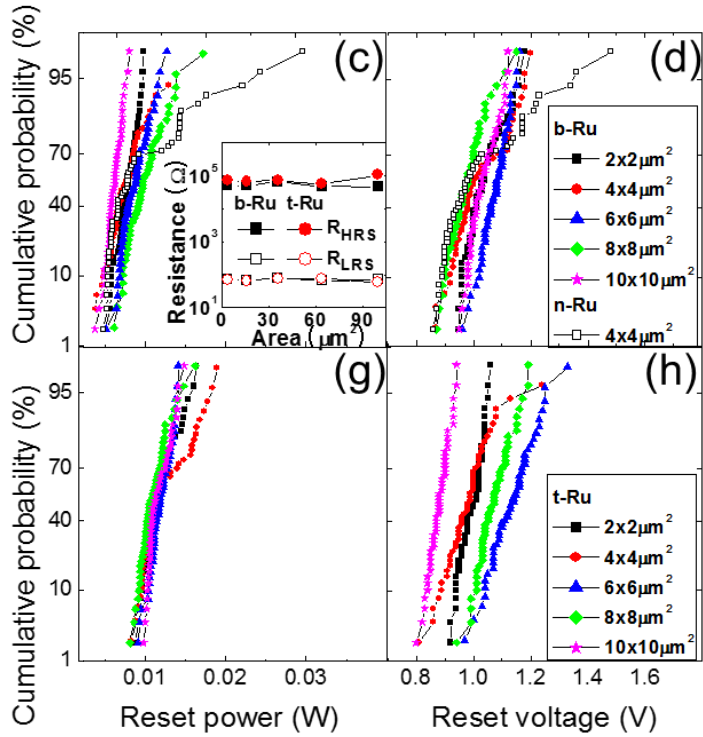


Figure 2. 6. The cumulative probability graphs of high resistance state (HRS) current, the set voltage, the reset power, respectively, for the n-Ru, b-Ru (nRu = 150) (a) ~ (d), and t-Ru (nRu = 250) (e) ~ (h) samples when cell sizes are $2 \times 2 \sim 10 \times 10 \mu\text{m}^2$. Area dependency of resistance in HRS and LRS (inset figure of (c)) and the morphology of crossbar type sample (inset figure of (f))

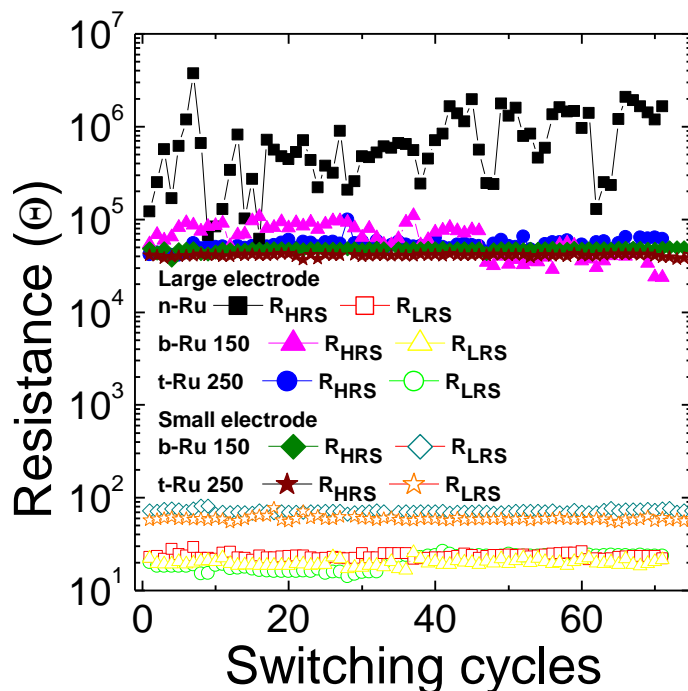


Figure 2. 7. Variation of resistance values in HRS and LRS with the switching cycle number of the n-Ru, b-Ru (nRu = 150), and t-Ru (nRu = 250)

Since such a drastic change in the RS performance with the inclusion of Ru-NDs was considered to be related to the modified distribution of local conducting spots, the b-Ru and t-Ru samples were examined using conductive atomic force microscopy (CAFM) before the Pt top electrode was deposited. Here, the focus was on the relative locations of protruded area, which is supposed to be the locations of Ru-NDs, and locally electrically conducting

area, which is supposed to be developed into the CFs during the subsequent electroforming or set operation. Figure 2.8 (a) shows the digitized topographic images of the t-Ru samples with n_{Ru} of 150 (left), 200 (middle), and 250 (right), and figure 2.8 (b) shows the corresponding local current images. The original topographical and unfiltered CAFM images are shown in figure 2.9. Figure 2.8 (c) shows the overlapped topographic and current images of t-Ru250 in (a) and (b) with a higher magnification, where the local current path and protruded areas are coincident, suggesting that the regions where the Ru-ND resides are more electrically conducting and will subsequently evolve into CF. This was further confirmed by the increasing number of electrically conducting spots (figure 2.8 (b)) with the increasing n_{Ru} . Figure 2.8 (d) shows a schematic diagram of the bias application, and electric field distribution across the cross-section of the film containing one Ru-ND for this CAFM experiment. The tip was grounded and the bottom Pt electrode was biased positively. The bias scheme corresponds to the b-Ru sample case shown in figures 2.4 (a) and 2.6 (a), where the top Pt electrode was biased positively and the bottom Pt electrode was grounded. In these cases (figures 2.4 (a), 2.6 (a), 3.8 and 3.9), the electrons are injected from the Pt electrode where the Ru-NDs reside nearby. The electron injection is a prerequisite to induce the CF formation via the Joule heating effect, therefore, identifying the location where the electrons are injected is crucial to identifying the CF location even before the actual CF formation.[21]

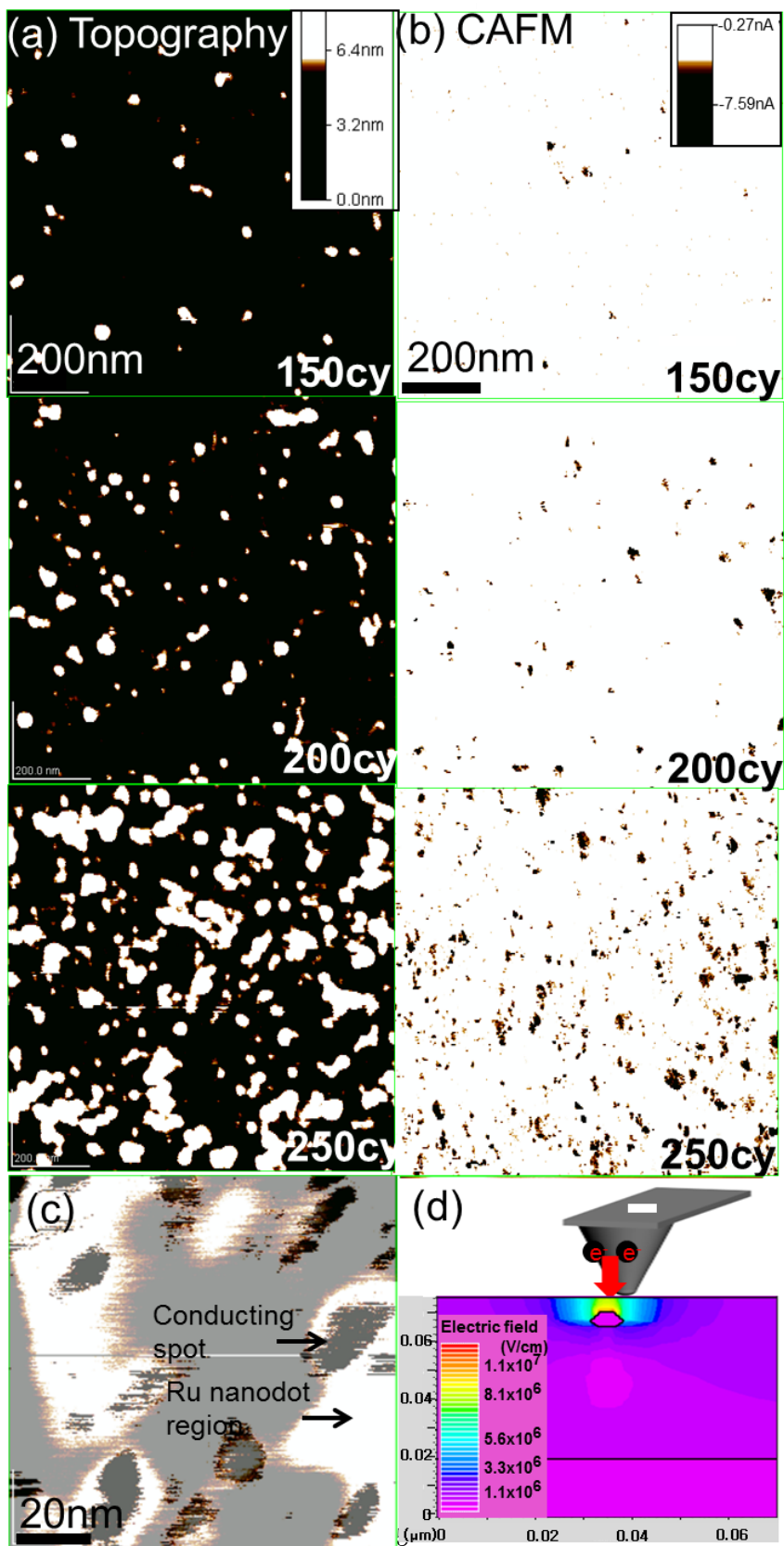


Figure 2. 8. (a) The digitized topographic images of the t-Ru samples with nRu of 150 (left), 200 (middle), and 250 (right), and (b) the corresponding local current images. (c) The high-resolution overlapped topographic and current images of t-Ru250 in (a) and (b). (d) The schematic diagram of the bias application, and electric field distribution across the cross-section of the film containing one Ru-ND for this CAFM experiment

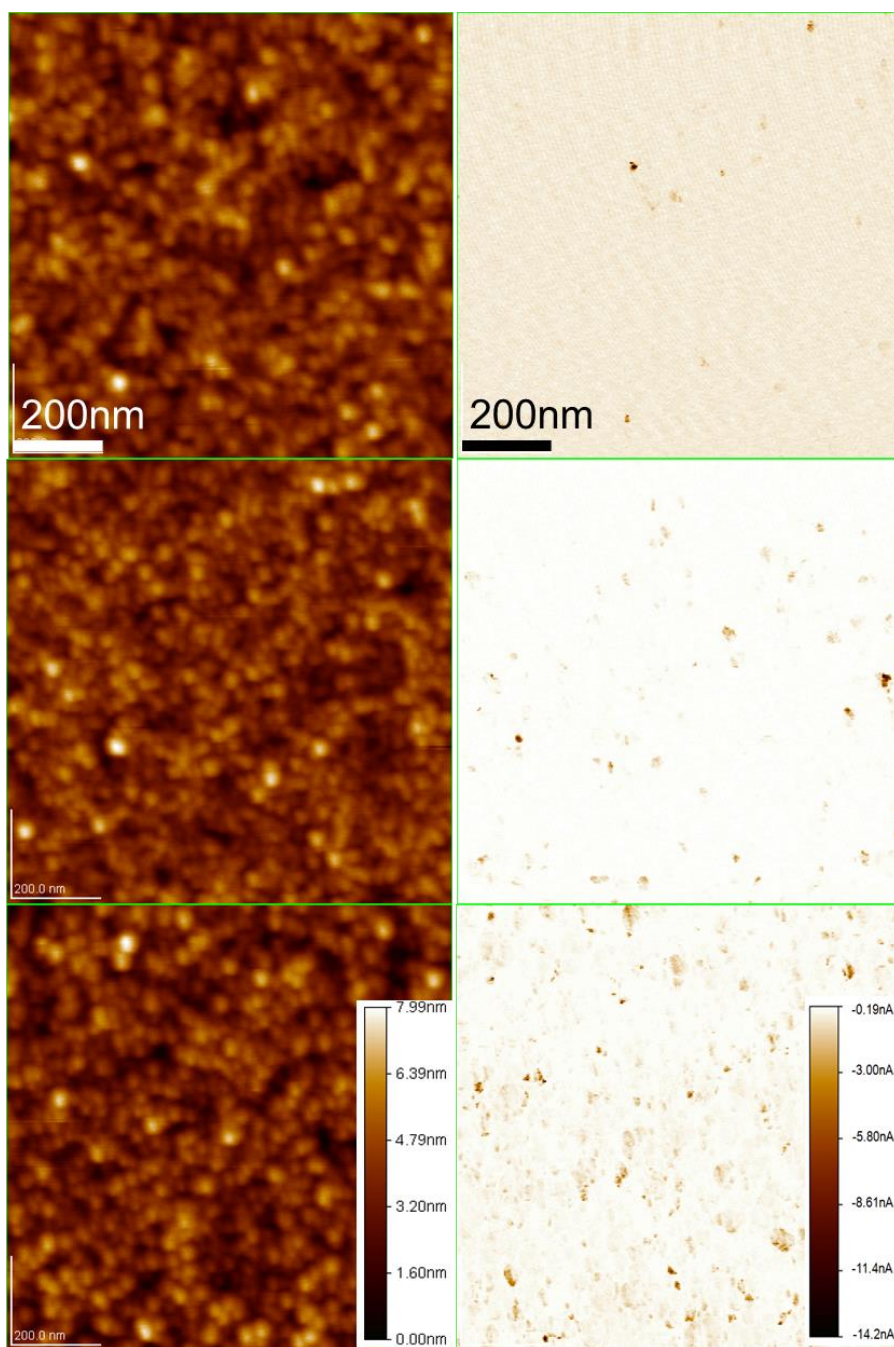


Figure 2. 9. Original topographical and unfiltered CAFM images shown in figure 2.8

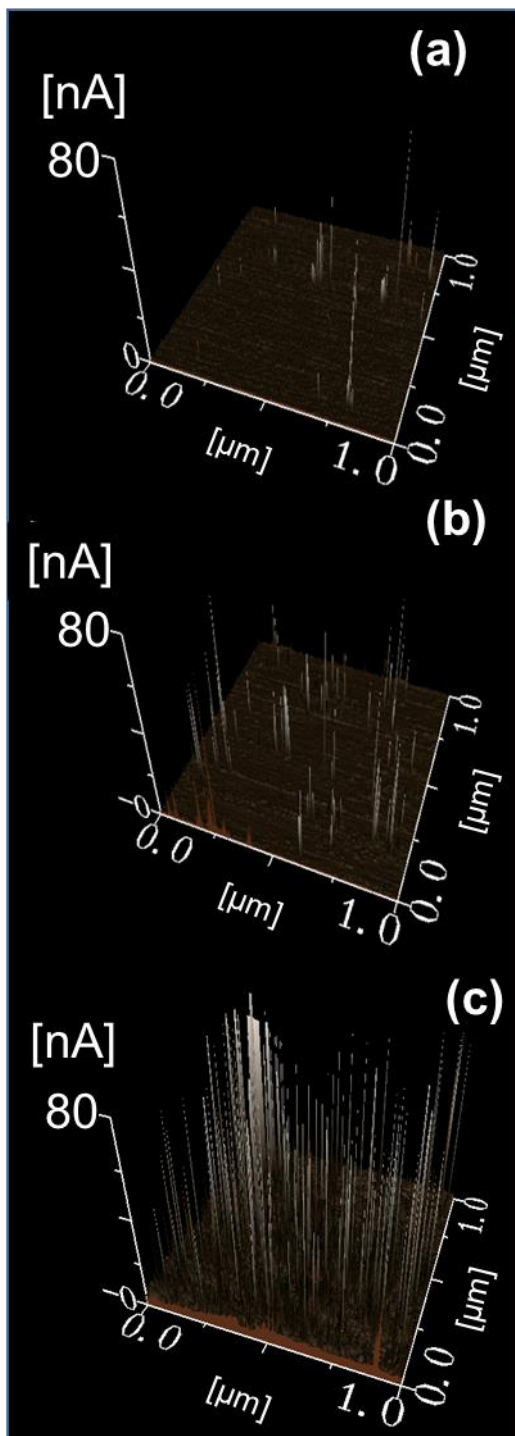


Figure 2. 10. Three-dimensional image of CAFM of the figure 2.8 (b)

Figures 2.11 (a) – (d) show the topographic, current, and overlapped CAFM images, and schematic diagram, respectively, for the b-Ru samples with the same bias application. Also, the original topographical and unfiltered CAFM images are shown in figure 2.12. It can be noted that there is hardly any coincidence between the topographically protruded area and electrically conducting area (figure 2.11 (c)), which was further confirmed by the decreased number of conducting spots with the increasing n_{Ru} (figure 2.11 (b)). An interesting finding is that when the number of conducting spots is limited ($150 n_{Ru}$ of in figure 2.8 and $250 n_{Ru}$ of in figure 2.11), better uniformity of RS parameters was achieved (b-Ru150 and t-Ru250 samples in figures 2.4 and 2.6). This is in fact consistent with the usual conjecture that limiting the number of CFs would improve RS uniformity.

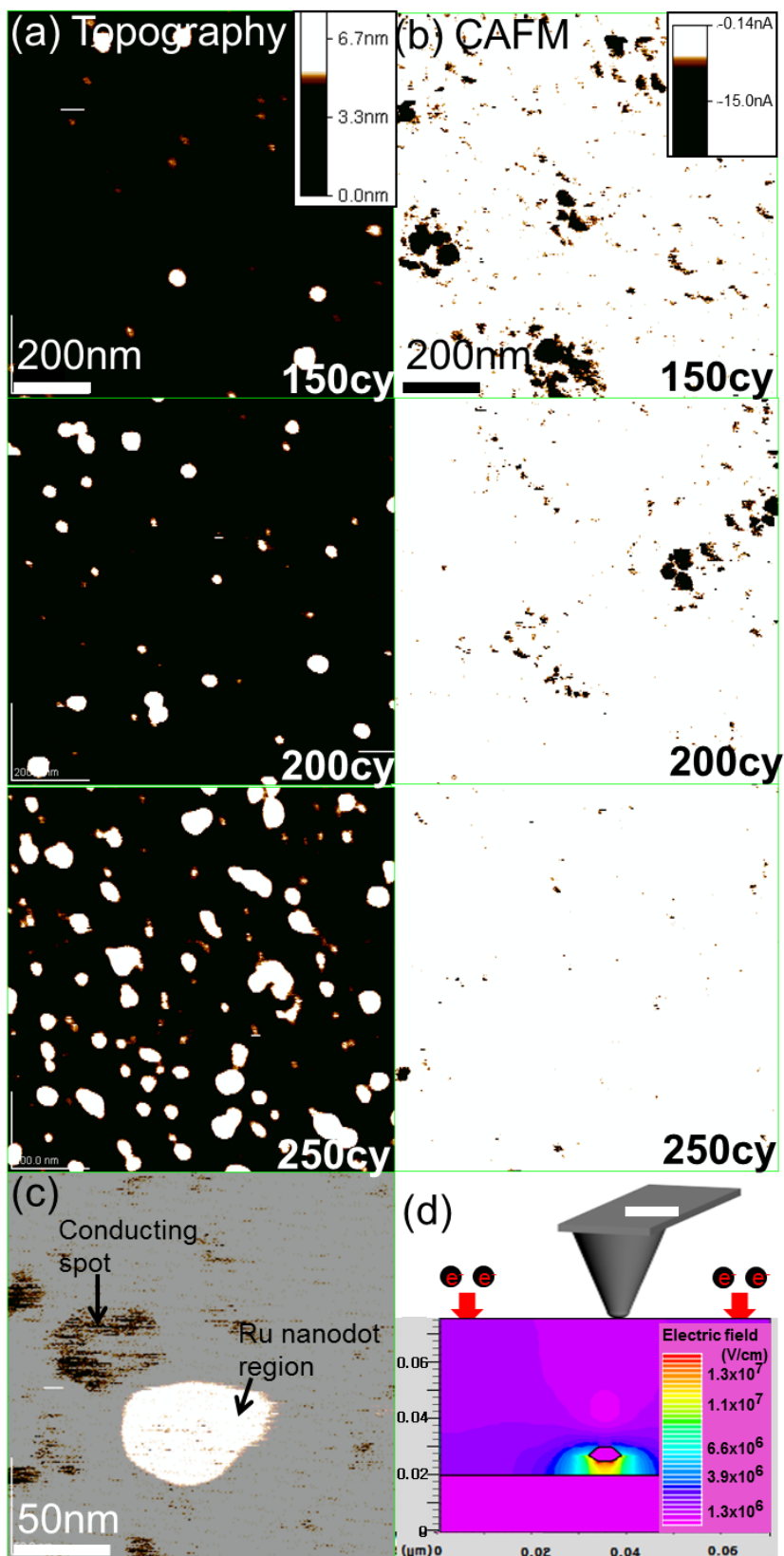


Figure 2. 11. (a) The digitized topographic images of the b-Ru samples with nRu of 150 (left), 200 (middle), and 250 (right), and (b) the corresponding local current images. (c) The high-resolution overlapped topographic and current images of b-Ru250 in (a) and (b). The schematic diagram of the bias application, and electric field distribution across the cross-section of the film containing one Ru-ND for this CAFM experiment

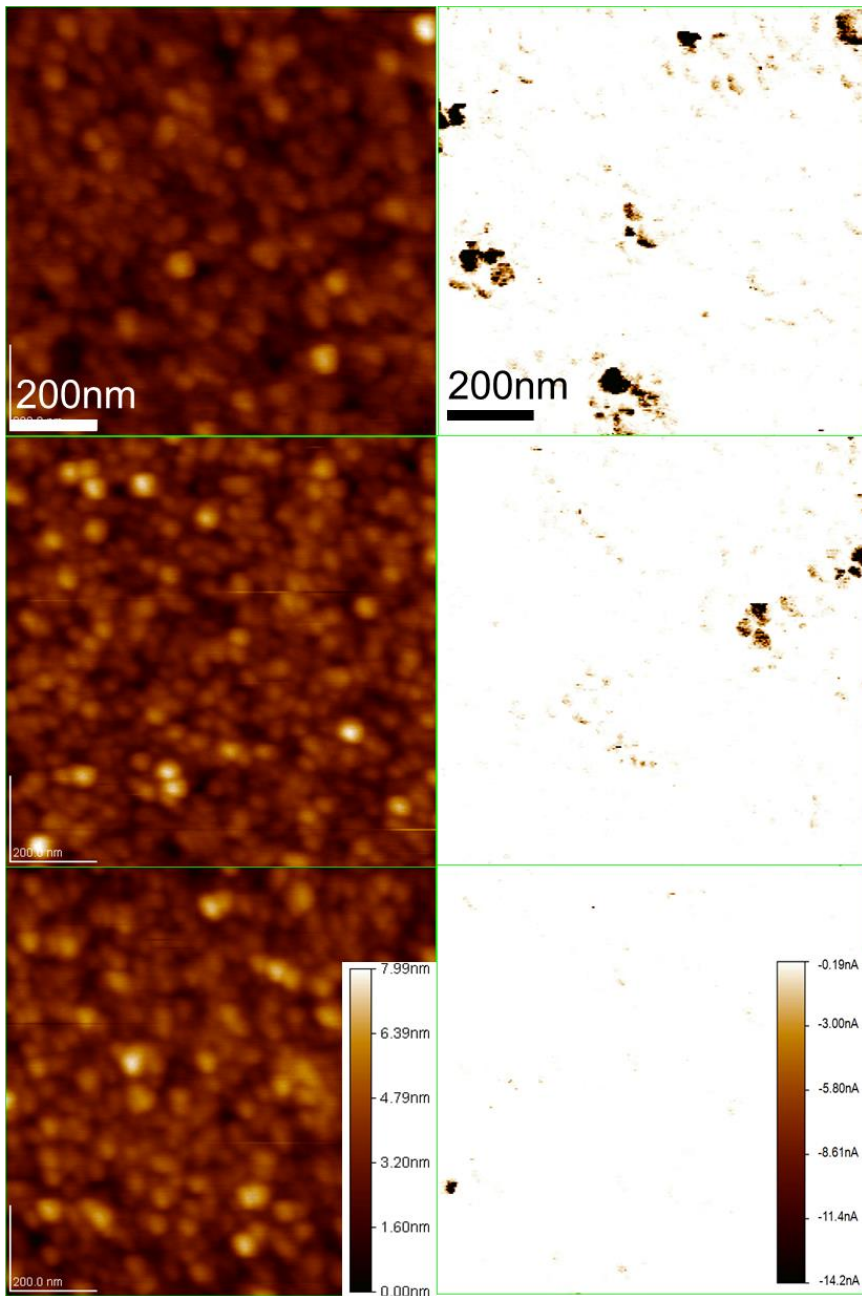


Figure 2. 12. Original topographical and unfiltered CAFM images shown in figure 2.11

The reason for the opposite trend of the coincidence between the topographic feature and local conduction can be understood from the simulation of electric field distributions as shown in figures 2.8 (d) and 2.11 (d). The electric field at the interface between the Pt-coated AFM tip and TiO₂ surface governs the electron injection, so the field distribution at that location must be focused. In figure 2.8 (d), the proximity between the Ru-ND and tip largely enhances the field between them, and the electron injection from the tip to the Ru-ND through the thin (~ 5nm) intervening TiO₂ must be fluent and the Ru-ND must be readily charged with electrons. Once the Ru-ND is charged with electrons, further injection of electrons from the Ru-ND into the bulk of TiO₂ must be highly enhanced compared with the other parts (note that this situation is not depicted in figure 2.8 (d)), which makes the location of Ru-ND coincide with the high carrier injection. In contrast, for figure 2.11 (d), the high field was induced between the Ru-ND and bottom electrode, which decreases the electric field on the TiO₂ surface at the location of Ru-ND, and the carrier injection at that location must be suppressed compared with the other parts. This corresponds to the distribution of local conducting path with respect to the Ru-NDs shown in figures 2.11 (a), (b) and (c).

Similar simulations were performed for the capacitor type samples having different Ru-ND density, as shown in figure 2.13. In this simulation, the Ru-ND densities were set considering the experimental results shown in figures 2.8 and 2.11, and the top electrode was assumed to be biased with +5 V in accordance with the experimental situations in figures 2.4 and 2.6. In order to

achieve the accurate simulation results, the protrusion on the TiO₂ surface by the presence of embedded Ru ND is also considered. The detailed effect of protrusion on the distribution of electric field is shown in figure 2.14. Here, the protrusion on the TiO₂ surface by the presence of embedded Ru ND was considered or not. Due to the tiny size and height compared with the TiO₂ film dimension, there are hardly any influence of the Ru-ND on the field distribution. The electric field distribution was simulated for the b-Ru (figure 2.13 (a)) and t-Ru (figure 2.13 (b)) samples. In this situation, the key factor that eventually controls the CF formation is the carrier injection at the bottom electrode (cathode) interface.[21] so that the field distribution along the bottom interface (marked by the yellow band in the figures) is highlighted in the right hand panels of each figure. The area where the field concentration occurs is highly limited to the region where the Ru-NDs reside for the case of b-Ru samples, so that the smaller n_{Ru} results in a smaller number of locations with concentrated field and an accompanying smaller number of CFs in this case. This is in a qualitative agreement with the experimental results with b-Ru samples shown in figures 2.4 and 2.6. In contrast, the region between the Ru-NDs (or clusters of Ru-NDs) showed a higher electric field for the case of t-Ru samples. Therefore, the number of spots where the field concentrates actually increases with the increasing n_{Ru} , which appears to be inconsistent with the experimental results with t-Ru samples shown in figures 2.4 and 2.6. However, it must be noted that there is a critical difference between the simulation results in figures 2.13 (a) and (b). The nominal applied field is ~ 1

MV/cm, but the peak field in figure 2.13 (a) is ~ 10 MV/cm, suggesting that the Ru-NDs work as the field enhancer in this case. However, the maximum field in figure 2.13 (b) is almost ten times lower than the other case, suggesting that the Ru-NDs in this case work as the field suppressor. Therefore, the higher the n_{Ru} is the lower the field at the cathode interface. Now, it must be noted that the simulations in figure 2.13 assumed a uniform distribution of Ru-NDs with different density, but the actual situation is not like that; as can be seen in figure 2.11, there is certain areas where the Ru-NDs density is substantially lower than the other area. These areas must be the locations where the CFs nucleate when the bias is applied. Therefore, the higher Ru-NDs density is the lower the CF density for this case. It must be noted that the lower Ru-NDs density is the lower the CF density in the other case since the CFs are formed where the Ru-NDs are. Similar improvements in the RS uniformity were also observed for the bi-polar type operation as shown in figure 2.15.

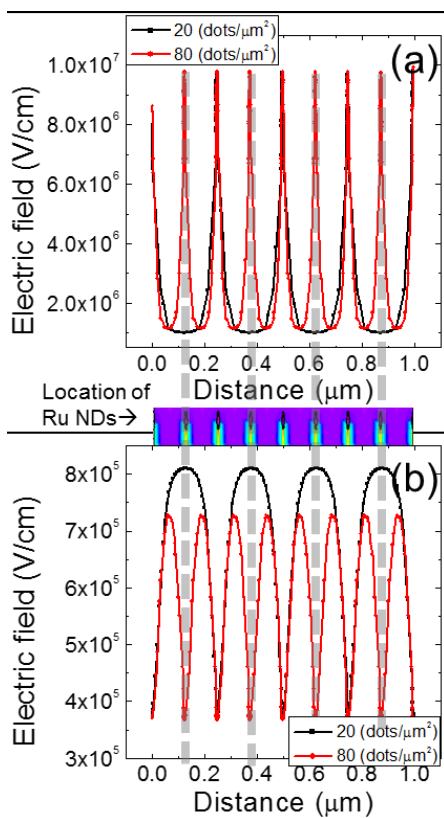
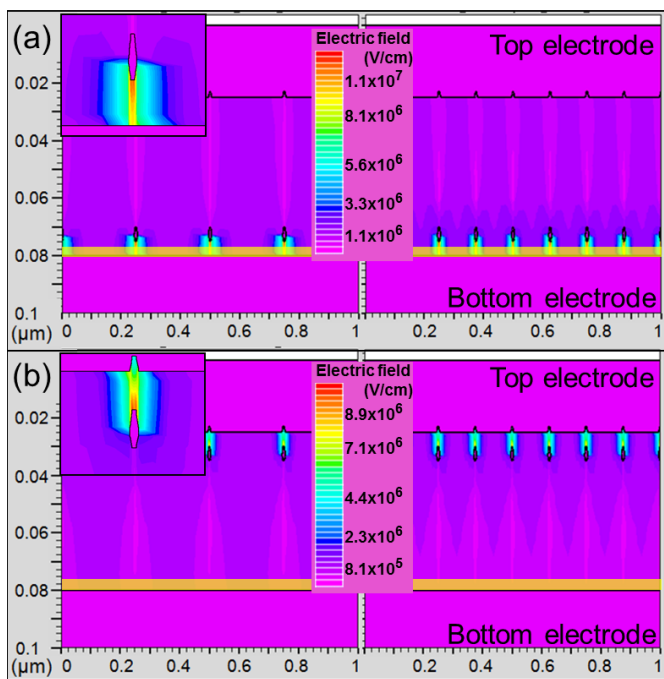
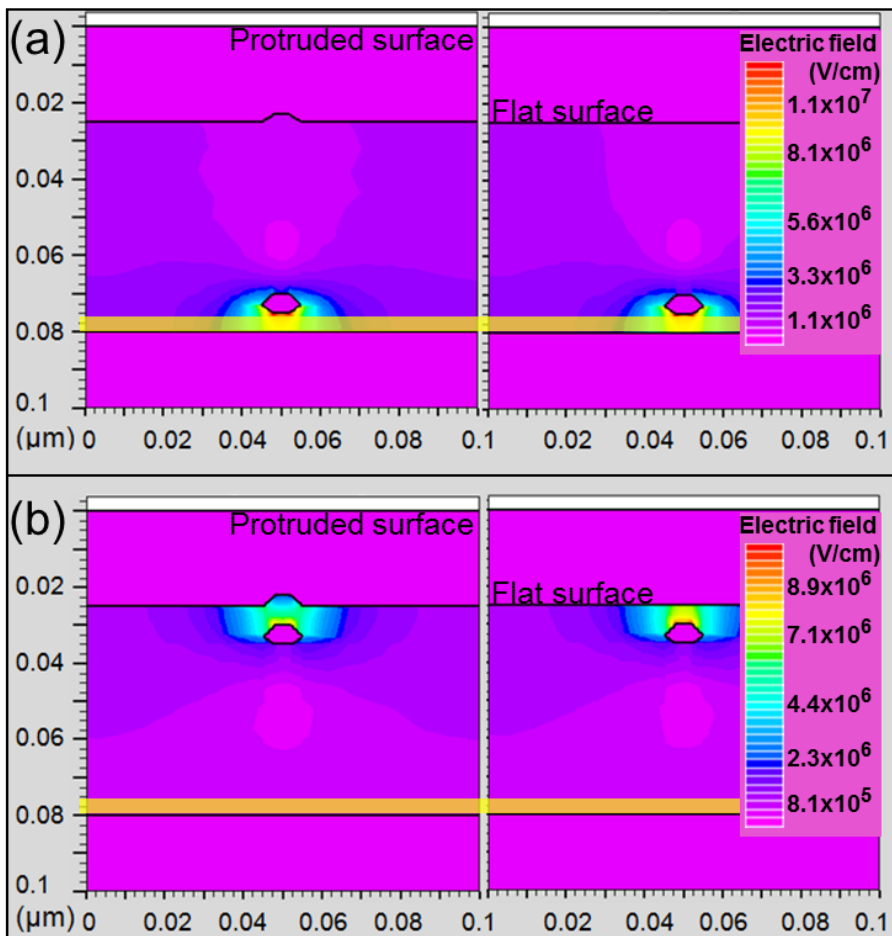


Figure 2. 13. The electric field distribution of (a) b-Ru and (b) t-Ru samples

having the density of Ru nano-dots with $20 \text{ dots}/\mu\text{m}^2$ and $80 \text{ dots}/\mu\text{m}^2$. The field distribution along the bottom interface (marked by the yellow band in the figures) is highlighted in the low panels of each figure. Inset figures of (a) and (b) show electric field distribution near one Ru nano-dot



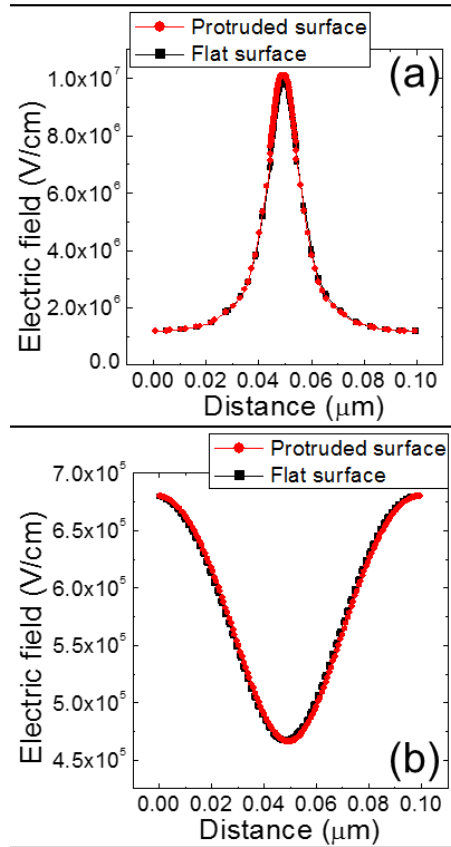


Figure 2. 14. The electric field distribution of (a) b-Ru and (b) t-Ru samples, where the protrusion on the TiO_2 surface by the presence of embedded Ru ND was considered or not. The field distribution along the bottom interface (marked by the yellow band in the figures) is highlighted in the lower panels of each figure. Inset figures of (a) and (b) show electric field distribution near one Ru nano-dot

In addition to the unipolar resistive switching that has been described so far, bipolar resistive switching in TiO_2 is also described within the context of the behavior of conducting filaments, and it is therefore substantially affected by the preferable spots for the growth of conducting filaments. Figure 2.15 (a) shows the typical bipolar resistive switching behavior observed in these TiO_2 films. The bipolar resistive switching in TiO_2 can be triggered after unipolar reset process followed by electroforming. Therefore, the local insulating region where the rupture of conducting filaments took place is the active area contributing to the redox reaction of the bipolar resistive switching. It is assumed that insulating TiO_2 region intervened between the Pt electrode and remaining CF after the URS reset is the active region for the bipolar switching. A remarkable improvement in the endurance performance was found from the bipolar resistive switching in the b-Ru and t-Ru samples compared with n-Ru sample. Figure 2.15 (b) shows the endurance data of n-Ru, b-Ru and t-Ru samples whose HRS and LRS resistance is obtained at 0.2V (read voltage) through DC I-V measurement. The I-V curve of b-Ru and n-Ru depending on the switching cycles are shown in figures 2.15 (c) and (d), respectively. There is little difference among the LRS performance, but a remarkable improvement was achieved from the b-Ru and t-Ru samples for the HRS performance. The uncontrolled formation and rupture of CFs in n-Ru samples may result in the non-optimum configuration of insulating TiO_2 region for the bipolar switching to occur, but the better controlled formation and rupture of CFs in the other cases can results in the more controlled bipolar switching

which is accompanied with the enhanced endurance.

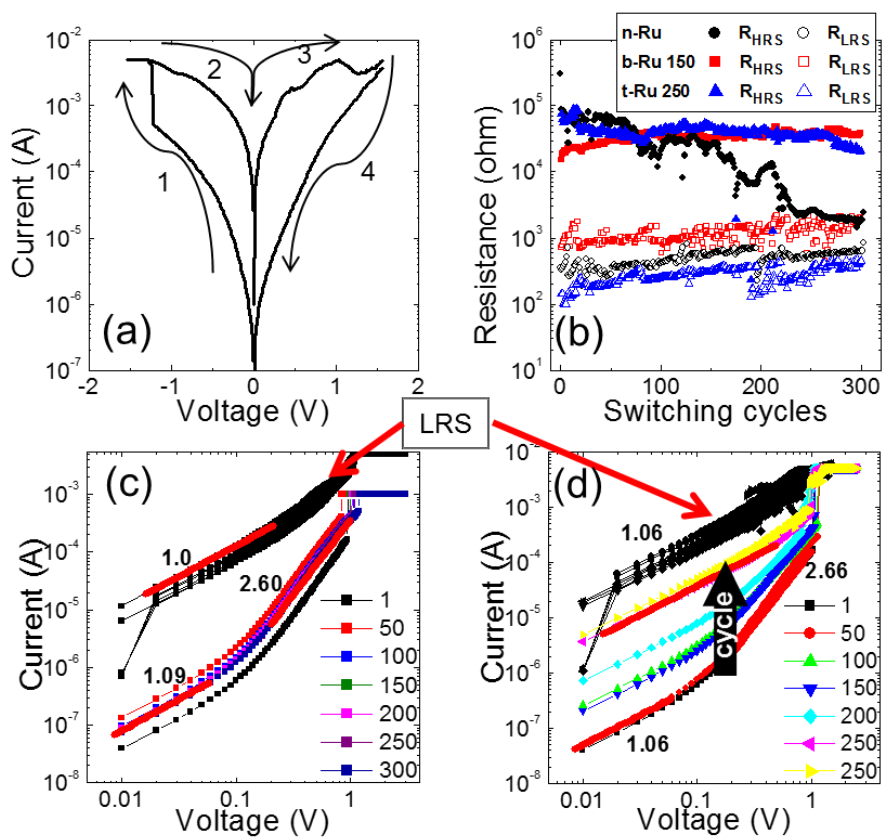


Figure 2. 15. (a) The typical bipolar resistive switching behavior and (b) endurance data of n-Ru, bRu and t-Ru samples. The I-V curve of (c) b-Ru and (d) n-Ru depending on the switching cycles

The URS of the various samples with the negative bias being applied to the top electrode could be also considered, which actually corresponds to the reversed field distribution of figure 2.13. If there were not any differences in the physical situations of the samples, the b-Ru and t-Ru samples must have shown the reversed trend of improvement in the uniformity with respect to the n_{Ru} compared with figures 2.4 and 2.6 under this bias situation, since the structures are simply upside down. However, the experimental results were not in line with this conjecture due to the reasons discussed in figure 2.16. Figure 2.16 shows the electroforming curves of the various samples; (a) shows the sample configuration for the I-V measurements, (b) shows the schematic diagram for the oxygen movement during the electroforming with either negative or positive bias being applied to the top Pt electrode. It can be immediately understood that the electroforming with negative bias was highly unfavorable, and it was even impossible for the t-Ru cases irrespective of the n_{Ru} . This may perhaps be due to the fact that the oxygen atoms must migrate down to the bottom interface and leave the structure at the interface, which is largely hindered by the presence of oxygen non-permeable Si substrate. It has been reported that the application of excessive negative stress actually disturbed the integrity of the structure.[23] so reliable experiments for checking the RS uniformity were not feasible for these sample sets with the negative bias. The evidence of evolution of gaseous oxygen through top electrode is shown in figure 2.17. Figures 2.17 (a) and (b) show the AFM topographic images of an n-Ru sample with a $4 \times 4 \mu m^2$ dimension before and

after electrical forming, respectively. While the pristine sample shows a very uniform and smooth surface morphology, the electroformed sample shows several protruding regions of which locations are not limited to any specific region of the active area. Such phenomenon has been discussed in many other groups.[2] which is related to the evolution of gaseous oxygen.

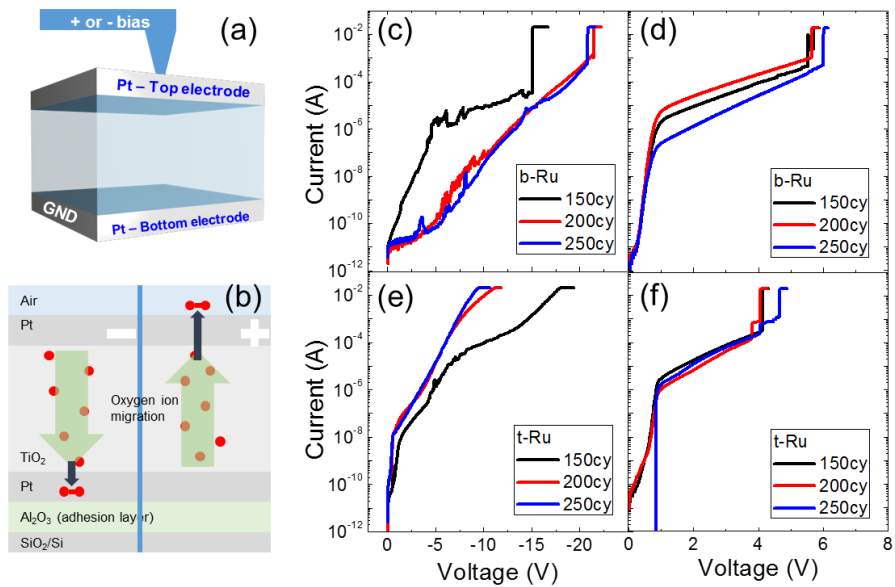


Figure 2. 16. (a) The sample configuration for the I-V measurement and (b) schematic diagram for the oxygen movement during the electroforming with either negative or positive bias. The I-V curve of pristine state in b-Ru ((c) : negative bias, (d) – positive bias) and t-Ru ((e) : negative bias, (f) – positive bias)

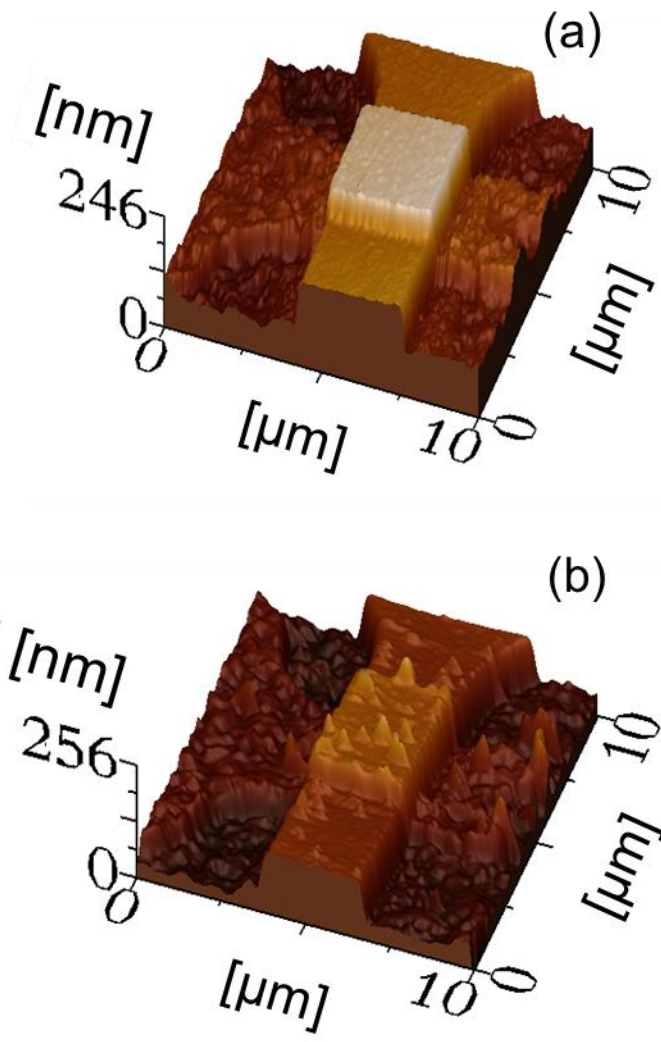


Figure 2. 17. AFM topographic images of an n-Ru sample with a $4 \times 4 \mu\text{m}^2$ dimension (a) before and (b) after electrical forming

It was also noted that the phases of TiO_2 can hardly influence the RS performance. TiO_2 material in b-Ru samples contain an appreciable portion of rutile phase, the crystallization of which was initiated by the Ru-NDs[18],[22] (see also figure 2.2), while t-Ru samples are mostly anatase. It can be understood that the local field distribution and accompanying localized carrier injection almost exclusively govern the RS behavior in these samples containing Ru-NDs, suggesting the irrelevance of TiO_2 phases to the RS. This may be due to the fact that localized heating during the RS by the Joule heating effect actually governs the local phase. Such an improvement in the switching uniformity was also confirmed from the cell-to-cell variations as shown by figure 2.18. Figures 2.18 (a), (b) and (c) shows the switching I-V curves taken from 20 different cells of n-Ru, b-Ru ($n_{\text{Ru}} = 150$), and t-Ru ($n_{\text{Ru}} = 250$) samples with the large capacitor type, as they most clearly show the difference. Although the uniformity was not as good as the repeated switching results from single cells shown in figure 2.4 and 2.5, it is still very obvious that the inclusion of b-Ru and t-Ru largely improved the uniformity.

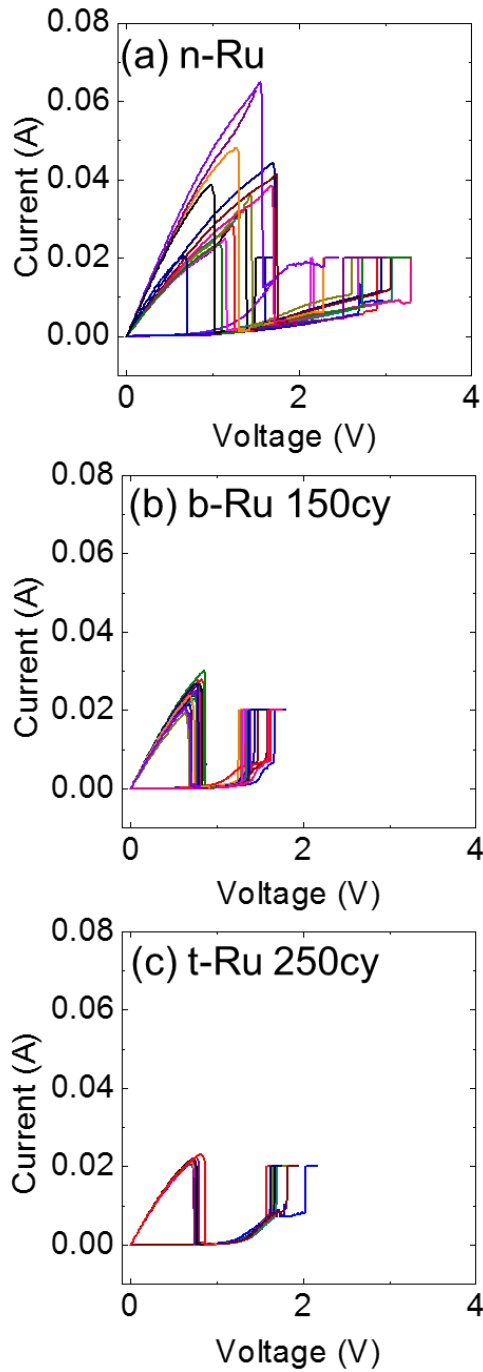


Figure 2. 18. Switching I-V curves taken from 20 different cells of (a) n-Ru, (b) b-Ru ($n_{Ru} = 150$), and (c) t-Ru ($n_{Ru} = 250$) samples with the large capacitor type

2.5. Summary

The substantial improvement in the RS uniformity of TiO₂ memory cells was achieved by adopting Ru-NDs embedded in the TiO₂ layer. It was concluded that limiting the location where electron injection occurs at the cathode interface to a narrower region was the key factor for achieving highly improved RS performance, which can be achieved by including the Ru-NDs. However, depending on their locations relative to the cathode interface, the role of Ru-NDs changes from field-enhancer to field-suppressor. It must be noted that continuous intermediate metal layer cannot play such a role, so that nano-scale dots are necessary for this purpose. The phases of TiO₂ can hardly influence the RS performances. Therefore, a similar improvement could be expected from other types of metal NDs as long as they can be embedded in an appropriate shape and density as in this work. The development of memory cell structure of truly nano-scale size having such a limiting factor for the electric-field distribution can solve the non-uniformity issue of future ReRAM.

2.6. Bibliography

[1] R. Waser, M. Aono, Nat. Mater. **2007**, 6, 833.

[2] D. B. Strukov, G. S. Snider, D. R. Stewart, R. S. Williams, Nature **2008**, 453, 80 .

[3] R. Waser, R. Dittmann, G. Staikov, K. Szot, Adv. Mater. **2009**, 21,

2632.

[4] J. Borghetti, G. S. Snider, P. J. Kuekes, J. J. Yang, D. R. Stewart, and R.S. Williams, *Nature* **2010**, 464, 873.

[5] A. Sawa , *Mater. Today* **2008**, 11, 28.

[6] D. -H. Kwon, K. M. Kim, J. H. Jang, J. M. Jeon, M. H. Lee, G. H. Kim, X.-S. Li, G.-S. Park, B. Lee, S. Han, M. Kim and C. S. Hwang, *Nat. Nanotechnol.* **2010**, 5, 148

[7] M. J. Lee, S. Seo, D. C. Kim, S. E. Ahn, D. H. Seo, I. K. Yoo, I. G. Baek, D. S. Kim, I. S. Byun, S. H. Kim, I. R. Hwang, J. S. Kim, S. H. Jeon, B. H. Park, *Adv. Mater.* **2007**, 19, 73.

[8] P. Strachan, J. Paul, D. Pickett, D. Matthew, J. J. Yang et al. *Adv. Mater.* **2010**, 22, 32.

[9] Y. Yang, P. Gao, S. Gaba, T. Chang, X. Pan, W. Lu, *NATURE COMMUNICATION* **2012**, 3, 732.

[10] G. S. Park, X. Li, D. Kim, R. Jung, M. J. Lee, S. Seo, *Appl. Phys. Lett.* **2007**, 91, 222103.

[11] P. Strachan, J. Paul, J. J. Yang, R. Muenstermann, Ruth, *Nanotechnology* **2009**, 20, 48.

[12] M. H. Lee and C. S. Hwang, *Nanoscale* **2011**, 3, 2.

[13] J. Y. Son and Y.-H. Shin. *Appl. Phys. Lett.* **2008**, 92, 222106.

[14] J. B. Yun, S. Kim, S. Seo, M. J. Lee, D. Kim, S. Ahn, Y. Park, J. Kim, and H. Shin, *PSS-RRL* **2007**, 6, 280

[15] G. H. Kim, J. H. Lee, Y. Ahn, W. Jeon, S. J. Song, J. Y. Seok, J. H.

Yoon, K. J. Yoon, T. J. Park, C. S. Hwang, *Adv. Funct. Mater* **2012**, DOI:10.1002.

[16] W. Guan, S. Long, R. Jia, and M. Liu, *Appl. Phys. Lett.* **2007**, 91, 062111.

[17] W. Chang, K. Cheng, J. Tsai, H. Chen, F. Chen, M. Tsai, and T. Wu, *Appl. Phys. Lett.* **2009**, 95, 042104.

[18] J. H. Yoon, K. M. Kim, M. H. Lee, S. K. Kim, G. H. Kim, S. J. Song, J. Y. Seok, and C. S. Hwang, *Appl. Phys. Lett.* **2010**, 97, 232904.

[19] J.J. Yang, J. Strachan, Q. Xia, D. A. A. Ohlberg, P. J. Kuekes, R. D. Kelly, W. F. Stickle, D. R. Stewart, G. Medeiros-Riveiro, S. Williams, *Adv. Mater.* **2010**, 22, 4034.

[20] K. M. Kim, B. J. Choi, Y. C. Shin, S. Choi and C. S. Hwang, *Appl. Phys. Lett.* **2007**, 91, 012907.

[21] K. M. Kim, D. S. Jeong, C. S. Hwang, *Nanotechnology* **2011**, 22, 254002.

[22] S. K. Kim, K. M. Kim, W. D. Kim, C. S. Hwang and J. H. Jeong, *Appl. Phys. Lett.* **2004**, 85, 4112.

[23] R. Muenstermann, J. J. Yang, P. Strachan, J. Paul, *PSS-RRL* **2010**, 4, 1-2.

3. Self-rectifying Resistive Switching

Phenomena in Pt/Ta₂O₅/HfO₂/TiN structure

3.1. Introduction

Resistance switching random access memory (ReRAM) is attracting a great deal of attention as one of the most promising next-generation non-volatile memory devices especially in the crossbar array (CBA) configuration [1-5]. It currently has several obstacles to overcome, however, such as the high variability in electrical performances, the requirement of an electroforming step, and the necessary integration of a memory cell with selector devices to alleviate the sneak currents in CBA [6]. These problems become even more serious when a three-dimensional (vertical) CBA structure is to be fabricated [6]. The former two problems are generally related to the localized (soft) breakdown of the dielectric layers in many metal-insulator-metal (MIM) structures, which is the typical configuration of memory cells in ReRAM or CBA, to induce the formation of conducting filaments (CF's), while the third problem is more closely related with the integration issues of the device in planar and vertical CBA structures. As the electrical resistance switching (RS) in many reported systems is closely related with the formation and (local) rupture of the CFs in the insulator layer of the MIM structure [7-9], which can usually be initiated by the electroforming step [10, 11], the random

fluctuations of RS parameters, such as the voltages for the switching and current levels in the low resistance state (LRS) and high resistance state (HRS), are somewhat inevitable. This must be more obvious for the cases where the CFs show distinctive phase transition from the insulating mother phase, such as the Magnéli CFs in TiO_2 [7, 12]. In addition, the involvement of the initial electroforming step, which is usually accomplished by adopting a voltage higher than the usual operation voltages, is generally unfavorable for the device fabrication and operation. Therefore, seeking an RS mechanism that does not require an electroforming step, which could also eliminate the involvement of the prominent local CF mechanism, is an important task for the further development of the ReRAM or CBA devices.

The fabrication of selector devices for the random access of the memory cell in their array configuration and integration with the RS memory devices is another crucial task for the successful development of the CBA. The CBA will evolve into the vertically integrated configuration, which does not correspond to the multiple stacking of two-dimensional CBAs [13]. The fabrication of a discrete selector, such as the Schottky diode [14, 15], however, or of highly nonlinear current-voltage (I-V) devices [16-18], and combining them with the RS memory cell, will be very difficult in the vertically integrated structure [6]. Therefore, the development of an RS memory cell that simultaneously contains rectification functionality in itself (self-rectification), highly reproducible RS performance, and electroforming-free characteristics is an impending task.

HfO₂ is a well-known high-k dielectric material for the advanced field effect transistor [19], but it also plays a crucial role in the ReRAM field due to its controllability of resistance values in atomic scale [20, 21]. Ta₂O₅ is also attracting a high level of interest in the ReRAM field as it has shown an exceptionally high switching endurance, especially when combined with a metastable TaO_x (x~2) layer, which serves as the reservoir for the oxygen vacancies (V_o) [5, 22]. These two materials are characterized as lacking in discrete metallic second phases, as opposed to TiO₂ and WO₃, which are characterized as having the conducting Magnéli phases (ca. Ti_nO_{2n-1}, n = 3, 4, 5...) in their heavily reduced state [7, 23]. Therefore, HfO₂ and Ta₂O₅ could have inherently higher uniformity compared with the other materials mentioned above, but many of the switching reports in these materials still utilized the CF-related mechanism, which is induced by the electroforming at voltages higher than that in the usual switching operations [5, 20-22]. In addition, there has been no report on the significantly self-rectifying I-V characteristics of these material systems, where the RS is observed in one bias polarity while the current flow in the opposite bias polarity is largely suppressed.

Meanwhile, electronic RS behaviors have been reported in several material systems, which could be mostly attributed to the trapping and detrapping of carriers (mostly electrons) depending on the bias polarities [24-26]. In contrast to other ionic RS mechanisms, which generally involve the movement of (defective) ionic species during the set (switching from HRS to

LRS) and reset (switching from LRS to HRS) operations, such electronic switching mechanisms induce no or minimal movement of ionic species, making them inherently immune to the large variations in the switching parameters. It has to be noted that the carriers that discern the LRS and HRS are still electrons or holes, not ions, even in the ionic RS systems. The prerequisites for such electronic RS systems are the presence of a mechanism that can induce the bias-polarity-dependent trapping and detrapping of the electronic carriers, and traps that are deep enough to store the trapped carriers for a sufficiently long time under the repeated read operations at the device operation temperatures. These requirements can be met by the deep traps in the band gap of the switching oxide, whose potential barrier must be asymmetric with respect to the bias polarity or different levels of discrete trap states, which respond differently to the bias depending on the resistance states of the sample.

Presented in this work, therefore, is a material system that can provide a very high uniformity in the switching parameters, which can be obtained without the problematic initial electroforming step, and self-rectifying functionality by combining the two promising dielectric materials, HfO₂ and Ta₂O₅. The key component of the idea is that between the two materials, HfO₂ plays the role of the fluent RS layer without requiring the electroforming step while Ta₂O₅ plays the role of a rectifier with the help of a high-work-function metal, which is the top electrode (TE) Pt in this case. To achieve an electroforming-free and highly uniform RS behavior, the initial defect (V_o)

content in the atomic-layer-deposited HfO_2 layer was increased by two means: through the chemical interaction with the TiN bottom electrode (BE) and through the deoxidation effect during the plasma-enhanced atomic layer deposition (PEALD) of the Ta_2O_5 layer on top. Another merit of the present work is that the two functional oxide layers are deposited via ALD (HfO_2) and PEALD (Ta_2O_5), which are the optimal processes for the three-dimensional vertical ReRAM or CBA fabrication. In this structure, the sample with optimized film thicknesses showed highly reliable electronic switching characteristics even at an operation temperature of 85 °C mitigating the concern about the stability of trap-occupied and unoccupied states. This could be ascribed to the deep trap depth in HfO_2 (~1 eV).

3.2. Experiment

Using an 8-inch-diameter-scale traveling-wave-type ALD reactor (CN-1 Co. Plus 200), 10-nm-thick HfO_2 films were deposited on a 50-nm-thick TiN/ SiO_2 /Si wafer, where the TiN wafer was reactively sputter-deposited using a commercial sputtering system (Endura, Applied Materials). ALD of the HfO_2 film was performed using $\text{Hf}[\text{N}(\text{CH}_3)(\text{C}_2\text{H}_5)]_4$ and O_3 as the Hf precursor and oxygen source, respectively. The Hf precursor and O_3 pulse durations were 2 and 3 s, respectively, and Ar purge gas was injected for 9 and 3 s, respectively, after the occurrence of each of these two chemical pulses. The wafer temperature during the deposition was set to 280°C. The PEALD

Ta₂O₅ layer was deposited in another shower-head-type ALD reactor using tert-butylimido-bis(diethylamido)cyclopentadienyltantalum and H₂O-activated plasma (300 W) as the Ta precursor and oxygen source, respectively, at a substrate temperature of 200°C. The PEALD Ta₂O₅ sequence consisted of Ta precursor feeding (5 s), Ar purging (7 s), water vapor pulsing (5 s, plasma power was turned on during the last 4 s), and Ar purging (10 s).

The film thickness, depth profile of each element, and chemical status of the films were examined using an ellipsometer (Gaertner Scientific Corporation, L116 D), AES (Perkin-Elmer, PHI 660), and XPS (ThermoVG, Sigma Probe), respectively. The cross-section of the Pt/Ta₂O₅/HfO₂/TiN sample was observed using a high-resolution TEM (JEOL, JEM-3000F). For electrical measurement, Pt top electrodes were electron-evaporated through a 300- μ m-hole-diameter metal shadow mask and the lift-off process for fabricating samples with different electrode areas (6,500-350,000 μ m²). The self-rectifying resistive switching behavior was measured using an HP4145B semiconductor parameter analyzer at room temperature, in voltage sweep mode. Each voltage sweep began from 0 V, and the bias was applied to the TE while the BE was grounded.

3.3. Structural Properties of the Ta₂O₅/HfO₂/TiN Thin-Film Stack

The cross-section transmission electron microscopy (TEM) images of the Pt/Ta₂O₅/HfO₂/TiN structure are shown in Figure 3.1 (a). The figure shows a well-distinguishable layer structure with a crystallized monoclinic HfO₂ layer, confirmed by the fast-Fourier-transformed image (lower right inset) of the crystalline lattice fringes, and an amorphous Ta₂O₅ layer structure. The HfO₂/TiN interface is also clearly defined, but a small amount of amorphous material can be observed at the mostly-grain-boundary regions of the crystalline TiN, which could be the TiO_xN_y material (left inset). There is no evidently oxidized TiO₂ (or TiO_x, $x < 2$) layer at the interface between HfO₂ and TiN. The well-distinguished Ta₂O₅/HfO₂/TiO_xN_y structure is also confirmed by the depth profiling in Auger electron spectroscopy (AES), as shown in Figure 3.1 (b). The influence of depositing the Ta₂O₅ layer via PEALD on top of the HfO₂ layer can be more evidently understood via X-ray photoelectron spectroscopy (XPS). Figures 3.2 (a) and (b) show the Ta *4f*/ Hf *4f*, and O *1s* core levels in the XPS depth profile results of the Ta₂O₅(5nm)/HfO₂(10nm)/TiN sample. For the XPS measurement, the Ar⁺ ion beam energy was set to 1 keV during the sputter-etching. The core-level data for N *1s* and Ti *2p* were also shown in figure 3.2 (c) and (d), respectively. The core levels were shown with regard to the etch level, where the time between the levels was ~10 s. The binding energy of Ta *4f* well coincided with the

reported value of the Ta $4f$ peak (26.2 eV for Ta $4f_{7/2}$ and 28.1 for Ta $4f_{5/2}$, indicated by the yellow vertical dashed lines in Figure 3.2 (a)) in Ta₂O₅ [27, 28]. The emergence of the peaks near the binding energy of ~22-24 eV was an artifact that originated from the preferential etching of oxygen atoms by the Ar⁺ ion bombardment. This suggests that the underlying HfO₂ layer had no significant influence on the chemical properties of the Ta₂O₅ layer. A significant change in the binding energy of Hf $4f$ was observed, however, as the XPS probing depth changed from the Ta₂O₅/HfO₂ interface region to the bulk HfO₂ region. The binding energy of the Hf $4f$ core levels shifted to a lower binding energy direction near the interface region with the Ta₂O₅ layer (indicated by the brown vertical dashed lines), which recovered the value of the reported Hf $4f$ binding energy (17.6 eV for Hf $4f_{5/2}$ and 19.2 for Hf $4f_{3/2}$, indicated by the black vertical dashed lines) of HfO₂ [29] as it moved away from the interface. The weak peaks near the binding energy of ~13-15 eV were also due to the preferential etching of oxygen atoms from the HfO₂ layer during the XPS depth profiling. The presence of a lower binding energy peak of Ta $4f$ up to the etching level of 13 did not necessarily suggest that Ta₂O₅ was intermixed with HfO₂, but this was believed due to the artifact produced by preferential etching considering the AES profile shown in figure 3.1 (b). This result implies that HfO_{2-x} are formed near the Ta₂O₅ thin-film layer during the PEALD process of the Ta₂O₅ layer. It appears that the impingement effect of ions during the PEALD of the Ta₂O₅ layer induced such defects in the HfO₂ layer. The XPS core levels of O $1s$, N $1s$, and Ti $2p$ shown in Figure

3.2 (b), (c) and (d) did not show any notable feature, except for the slight shift of the O $1s$ peak position to the high-binding-energy direction as the layer changed from Ta₂O₅ to HfO₂. The binding energy of N $1s$ coincided well with the reported value of the N $1s$ peak (397.4 eV for N $1s$, indicated by the yellow line) in TiN [SI-1]. The Ti $2p$ peak well matches the reported Ti $2p$ binding energy (460.9 eV for Ti $2p_{1/2}$ and 454.92 for Ti $2p_{3/2}$, indicated by the blue vertical dashed lines) of TiN [SI-2, 3]. The slight bump near binding energy ~404 in the N $1s$ spectra was due to the Ta $4p$ core level. The presence of O $1s$ at etching level >14, which corresponds to mainly TiN, confirmed that the TiN BE was partly oxidized, as shown in figure 3.1 (a). The precise coincidence between the emergences of the Ti and N peaks suggested that the interface between HfO₂ and TiN BE could be quite abrupt, which was consistent with the TEM results shown in figure 3.1 (a). These results suggested that depositing the PEALD Ta₂O₅ layer on top of ALD HfO₂ induced a deoxidizing effect on the HfO₂ layer while the Ta₂O₅ layer itself had a low defect concentration. The application of plasma power during the Ta₂O₅ deposition appeared to impose such deoxidizing effect on the underlying HfO₂ layer. This effect was well represented by the electrical performances of the single and stacked dielectric-layer samples described in the following section.

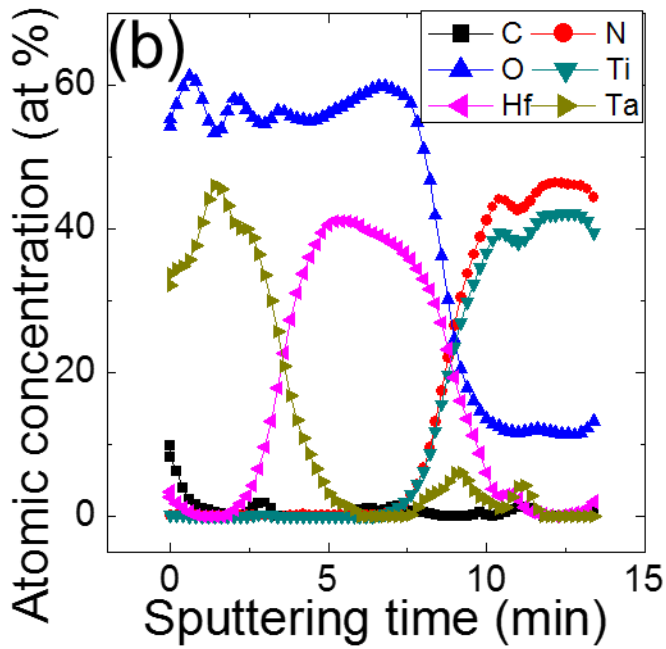
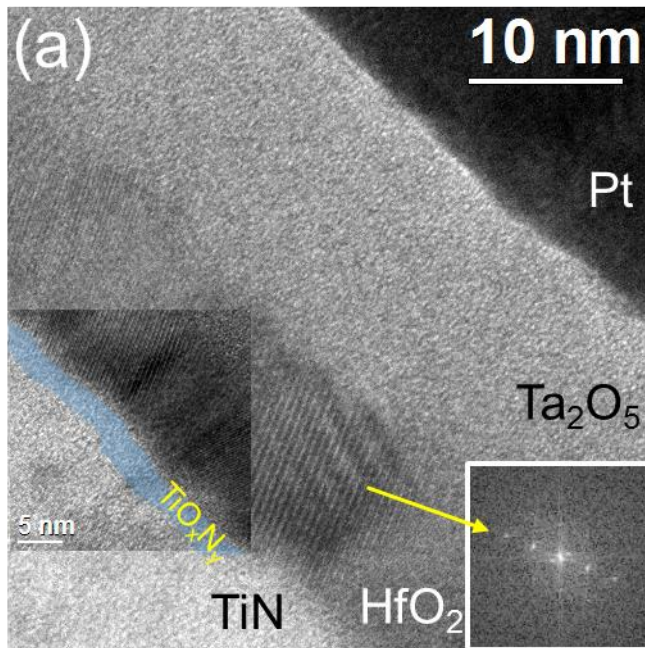
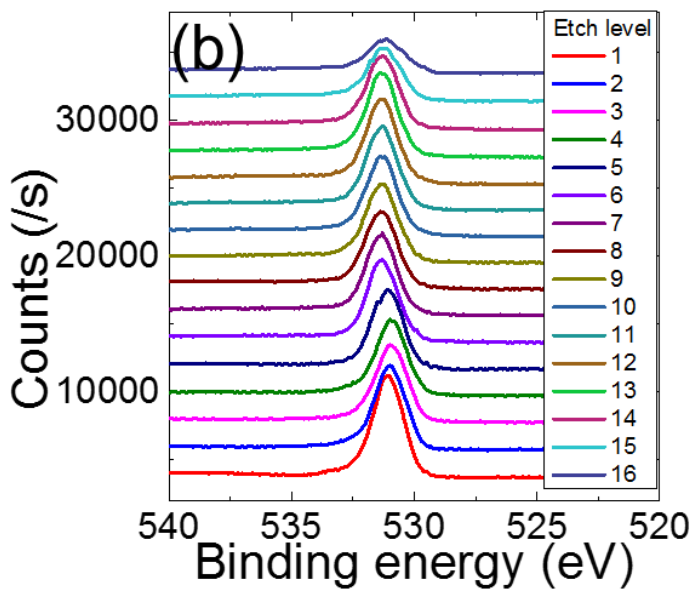
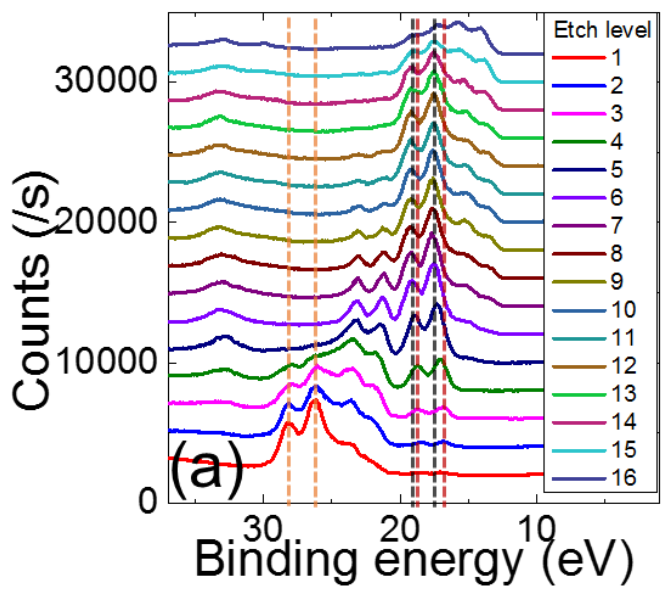


Figure 3. 1. (a) Cross-section TEM images and (b) depth profiling AES data of the Pt/Ta₂O₅(10nm)/HfO₂(10nm)/TiN sample



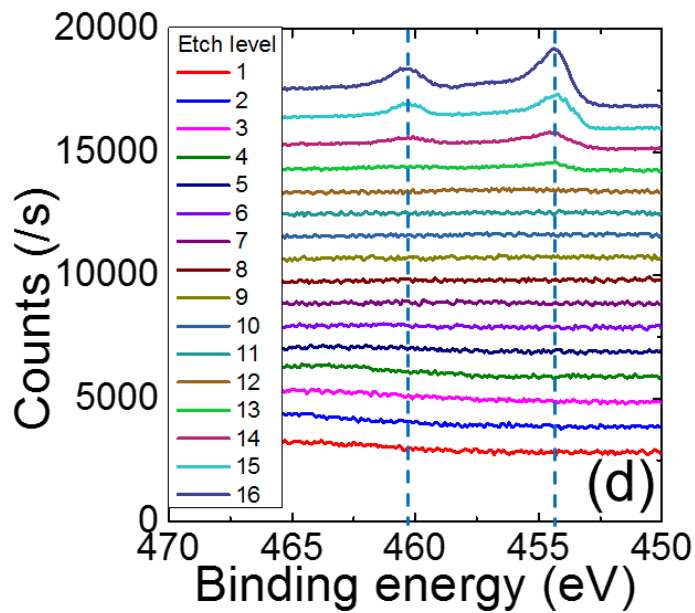
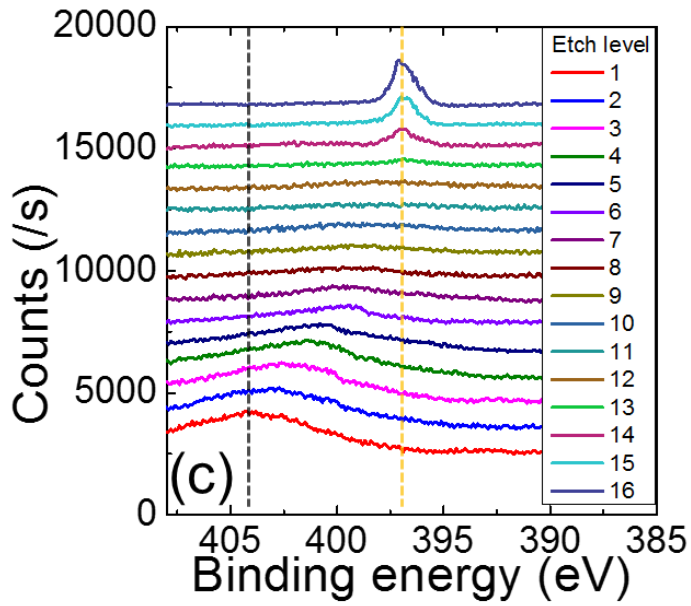


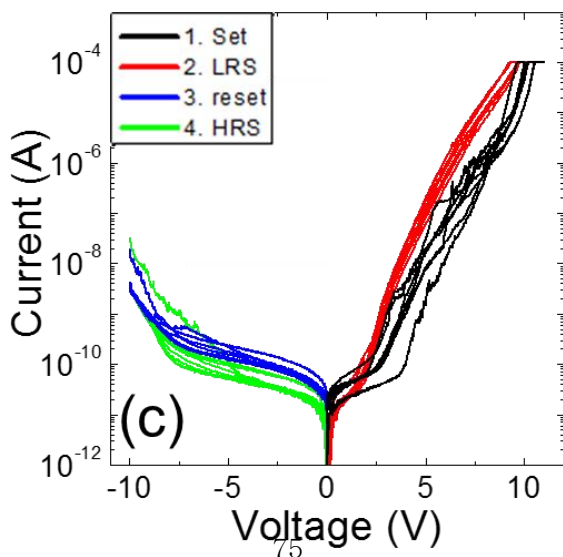
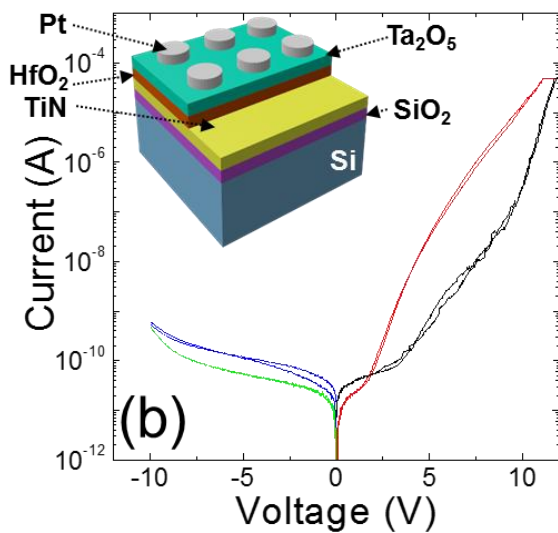
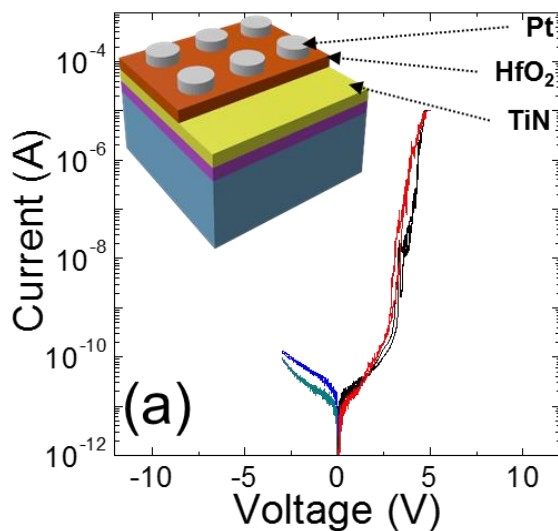
Figure 3. 2. (a) Ta $4f$ / Hf $4f$, (b) O $1s$, (c) N $1s$ and (d) Ti $2p$ core levels in the XPS depth profile results of the Ta₂O₅(5nm)/HfO₂(10nm)/TiN sample

3.4. Electrical Performances of the Memory Cell and Switching Mechanism

Figures 3.3 (a) - (d) show the RS I-V curves of the Pt/10-nm-thick HfO₂/TiN, Pt/5-nm-thick Ta₂O₅/10-nm-thick HfO₂/TiN, Pt/10-nm-thick Ta₂O₅/5-nm-thick HfO₂/TiN, and Pt/10-nm-thick Ta₂O₅/10-nm-thick HfO₂/TiN samples, respectively. The inset figures in figures 3.3 (a) and (b) show the schematic diagrams of the samples with single and stacked dielectric layers. For these I-V tests, Pt TE was biased while TiN BE was grounded, and the compliance current (I_{cc}) was set at between 10 and 100 μ A to prevent not only the complete breakdown of the sample but also the emergence of the usual bipolar type switching. The usual bipolar-type switching characteristics are shown in figure 3.3 (e). Briefly, it required electroforming in the negative bias voltage region with the typical electroforming voltage and the current levels of \sim -10 V and 1 μ A. This corresponds to ionic switching where the high Schottky barrier at the Pt/HfO₂ or Pt/Ta₂O₅ is locally disrupted and recovered by the drifting movement of the oxygen ions while the oxide/TiN interface maintained (quasi-) Ohmic contact. In contrast, such usual ionic RS mechanism was strictly prohibited in this work by adopting set and reset switching in positive and negative bias polarities, respectively, while the minimum (maximum absolute) voltages in the negative bias region was controlled so as not to induce a large leakage current in that bias region. All the samples showed high resistance in the pristine state, as can be seen from

the first set of I-V curves (black lines). Among these samples, the Pt/10-nm-thick Ta₂O₅/10-nm-thick HfO₂/TiN sample (figure 3.3 (d)) shows a highly desirable RS performance, as will be discussed in detail later. Three notable features could be found in figure 3.3. First, the single HfO₂ layer did not show feasible RS behavior (figure 3.3 (a)). This sample generally shows an asymmetric I-V shape, where the much more fluent electron injection at the HfO₂/TiN interface under the positive bias compared with the suppressed electron injection at the Pt/HfO₂ interface under the negative bias is the reason for the asymmetry. Second, the stacked dielectric layer shows desirable RS curves in the positive bias region when the HfO₂ layer thickness was 10 nm while the current in the negative bias region was generally very low in a wide voltage range irrespective of the resistance state of the samples. Third, a large-enough and clearly distinguishable resistance ratio between the HRS and LRS could have been achieved only when both the HfO₂ and Ta₂O₅ layers were 10-nm-thick (figure 3.3 (d)). These three findings suggest that any change in the sample that induced the RS was confined within the HfO₂ layer while the high Schottky barrier at the Pt/Ta₂O₅ interface remained intact during all the switching cycles. Based on the I-V characteristics shown in figure 3.3, the Pt/10-nm-thick Ta₂O₅/10-nm-thick HfO₂/TiN sample was chosen, and its detailed RS performances were examined. The general switching sequences are shown by the numbers included in figure 3.3 (d): the I-V curves of the pristine state (curve 1, open square symbol); the LRS (curve 2, red line), which was induced by the first voltage sweep up to +12 V with an I_{cc} of 10 μA;

the resetting curve (curve 3, blue line), where the voltage was swept down to -10 V; the HRS (curve 4, green line), which was induced by the previous voltage sweep into the negative voltage direction; and the setting curve (curve 5, black line) in the positive voltage region, which set the sample to the LRS again. The almost identical shapes of curves 1 and 5 reveal that this was the electroforming-free sample. The resistance ratio between HRS and LRS and the rectification ratio (the current ratio between the positive (LRS) and negative voltages) as a function of absolute voltage was included in the inset figure in figure 3.3 (d). A maximum resistance ratio of $\sim 10^3$ and a rectification ratio of $\sim 10^4$ were achieved. The resistance ratio was high enough for the high-density CBA (Mb block density), but the rectification ratio should be improved [4]. In addition, the voltage range for achieving those performances was generally too high, and as such, further engineering works are required to address these two problems. Nevertheless, the present work was devoted to the possible fabrication of an electroforming-free, highly uniform, and self-rectifying RS device structure, and to the elucidation of the underlying mechanism.



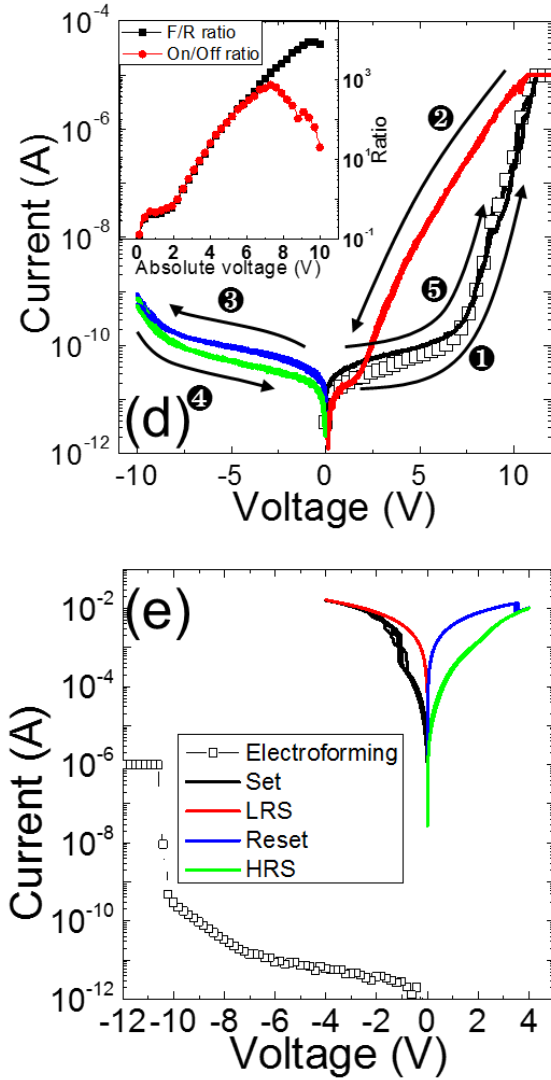
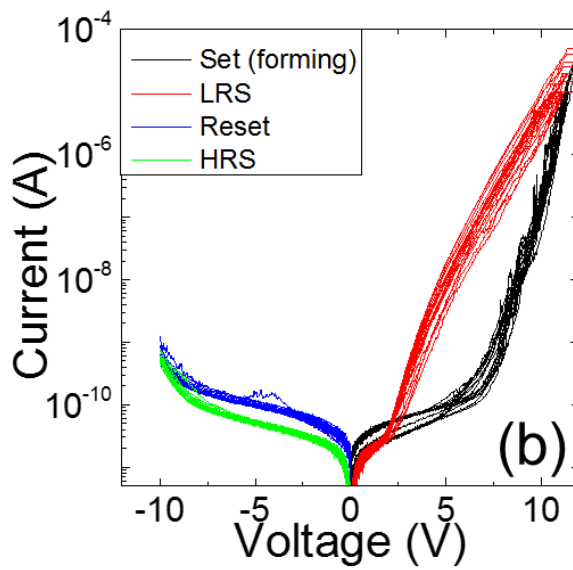
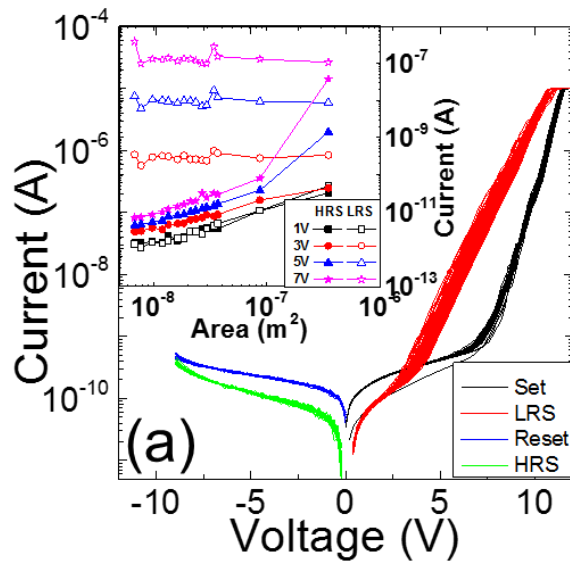


Figure 3. Resistive switching I-V curves of the (a) Pt/10-nm-thick HfO₂/TiN, (b) Pt/5-nm-thick Ta₂O₅/10-nm-thick HfO₂/TiN, (c) Pt/10-nm-thick Ta₂O₅/5-nm-thick HfO₂/TiN, and (d) Pt/10-nm-thick Ta₂O₅/10-nm-thick HfO₂/TiN samples. Schematic diagrams of the samples with (inset figure of (a)) single and (inset figure of (b)) stacked dielectric layers. (inset figure of (d)) Resistance ratio between HRS and LRS, and rectification ratio (current ratio between the positive (LRS) and negative voltages) as a function of absolute

voltage. (e) The conventional bipolar resistive switching behavior in the Pt/Ta₂O₅(10nm)/HfO₂(10nm)/TiN sample. The electroforming was initially performed in the negative bias voltage region with the typical electroforming voltage and the current levels of ~-10 V and 1 μA. This was not the desired switching operation in this work

Figures 3.4 (a) and (b) represent the exceptionally high uniformity of the RS performances within one dot (300 μm diameter) up to 100 I-V sweep cycles, and within 20 dots in a single sample, respectively. The cumulative probability of the current levels of the LRS and HRS in the positive and negative bias voltage regions at particular read voltages (6, 7, and 8 V) is shown in figure 3.4 (c), where the set and reset voltages were 12 and -8 V, respectively, and the I_{cc} was 10 μA . The distributions were extremely narrow, suggesting the exceptional uniformity of the various resistance states.

Figure 3.4 (d) shows the retention data of the LRS and HRS at room temperature and at 85°C up to 10^6 s. Both the HRS and LRS stably retained their current values (measured at 6 V) at room temperature, but the HRS current increased by about one order of magnitude after $\sim 10^3$ s at 85°C. The current ratio was maintained at $\sim 10^2$, however, even after the degradation, showing the high feasibility of the present material's use as the RS element in ReRAM or CBA. The TE-area-dependent current values of the HRS and LRS read out at different voltages are shown in the inset figure in figure 3.4 (a), where the TE area varies ~ 50 times (6,500-350,000 μm^2). It is worth noting that the LRS current was almost completely independent of the TE area, suggesting that the LRS current flowed along a limited number of local spots. In contrast, the HRS current almost linearly varied according to the TE area, suggesting that the leakage current flowed uniformly across the whole TE area when the local conducting paths were removed by reset operation.



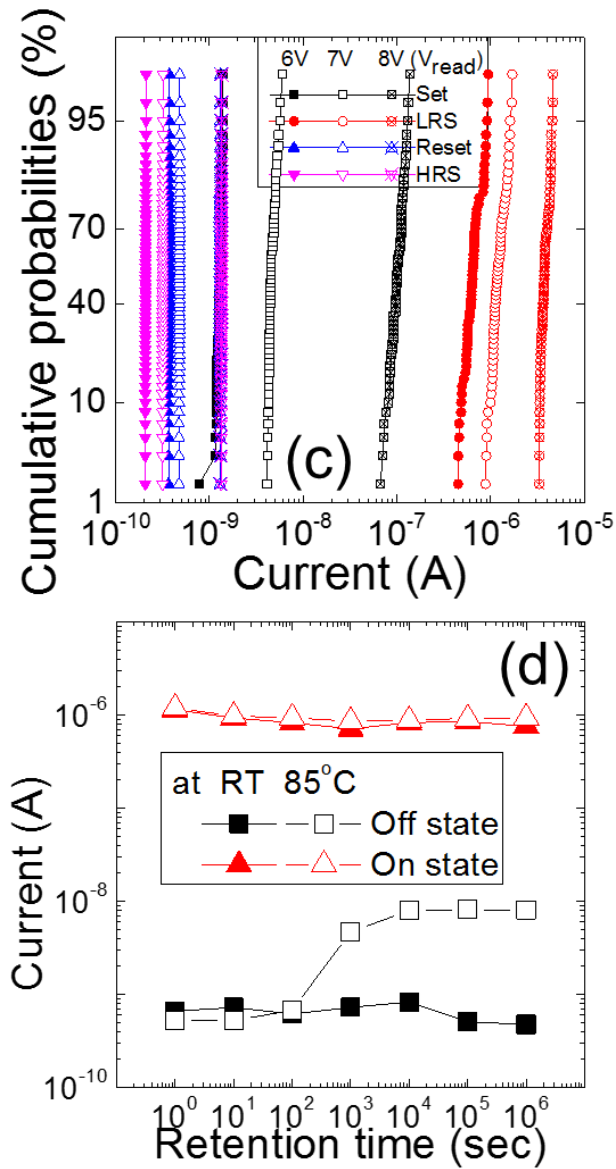
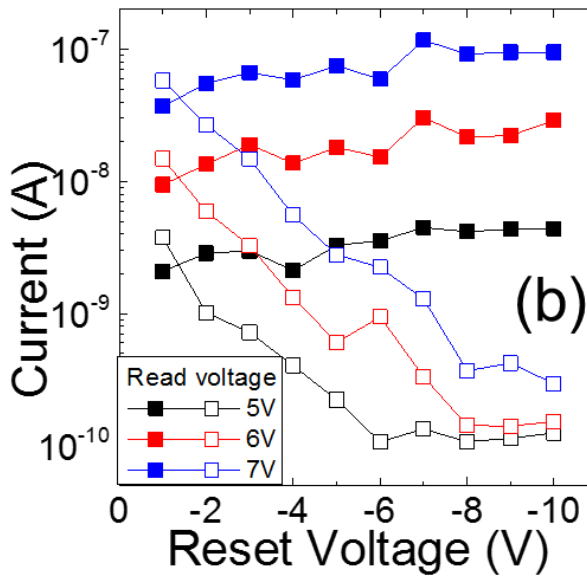
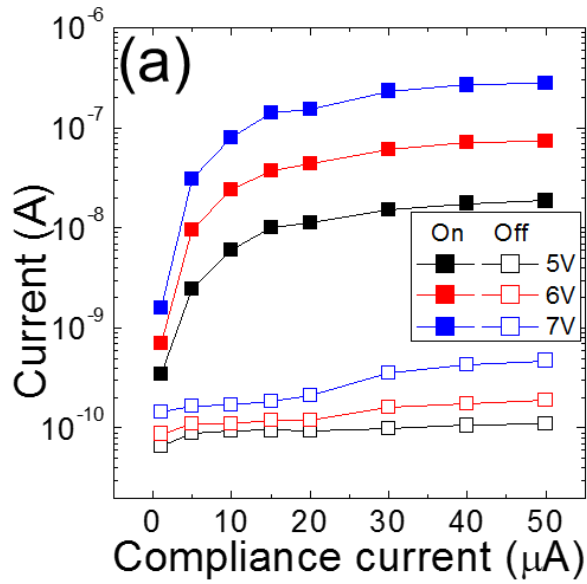


Figure 3. 4. Exceptionally high uniformity of the RS performances within (a) one dot (300 μm diameter) up to 100 I-V sweep cycles, and (b) 20 dots in a single sample; (c) cumulative probability of the current levels of LRS and HRS in the positive and negative voltage regions at particular read voltages (6, 7, and 8 V); and (d) retention data of the LRS and HRS at room temperature and 85°C up to 10^6 s (measured at 6 V)

Figures 3.5 (a) and (b) show another crucial merit of this RS system, which must be contributed by the uniform switching behavior. Figures 3.5 (c) and (d) show the switching I-V curves with different I_{cc} values, and the reset voltage in the self-rectifying mode. The set graphs and low resistance state (LRS) curves are depicted in figure 3.5 (c) with open and closed square symbols, respectively, with different I_{cc} values (from 1 to 50 μA). The sequence for obtaining the dependency of the HRS and LRS currents on different I_{cc} values was as follows. First, set operation is performed with a particular I_{cc} value in the positive bias condition. Second, LRS is checked with the same positive bias. Finally, the reset process is carried out with -10 V for recovering the HRS. After the completion of this single sequence, the experiment was repeated at an increased I_{cc} value. The dependency of the HRS and LRS currents on different reset voltages was tested as in the above experiment: First, set operation was conducted in the positive bias condition, with an I_{cc} of 10 μA . Second, the reset process was carried out with a particular reset voltage. Finally, the HRS current level was measured. After the completion of the single sequence, the experiment was repeated at a decreased reset voltage, and the results are shown in figure 3.5 (d). When the I_{cc} was lower than $\sim 15 \mu\text{A}$, the LRS current increased rapidly as the set switching occurred with the increasing I_{cc} . In figure 3.5 (a), the variations in the HRS and LRS currents measured at 5, 6, and 7 V, respectively, are shown as a function of I_{cc} during the set switching, when the reset operation was performed by sweeping the voltage to -8 V after each set switching. When the I_{cc} became higher than ~ 20

μA , however, the LRS current was saturated at a certain value, meaning that the uncontrolled variations that might occur during set switching could be well suppressed. Figure 3.5 (b) shows that the HRS current was also saturated at a certain level, even when the reset voltage decreased to sufficiently low values. These two factors suggested that the switching mechanisms in this material system were not controlled by the creation and rupture of the conduction channels that could have been contributed by the drift and diffusion of the ionic defects, such as the oxygen vacancies. In the following, the possible reasons for such exceptional performance are discussed, based on the electrical-conduction mechanisms of the HRS and LRS.



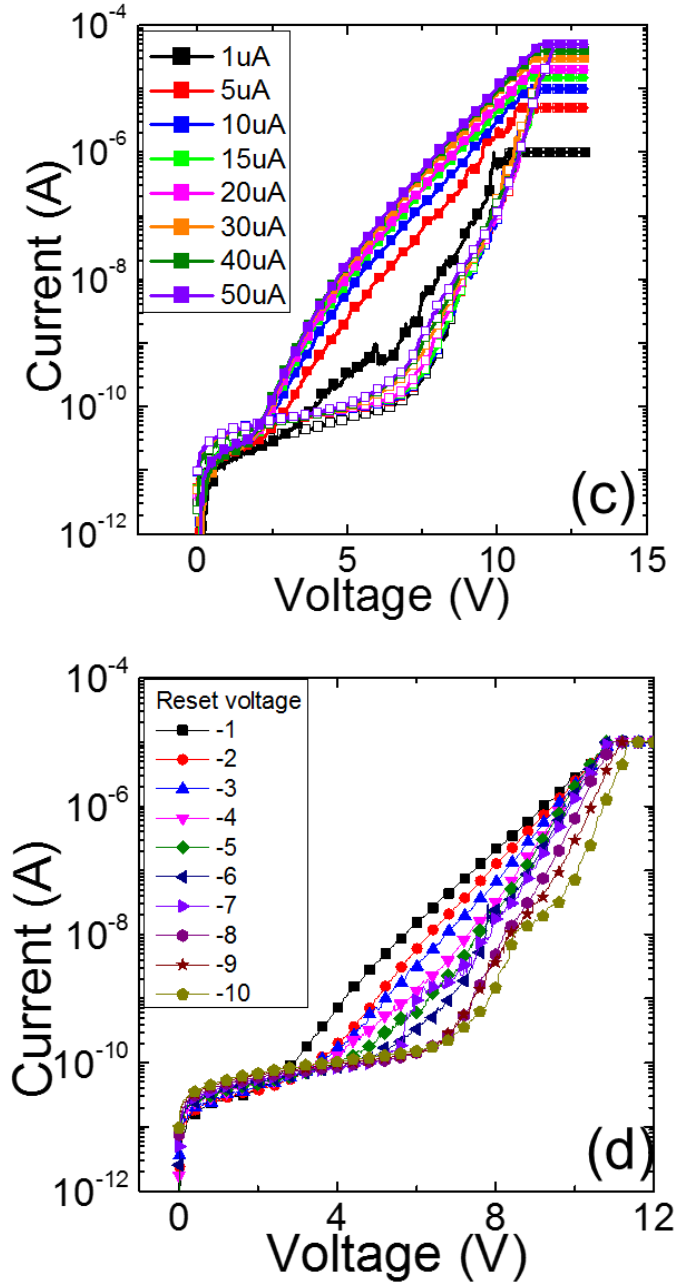
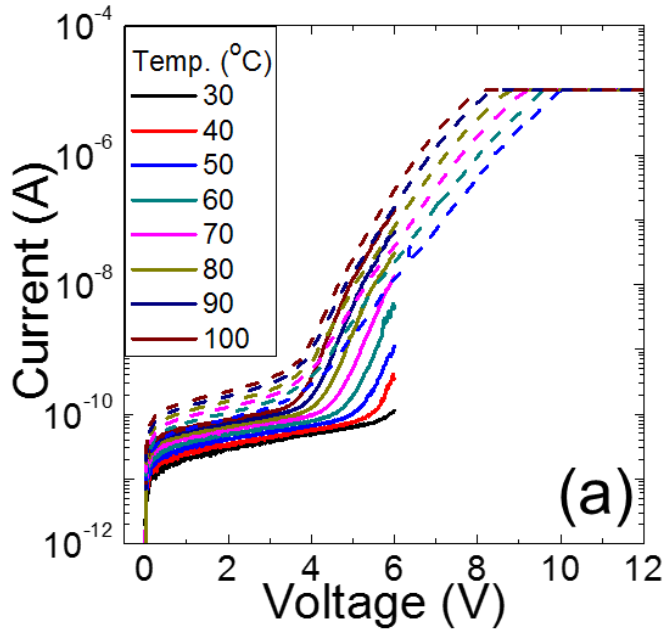


Figure 3. 5. Variations of the current level in the HRS and LRS, measured at 5, 6, and 7 V, respectively, as a function of the (a) I_{cc} during the set switching, and (b) reset voltage during the reset switching. The switching I-V curves with different (c) I_{cc} values, and (d) reset voltage

Figure 3.6 (a) shows the I-V curves of the LRS (dashed lines) and HRS (lines) measured at different temperatures ranging from 30 to 100°C. Here, the HRS was attained by applying -10 V, and the LRS, by applying +12 V, with an I_{cc} of 10 μ A. In both states, the current generally increased with the increasing temperature, suggesting a thermally activated mechanism. It was also evident that the voltage regions could be divided into two regions according to the current increase rate. In the low-voltage regions, both states showed a gradual increase in current, while in high-voltage regions, the current increased at a much higher rate with the voltage and temperature. For the assessment of the current conduction mechanism in the low-voltage regions, the currents at 1.0-2.5 and 1.4-2.9 V for the LRS and HRS, respectively, were plotted according to the Arrhenius form ($\ln I$ vs. $1/T$), and the activation energies (E_a) were extracted at each voltage from the best-linear-fit graphs of the data. Figures 3.6 (b) and (c) show the $\ln I$ vs. $1/T$ results for HRS and LRS, respectively, and the two inset figures show the variations in the E_a for HRS and LRS. Although the plots were not shown, the $\log I$ vs. $\log V$ curves in the low-voltage region showed a slope very close to 1 for both cases. The E_a values were relatively small and were not very different for both states (0.15-0.21 eV). It is believed that the V_o 's were dispersed within the HfO_2 layer and acted as the trap sites for the injected carriers in both states. As the band gap of Ta_2O_5 is lower than that of HfO_2 (~ 5.68 and ~ 4.2 eV in HfO_2 and Ta_2O_5 , respectively, estimated via Auger-electron spectroscopy reflective electron energy loss spectroscopy and spectroscopic ellipsometry, respectively), the

electrons transported to Ta₂O₅ easily moved to Pt TE via the conduction within the CB of the Ta₂O₅ layer, so that the Ta₂O₅ layer did not interfere with the current conduction under the positive bias condition. The almost identical I-V curves of the pristine and HRS samples suggested that the distribution of V_o's within the HfO₂ layer did not vary during the repeated switching.



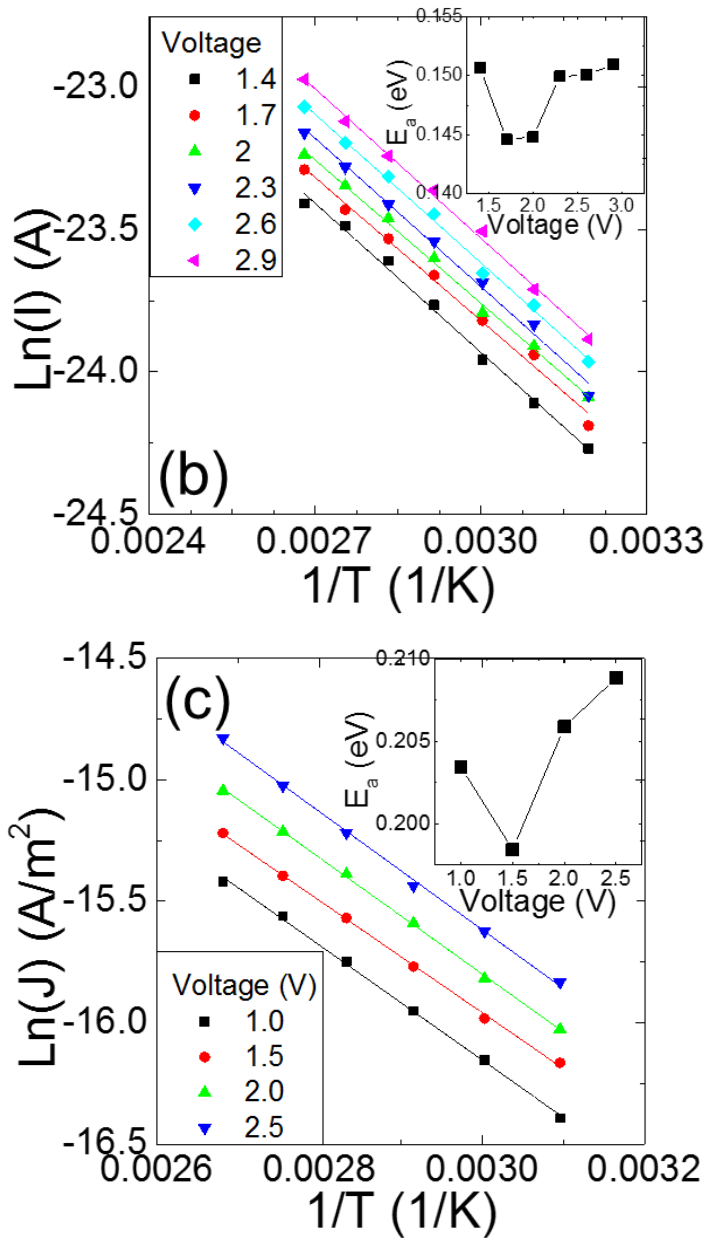
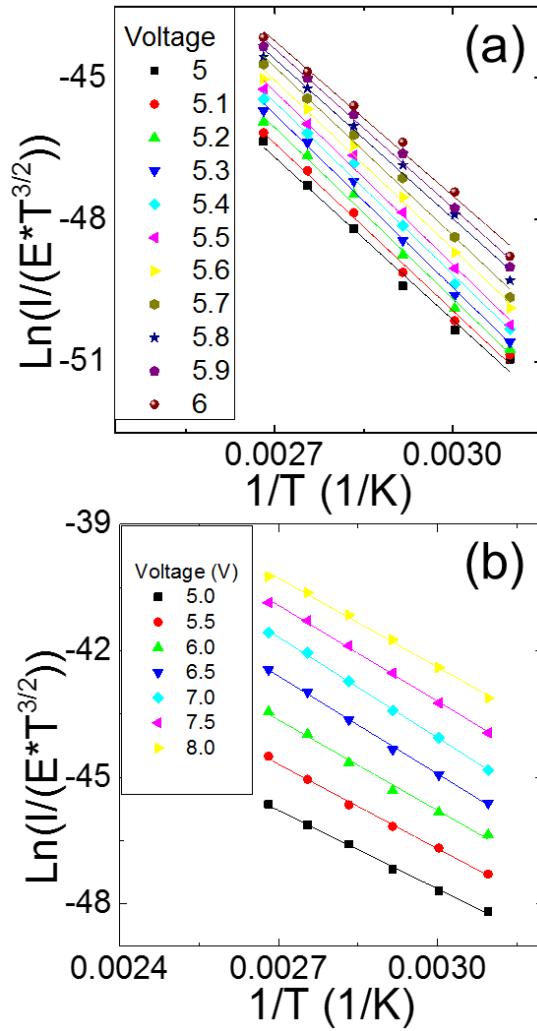


Figure 3. 6. (a) I-V curves of the LRS (dashed lines) and HRS (solid lines) samples measured at different temperatures ranging from 30 to 100°C. Arrhenius form ($\text{Ln } I$ vs. $1/T$) plot in (b) HRS and (c) LRS, and (inset figures of (b) and (c)) activation energies (E_a) extracted at each voltage from the best-linear-fitting of the data in HRS and LRS

The critical differences between the currents of HRS and LRS could be found in the high-voltage region, and the I-V curves in the high-voltage region were attempted to be fit with the Poole-Frenkel (P-F), Schottky, and tunneling mechanisms. The best results were achieved from the P-F fitting, and the plots in the form of $\ln(I/(E \cdot T^{3/2}))$ vs. $1/T$ according to the P-F equation for the voltages ranging from 5 to 6 V and 5 to 8 V are shown in figure 3.7 (a) and (b) for the case of HRS and LRS, respectively. The results fit quite well with the P-F mechanism. For these fittings, the electric field (E) was calculated by dividing the voltage applied over the HfO₂ layer, which could be estimated from the thicknesses and dielectric constants of HfO₂ (10 nm, 18) and Ta₂O₅ (10 nm, 25) and the total applied voltage, with a thickness of HfO₂, suggesting that the conduction was really governed by the HfO₂ layer. From the slopes of the best-linear-fitted graphs at each voltage, the activation energy, which corresponded to the trap depth at each voltage, could be achieved, and the results are summarized in the upper panels (left for HRS and right for LRS) of figure 4.7 (c). The estimated trap depths for HRS and LRS were ~1.0 and ~0.6 eV, respectively. The accuracy of these P-F could be confirmed by the following plots of the I-V curves according to another formalism of the P-F equation: $\ln(I/E)$ vs. $E^{1/2}$ graphs, which were also shown in figure 4.7 (d) and (e). They also showed a nice linear relationship in the high-voltage region, and from the slopes of the best-linear-fitted graphs, the dielectric constant could be estimated, which are summarized in the lower panels (left for HRS and right for LRS) of figure 4.7 (c). While there were

some variations according to the resistance states and temperatures, the estimated values of 3.8-5.9 coincided reasonably well with the optical dielectric constant of ~ 3.9 calculated from the square of the refractive index ($n \sim 1.9$).



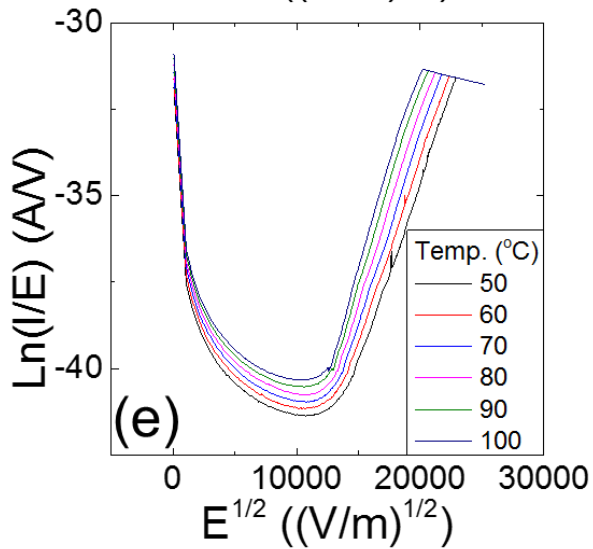
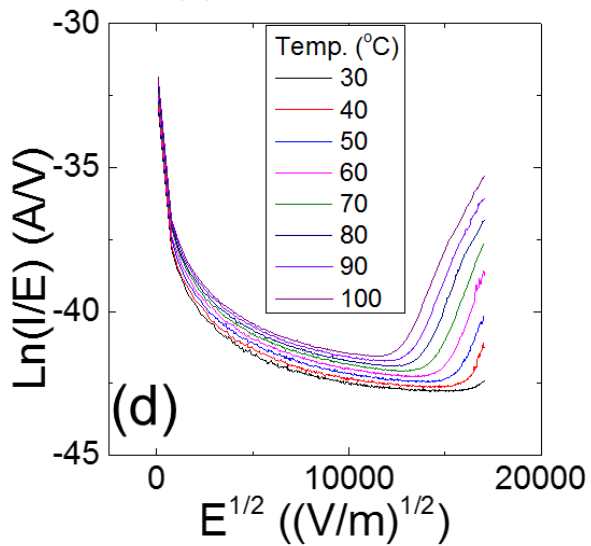
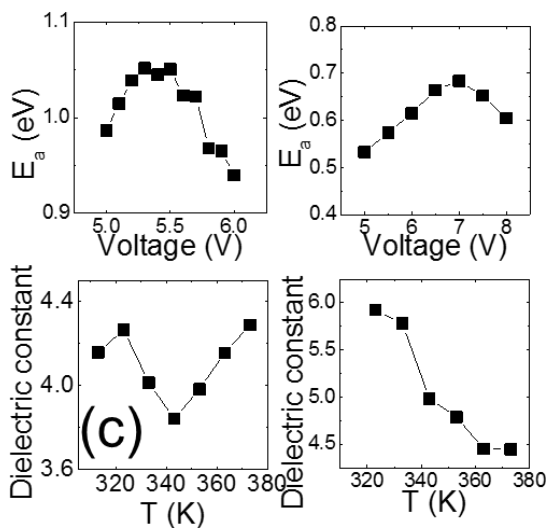
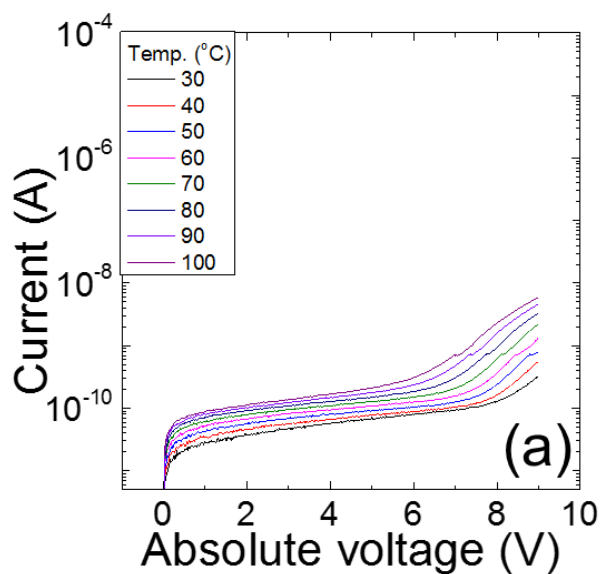


Figure 3. 7. P-F fitting and the plots in the form of $\ln(I/(E \cdot T^{3/2}))$ vs. $1/T$ according to the P-F equation for the voltages ranging from 5 to 6 V in (a) HRS and 5 to 8 V in (b) LRS. (Upper panels of (c)) Activation energy, corresponding to the trap depth at each voltage in HRS and LRS (left for HRS and right for LRS), and (lower panels of (d)) dielectric constant at each temperature. P-F plots in the form of $\ln(I/E)$ vs. $E^{1/2}$ according to the P-F equation in (d) HRS and (e) LRS, respectively

When Pt TE was negatively biased, conduction mechanism analysis was similarly attempted, as shown in figure 3.8. Under this bias condition, the current was generally low in a wider voltage range, and the activation energy obtained from the slopes of the best-linear-fitting $\ln(J)$ vs. $1/T$ graph at voltages ranging from -1 to -5 V was ~ 0.16 eV shown in figure 3.8 (b). The $\log I - \log V$ graphs in the same voltage region showed a slope of ~ -1 , suggesting that the current conduction in this voltage region was also governed by the trap-assisted hopping mechanism. The almost identical E_a to the case where the TE was positively biased, estimated in figure 3.6, suggests that the small leakage current was also governed by the shallow traps in HfO_2 .

For the lower-voltage (high-absolute-value) region, where the current increased exponentially with the voltage and temperature, the I-V curves in that region were plotted according to the P-F, Schottky, and tunneling equations. It was found that only the Schottky mechanism well fit the experimental data, and the $\ln(I/T^2)$ was plotted vs. $1/T$ at voltages ranging from 8.3 to 8.7 V (Figure 3.8 (c)). The slopes of the best-fit graphs corresponded to the Schottky barrier height at a given E ($\psi_0 - \beta_s E^{1/2}$, where ψ_0 and β_s are the zero-field Schottky barrier height and Schottky coefficient, which is determined by the optical dielectric constant). The $\psi_0 - \beta_s E^{1/2}$ values were plotted as a function of $E^{1/2}$ in the inset figure in figure 3.8 (c), whose best-linear-fitting gave the ψ_0 value of ~ 0.70 eV and the dielectric constant of ~ 4.2 , which was close to the estimated value with the refractive index (~ 2.0) of Ta_2O_5 from the ellipsometry. For this estimation, the electric field E was

taken from the voltage applied over the Ta₂O₅ layer and its thickness. This estimation suggests that the low leakage current in the negative bias region was due to the suppression of the carrier injection from the Pt to the Ta₂O₅ layer by the presence of a high Schottky barrier (~0.70 eV), which appeared to have remained intact irrespective of the resistance states in the positive bias region. This was the main reason for the achievement of a high rectification ratio. The 0.70 eV Schottky barrier does not correspond to the ideal Schottky barrier at the Pt/Ta₂O₅ interface, which could be lowered by several factors, pinning the Fermi level close to the conduction band (CB) edge.



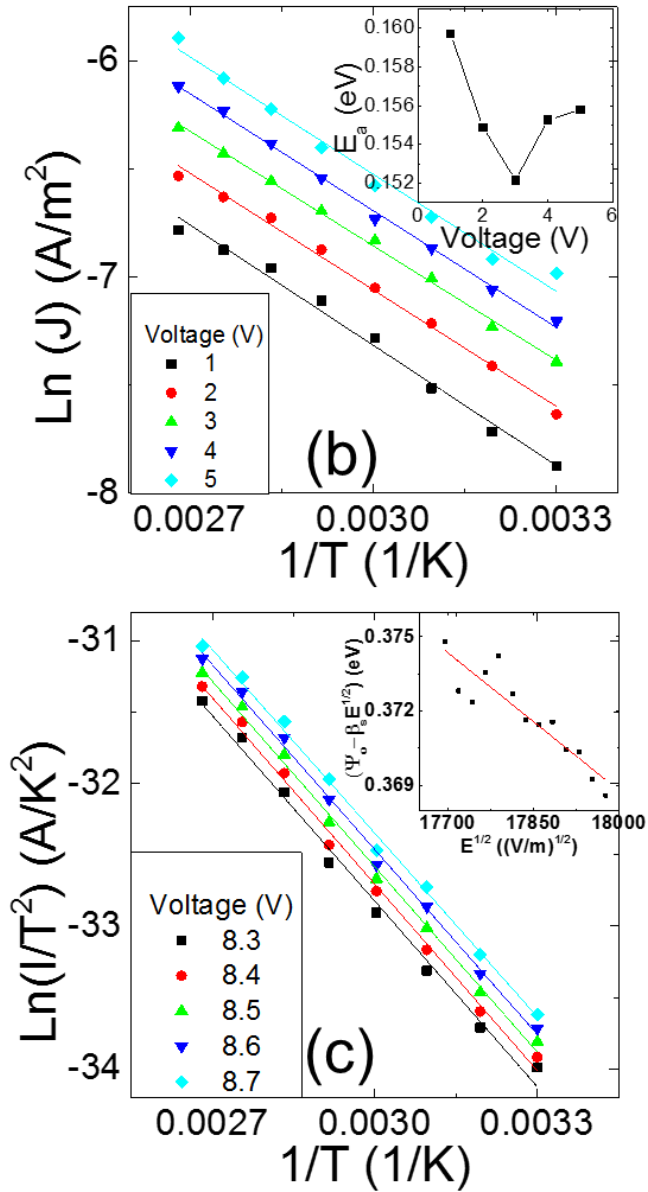


Figure 3. 8. (a) I-V curves and (b) Arrhenius form ($\text{Ln } J$ vs. $1/T$) plot under a negatively biased condition measured at different temperatures ranging from 30 to 100°C. (Inset figures of (b)) activation energies (E_a) extracted at each voltage from the best-linear-fitting of the data. (c) Schottky type form $\text{Ln}(I/T^2)$ vs. $1/T$ plot at voltages ranging from 8.3 to 8.7 V. (Inset figure of (c)) $\psi_0 - \beta_s E^{1/2}$ values plotted as a function of $E^{1/2}$

The above estimations unveil the switching mechanism in this material system. The identification of two trap levels (0.6 and 1.0 eV) in the positive bias region suggested that these levels should be taken into account for the identification of the switching mechanism, and the electrode-area-independent LRS resistance revealed that the conduction path with the 0.6 eV of trap depth were spatially localized. This localized area might be related with several locations along the grain boundaries of the crystallized HfO₂, whereas the current path with the trap depth of 1.0 eV could be safely assumed to be the bulk HfO₂ from the electrode-area-dependent HRS resistances. The trap depth of 1.0 eV well coincided with the energy distance between the V_o from the CB edge in HfO₂ [31]. Although the trap depth of 0.6 eV has not been reported in HfO₂ yet especially when the trap depth of V_o was ~1 eV, (It must be noted that estimation of trap depth or additional energy location in the band gap of dielectrics generally relies upon the adopted functional in density functional theory calculations, mainly due to the band gap underestimation. Therefore, only the theoretical reports assigning the trap depth of V_o to ~1 eV were considered in this work.) the high V_o density and the possible interactions between them at several specific structures of grain boundaries could induce the shift of V_o level upward. Otherwise, there could be any other defects which may form trap levels at that energy location. Another possibility for explaining the shallower trap levels could be that the energy gap of oxides near the grain boundaries are lower than the bulk [32], so that the identical traps could induce shallower trap depth in P-F conduction. In any case, it was

believed that the number of locations with such specific trap distribution must be quite limited, so that the electrode-area-independent LRS resistance could be achieved, while the electrode-area-dependent HRS resistance could be safely ascribed to the uniform (low) electrical conduction throughout the bulk portion of HfO₂.

Although the accurate energy band structure could not be depicted due to the lack of precise information on the band offset between the two dielectric layers and possible (small) Schottky barrier at the HfO₂/TiN interface, a tentative schematic band diagram could be drawn as shown in figure 3.9 (a) for the zero external bias condition. Here, the CB offset between Ta₂O₅ and HfO₂ was taken as 1 eV considering the known electron affinities of the two materials [33, 34], and contact potential at the HfO₂/TiN interface was arbitrarily taken as 0.3 eV to make it an (quasi-) Ohmic contact. The figure in left hand panel showed the circumstance for bulk portion of HfO₂, which does not bear the specific 0.6 eV traps, and right hand panel showed the circumstance for the local portion of HfO₂ which has the specific 0.6 eV traps in addition to the 1.0 eV traps. There must be internal bias voltage being ascribed to the different Schottky barrier heights of the two interfaces, and such internal bias must be applied over the two dielectric layers inversely proportional to their static dielectric constants. The electronic configuration of traps (trap-empty or trap-filled) could be dependent on the relative energy locations of the traps and Fermi levels of metals. However, when a small positive bias applied to the Pt TE, all the traps easily detrapped by the

transport of trapped electrons to Pt TE through CB of Ta₂O₅ layer. Due to the close proximity of trap levels in HfO₂ and CB of Ta₂O₅, and always higher level of CB of HfO₂ than that of Ta₂O₅, Ta₂O₅ layer generally did not interfere with the electron transport when the electrons were injected from TiN BE through HfO₂ layer. Of course, this is not the case for negative bias condition. The initially low current and the observation of the P-F conduction mechanism with a trap depth of 1 eV suggested that the two trap levels were with the trap-empty configurations under low positive bias condition, which well coincided with the HRS. With the slight increase in the positive bias voltage to Pt TE, electrons must be injected from TiN BE to HfO₂ mainly via the thermionic emission. No observation of any tunneling-related mechanisms suggested that tunneling of electrons to trap levels from the TiN BE and trap-assisted-tunneling mechanism could be safely disregarded in this case. This must be reasonable considering the rather thick thickness of the two layers, (20 nm) and that 10 V of applied voltage coincided with average 5MV/cm which was generally too low to induce a significant tunneling. Under the not-so-high positive bias voltage (< ~3 V), the injected electrons trapped mainly at the trap levels of 1.0 eV, and transported through the hopping mechanism, as schematically shown in figure 3.9 (b). This must be due to the low voltage which was insufficient to sufficiently decrease the trap depth by the P-F effect. It was believed that most of the traps remained empty since the degree of carrier injection must be low due to the low bias voltage. This explained the hopping mechanisms observed for both HRS and LRS shown in figures 3.6 (b)

and (c). As the voltage increased, the carrier injection became higher, and both traps started to be filled with the injected carriers. At the same time, the P-F effect started to work and the effective trap depth decreased as shown in figure 3.9 (c). It must be noted that this effect should work for both the 0.6 and 1.0 eV depth traps, but as long as the traps with 1.0 eV were not fully filled, the operation of the 0.6 eV depth traps could not be detected since the carriers had no reason to stay in the shallower levels rather than transited to the deeper traps. This could well explain the observation of HRS current in the higher positive voltage region. When the voltage became high enough and the carrier injection overwhelmed their transport through the HfO_2 (also via Ta_2O_5) layer, the deep traps were now fully filled with carriers, and the system switched to LRS, as long as the trapped carriers did not detrapp. Under this circumstance both deep and shallow traps could be filled with carriers, but the shallow traps could be detrapped temporarily under the positive bias condition due to the P-F effect, and the carrier transport could occur via the P-F mechanism mediated by the 0.6 eV traps. This could explain the observation of P-F mechanism current with 0.6 eV trap depth for the LRS.

Therefore, these mechanistic considerations suggested that the switching from the HRS to LRS under the positive bias condition corresponded to the filling of deep traps with the injected carriers, and further injected carriers transported via the local paths which contained the shallower traps. As mentioned above, these localized paths could be composed of some specific regions along the grain boundaries of HfO_2 but there was no reason why some

part of bulk HfO₂ could not contribute to this local paths especially under the process conditions that the plasma-induced damage was rather serious. Such a condition could be schematically represented by the figure shown in figure 3.9 (d). The switching back from the LRS to HRS and low current irrespective of the resistance state under the negative bias could be understood as follows.

When the bias voltage decreased to a sufficiently low negative bias, the electrons in the HfO₂ traps were detrapped while the electron injection from the Pt TE was suppressed by the high Schottky barrier height. Figure 3.9 (e) showed the schematic diagram of this circumstance. This coincided with the resetting graphs in figure 3.3 (d). Therefore, when the bias voltage was switched back to a positive direction, the drift of the electrons injected from the TiN were interfered with by the traps with a depth mainly of ~1.0 eV, so that the current flow under this circumstance must be much lower, and HRS could be attained. This is, in fact, identical to the current conduction of the pristine state, explaining the electroforming-free property of the present sample. The degradation in the retention performance at 85 °C for the case of HRS (decrease in the HRS resistance) could be also understood from the suggested switching mechanism. When the traps became empty by the high negative bias, and bias was removed subsequently, the energy band diagram could be represented by figure 3.9 (f). Under this circumstance, some of the electrons accumulated at the Ta₂O₅/HfO₂ layer, which were injected from the Pt electrode by thermionic emission, could be transported to the empty deep traps and degrade the HRS resistance with time (See figure 3.4 (d)).

The above mentioned switching mechanism also provided a reasonable explanation for the degraded switching performances of the thinner HfO₂ film shown in figure 3.3 (c). In this case, the total numbers of traps with both 1.0 and 0.6 eV trap depth in HfO₂ must be smaller, so that the switching performance was degraded.

The most critical feature of the above-mentioned switching mechanism is that it is related with the change in the charge state of the electron traps, presumably oxygen vacancies with different oxidation states in HfO₂, not the variations in their local spatial distribution or concentration, meaning that this is an almost purely electronic mechanism. This is closely related with the high uniformity of the memory cell. It could be noted that this type of RS mechanism had an aspect in common with the flash memory in that the electron movement for writing occurred only in one side of the devices; in the flash, electrons tunnel between the channel and the floating gate (or charge trap layer) via the tunneling oxide while their migration through the blocking oxide is strictly prohibited. In this ReRAM, during the writing operations, electrons are transported between the TiN electrode and the deep trap levels in the HfO₂ through the HfO₂ layer while their movement through the Ta₂O₅ layer is successfully suppressed by the high Schottky barrier. Of course, the reading mechanism must be quite different in the two devices.

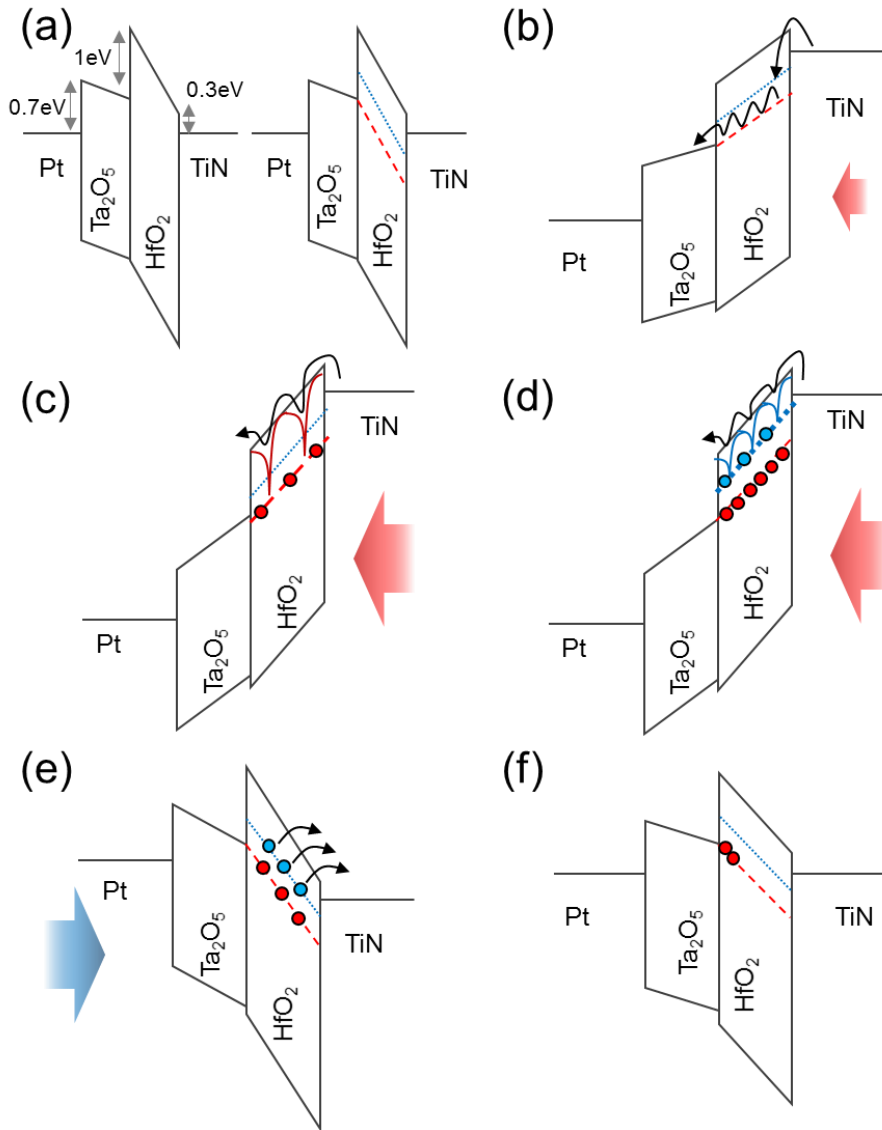


Figure 3. 9. Schematic diagram showing the switching mechanism: (a) Schematic diagrams of band structure for zero bias condition (left panel figure). The bulk of HfO_2 has the 1.0eV traps, which has coincided with the energy distance between V_o from the CB edge, while local portion of HfO_2 has the 0.6eV traps in addition to the 1.0eV traps (right panel figure). (b) Under the low positive bias ($\sim 3V$), the injected electrons transported through

the hopping mechanism. (c) As the traps with 1.0eV were filled with electrons, P-F effect started to show up where the effective trap depth decreased at the higher positive bias. (d) The carrier transport could occur via P-F mechanism mediated by 0.6eV traps after the deeper trap level was fully filled with carriers and the system switched to LRS. (e) When the low negative bias was applied to system, the electrons in the HfO₂ traps were detrapped. At the same time, carrier injection from the Pt electrode was suppressed by the Schottky barrier while the electrons from all the trap sites detrap switching back the sample to HRS. (f) Even under no bias condition, some of the electrons accumulated at the Ta₂O₅/HfO₂ interface could be transported to the empty deep traps and degrade the HRS with time especially at high temperature (85 °C)

3.5. Summary

In this work, a feasible method of achieving a highly uniform, electroforming-free, and self-rectifying RS memory cell is presented. The method can be generally stated as having a two-layered dielectric structure, where one layer (in this case, HfO₂) works as the resistance switching layer by trapping and detrapping the deep trap sites (1.0 eV trap depth) while the other dielectric layer (in this case, Ta₂O₅) remains intact during the whole switching cycle and creates a high Schottky barrier with a high-work-function metal (in

this case, Pt) to constitute the rectifying functionality. In addition, the RS layer should have a lower dielectric constant compared with the rectifying oxide layer for the effective application of the integral part of the voltage over the RS layer. In addition, the energy gap of the RS layer should be higher than that of the rectifying oxide layer to ensure that the carrier transport in the forward (or switching) bias polarity will not be disturbed by the conduction band offset between the two dielectric layers.

The present combination of the Ta₂O₅ and HfO₂ layers, which were in contact with the Pt and TiN electrode, respectively, nicely fitted the above-mentioned conditions for achieving the desired multitude of functionality from one RS system. In addition, the appropriate deoxidation effect of the PEALD process for Ta₂O₅ on the underlying HfO₂, while the deoxidation effect on Ta₂O₅ itself was minimized by the optimized process conditions, made the HfO₂ have just enough density of oxygen vacancies to induce the fluent RS within the layer. With all these optimized structure and operation conditions for the given structure, excellent RS uniformity and electroforming-free and self-rectifying functionality could be simultaneously achieved from the Pt/Ta₂O₅/HfO₂/TiN structure, which could be attributed to the electronic switching mechanism, where the disturbance by the uncontrolled ion migration could be largely suppressed.

3.6. Bibliography

- [1] J. Borghetti, G. S. Snider, P. J. Kuekes, J. J. Yang, D. R. Stewart, and R.S. Williams, *Nature* **2010**, 464, 873.
- [2] E. Linn, R. Rosezin, C. Kugeler, and R. Waser, *Nat. Mater.*, **2010**, 9, 403.
- [3] S. H. Jo, K. Kim and W. Lu, *Nano Letters*, **2009**, 9, 870-874.
- [4] G. H. Kim, J. H. Lee, Y. Ahn, W. Jeon, S. J. Song, J. Y. Seok, J. H. Yoon, K. J. Yoon, T. J. park, and C. S. Hwang, *Adv. Funct. Mater.*, **2012**, 23, 1440-1449.
- [5] M. J. Lee, C. B. Lee, D. Lee, S. R. Lee, M. Chang, J. H. Hur, Y. Kim, C. Kim, D. H. Seo, S. Seo, U. Chang, I. Yoo, and K. Kim, *Nat. Mater.*, **2011**, 10, 625-630.
- [6] J. Y. Seok, S. J. Song, J. H. Yoon, K. J. Yoon, T. H. Park, D. E. Kwon, H. Lim, G. H. Kim, D. S. Jeong, and C. S. Hwang, submitted to *Adv. Funct. Mater.*
- [7] D. Kwon, K. M. Kim, J. H. jang, J. M. Jeon, M. H. Lee, G. H. Kim, X. Li, G. Park, B. Lee, S. Han, M. Kim, and C. S. Hwang, *Nat. Nano.*, **2010**, 5, 148-153.
- [8] B. J. Choi, D. S. Jeong, S. K. Kim, C. Rohde, S. Choi, J. H. Oh, H. J. Kim, C. S. Hwang, K. Szot, R. Waser, B. Reichenberg, and S. Tiedke, *J. Appl. Phys.*, **2005**, 98, 033715.
- [9] G. Park, X. Li, D. Kim, R. Jung, M. Lee, and S. Seo, *Appl. Phys. Lett.*, **2007**, 91, 222103.
- [10] K. M. Kim, B. J. Choi, C. S. Hwang, *Nanotechnology*, **2011**, 22,

254002.

[11] K. M. Kim, B. J. Choi, C. S. Hwang, *Appl. Phys. Lett.*, **2007**, 90, 242906.

[12] S. J. Song, J. Y. Seok, J. H. Yoon, K. M. Kim, G. H. Kim, M. H. Lee and C. S. Hwang, *Scientific Reports*, **2013**, DOI: 10.1038/srep03443.

[13] N. Huby, G. Tallarida, M. Kutzaba, S. Ferrari, E. Guziewicz, L. Wachnicki, and M. Godlewski, *Microelectron. Eng.*, **2008**, 85, 2442-2444.

[14] G. H. Kim, J. H. Lee, J. H. Hwan, S. J. Song, J. Y. Seok, J. H. Yoon, K. J. Yoon, M. H. Lee, T. J. park, C. S. Hwang, *Appl. Phys. Lett.*, **2012**, 100, 213508.

[15] W. Y. Park, G. H. Kim, J. Y. Seok, K. M. Kim, S. J. Song, M. H. Lee, and C. S. Hwang, *Nanotechnology*, **2010**, 21, 195201.

[16] J. Huang, Y. Tseng, C. Hsu, and T. Hou, *IEEE Electron Device Letters*, **2011**, 32, 1427-1429.

[17] W. Lee, J. Park, S. Kim, J. Woo, J. Shin, G. Choi, S. Park, D. Lee, E. Cha, B. h. Lee, and H. Hwang, *ACS NANO*, **2012**, 6, 8166-8172.

[18] M. Son, J. Lee, J. Park, J. Shin, G. Choi, S. Jung, W. Lee, S. Kim, S. Park, and H. Hwang, *IEEE Electron Device Letters*, **2011**, 32, 1579-1581.

[19] G. D. Wilk, R. M. Wallace, J. M. Anthony, *J. Appl. Phys.* **2001**, 89, 5243.

[20] B. Govoreanu, G. S. Kar, Y. -Y. Chen, V. Paraschiv, S. Kubsek, A. Fantini, I. P. Radu, L. Goux, S. Clima, R. Degraeve, N. Jossart, O. Richard, T. Vandeweyer, K. Seo, P. Hendrix, G. Pourtois, H. Bender, L. Altimine, D. J.

- Wouters, J. A. Kittl, M. Jurczak, *IEDM Tech. Dig.* **2011**, 729.
- [21] P. Gonon, M. Mougenot, C. Vallee, C. Jorel, Jousseau, H. Grampeix, F. El Kamel, *J. Appl. Phys.* **2010**, *107*, 074507.
- [22] J. H. Hur, M. Lee, C. B. Lee, Y. Kim, and C Kim, *Phys. Rev. B*, **2010**, *82*. 155321.
- [23] C. Y. Dong, L. Shi, D. S. Shang, W. Chen, J. Wang, B. G. Shen and J. R. Sun, *J. Phys. D: Appl. Phys.*, **2011**, *44*, 205302.
- [24] K. M. Kim, B. J. Choi, M. H. Lee, G. H. Kim, S. J. Song, J. Y. Seok, J. H. Yoon, S. Han and C. S. Hwang, *Nanotechnology*, **2011**, *22*, 254010.
- [25] K. M. Kim, G. H. Kim, S. J. Song, J. Y. Seok, M. H. Lee, J. H. Yoon and C. S. Hwang, *Nanotechnology*, **2010**, *21*, 305203.
- [26] K. J. Yoon, S. J. Song, J. Y. Seok, J. H. Yoon, G. H. Kim, J. H. Lee and C. S. Hwang, *Nanotechnology*, **2013**, *24*, 145201.
- [27] S. F. Ho, S. Contarini, and J. W. Rabalais, *J. Phys. Chem.*, **1987**, *91*, 4779
- [28] J. Lim, B. Oh, W. Lee, K. Lee, H. Na, B. Kim, D. Seo, J. Han and J. Hwang, *Appl. Phys. Lett.*, **2009**, *95*, 123503.
- [29] B. Vincent Crist, *Handbook of Monochromatic XPS spectra*, John Wiley & Sons, England, **2000**.
- [30] P. Broqvist and A. Pasquarello, *Appl. Phys. Lett.*, **2006**, *89*, 262904.
- [31] J. L. Gavartin, D. Munoz Ramo, A. L. Shluger, G. Bersuker and B. H. Lee, *Appl. Phys. Lett.*, **2006**, *89*, 082908.
- [32] K. P. McKenna and A. L. Shluger, *Proc. R. Soc. A*, **2011**, *467*, 2043.

- [33] W. Zheng, K. H. Bowen, J. Li, I. Dabkowska, and M. Gutowski, *J. Phys. Chem. A*, **2005**, 109, 11521.
- [34] B. C. Lai, N. Kung and J. Y. Lee, *J. Appl. Phys.*, **1999**, 85, 4087.

4. Self-rectifying Resistive Switching Phenomena in Pt/Ta₂O₅/HfO₂/Ti structure

4.1. Introduction

Designing a new concept of RS memory cell and adopting new RS operation scheme which include the properties of self-rectifying RS behavior, electroforming-free and only electronic type RS behavior have been thought as impending tasks for the further application of planar or vertical type CBA devices. As a solution for this need, a new material system that includes highly uniformity in RS parameters, electroforming-free, and only electronic type RS behavior with self-rectification is presented in chapter 3 by combining two dielectric materials, HfO₂ and Ta₂O₅ which are contacted with Pt and TiN electrodes. Also, the functional films were grown by atomic layer deposition (ALD) and thus it is very friendly to the future vertical type CBA structure and further applications. In this structure, the main idea of unprecedented resistive switching phenomena is highly related to the role of each insulators and unique operation scheme. Fluent RS behavior which is induced without electroforming step is mainly originated from the initial defect which is formed during the plasma-enhanced ALD of Ta₂O₅ on top of HfO₂ in HfO₂ layer while the leakage current in the opposite bias region is highly suppressed through the high Schottky barrier formed at the interface

between high-work-function Pt and Ta₂O₅. Also, only electronic type RS mechanism without ionic movement inducing variations in the RS parameters dominated the overall RS operation which could be attributed to the trapping and de-trapping of electrons in traps of HfO₂ layer.

Even though previously reported self-rectifying RS device composed of Ta₂O₅ and HfO₂ has excellent properties and promising material system in the perspective of new RS memory structure concept, several problems which must be solved are clearly revealed. First, operation voltages especially set, reset and read voltage are too high to apply this structure ReRAM cell to actual storage memory. According to the reported results, enough and clearly distinguishable on/off and forward/reverse window could have been achieved only when the HfO₂ layer was thicker than ~10nm. Therefore, reducing the thickness in order to decrease operation voltage is not the appropriate method to solve the problem. Second, on/off and forward/reverse ratio should be improved. Taking into account the necessity of multi-level switching functionality and sneak path current problem which are crucial properties for storage memory, large enough on/off and forward/reverse resistance ratio should be proposed.

In this work, therefore, improved self-rectifying RS memory cells consisting of HfO₂ and Ta₂O₅ bi-layered structure with Pt (top) and Ti (bottom) electrodes as the configurations of crossbar structure which can provide excellent uniformity in the switching parameters and obtain electroforming-free, self-rectifying, self-limited current and multi-level switching

functionality are fabricated. Also, on/off and forward/reverse resistance ratio is drastically increased and operation voltage is reduced by about half compared to the previously reported value. According to the previous rigorous analysis results of conduction mechanism in bi-layered RS system, it has been found that the fluent RS behavior is mainly attributed to the HfO₂ layer which is connected to the bottom electrode (BE) while the Ta₂O₅ plays just the role of rectifying layer which is connected to top electrode (TE). The highly uniform and electroforming-free RS behavior are achieved by the defect state in the HfO₂ layer. Ti which is newly used as BE in this structure was chosen as a breakthrough point in order to solve the remaining critical problems in bi-layered RS system described above. Defect content in HfO₂ layer is highly increased during the ALD of the HfO₂ layer on Ti electrode due to deprivation of oxygen ions in HfO₂. Also, the relative small work-function value of Ti compared to the TiN has greatly influenced on the formation of stale (quasi-) ohmic contact between HfO₂ and Ti. Therefore, electron is more easily injected from bottom Ti electrode into HfO₂. Consequently, scaling down the operation voltage and increasing the current level of low resistance state which is the determinant of on/off and forward/reverse resistance ratio are obtained in much the same reason. So, in this self-rectifying I-V characteristics of these materials systems, the feasible and problem solved RS behavior is observed in one bias polarity while the current flow in the opposite bias polarity is highly suppressed.

4.2. Experiment

The standard photolithography and lift off process for top Pt and bottom Ti electrodes were used for the cross-bar type sample fabrication. Details for the crossbar pattern fabrication were reported elsewhere.[1] Using an 8-inch-diameter-scale traveling-wave-type ALD reactor (CN-1 Co. Plus 200), 10-nm-thick HfO₂ films were deposited on a 100-nm-thick Ti BE. Ti and Pt were deposited by e-beam evaporator (Maestech, ZZS550-2/D). ALD of the HfO₂ film was performed using Hf[N(CH₃)(C₂H₅)]₄ and O₃ as the Hf precursor and oxygen source, respectively. The PEALD Ta₂O₅ layer was deposited in another shower-head-type ALD reactor using tert-butylimido-bis(diethylamido)cyclopentadienyl)tantalum and H₂O-activated plasma (300 W) as the Ta precursor and oxygen source, respectively, at a substrate temperature of 200°C. The details for the ALD of HfO₂ and Ta₂O₅ were reported elsewhere.[2]

The film thickness, depth profile of each element, and chemical status of the films were examined using an ellipsometer (Gaertner Scientific Corporation, L116 D), AES (Perkin-Elmer, PHI 660), and XPS (ThermoVG, Sigma Probe), respectively. The cross-section of the Pt/Ta₂O₅/HfO₂/TiN sample was observed using a high-resolution TEM (FEI, Tecnai F20). For electrical measurement, Pt top electrodes were electron-evaporated through lift-off process for fabricating samples with different electrode areas (6,500-350,000 μm²) and cross-bar pattern. The self-rectifying resistive switching

behavior was measured using an HP4145B and HP4155A semiconductor parameter analyzer at room temperature, in voltage sweep mode. Each voltage sweep began from 0 V, and the bias was applied to the TE while the BE was grounded.

4.3. Structural Properties of the Ta₂O₅/HfO₂/Ti Thin-Film Stack

Figure 4.1a and b show the high resolution cross-section transmission electron microscopy (HRTEM) image and depth profiling in auger electron spectroscopy (AES) image of the Pt/Ta₂O₅/HfO₂/Ti structure. From the HRTEM image, each thin-film layers are well-distinguishable with the amorphous Ta₂O₅, crystallized HfO₂ and Ti except the HfO₂/Ti interface. An amorphous layer having around 5nm-thick is formed between monoclinic HfO₂ and crystallized Ti. It is evident that the deprivation of oxygen from HfO₂ to Ti during ADL process of HfO₂ on Ti can mainly influence on the formation of interfacial amorphous layer. This interfacial amorphous material is a critical factor that clarify the distinction of RS behavior of Pt/Ta₂O₅/HfO₂/Ti compared to Pt/Ta₂O₅/HfO₂/TiN structure. The details of RS behavior is dealt with the electrical performance part in this study. The well-distinguishable structure is also verified by AES data in figure 4.1b. The structural and chemical impact of depositing HfO₂ layer on Ti substrate and Ta₂O₅ layer on HfO₂ layer in Pt/Ta₂O₅/HfO₂/Ti is obviously confirmed by the

depth profiling in X-ray photoelectron spectroscopy (XPS) and medium energy ion scattering spectrometer (MEIS) shown in **figure 4.2**. Figure 4.2a ~ d show the Hf *4f* / Ta *4f* , only Hf *4f* , Ti *2p* and O *1s* core levels in the XPS depth profile data of the Ta₂O₅(10nm)/HfO₂(10nm)/Ti structure sample. Ar⁺ ion beam energy was fixed to 1keV during the etching to avoid the sputtering damage or unsuspected oxidation issue. The interval time of each etching level is ~10s. The core levels were represented with reference to the etch level. The value of binding energy (BE) of Ta *4f* shown in figure 4.2a well coincided with the reported BE value of the Ta *4f* in Ta₂O₅. (26.2 eV for Ta *4f*_{7/2} and 28.1 eV for Ta *4f*_{5/2}, expressed by the black vertical dashed lines in figure 4.2a).[3-4] The un-wanted by-product of oxygen deficient Ta *4f* and Hf *4f* BE peaks formed during the etching of oxygen atoms by the Ar⁺ ion appears near the BE of ~22-24 and ~14-15 eV, respectively. This emergence of by-product peaks is not the evidence that explain the influence of underlying HfO₂ and Ti layer on the chemical properties of the Ta₂O₅ and HfO₂ layer. Unlike in the case of Ta, an important two changes in BE of Hf *4f* were obvious from the Ta₂O₅/HfO₂ and HfO₂/Ti interface region. The BE of Hf *4f* core levels near Ta₂O₅ layer is shifted to a lower binding energy direction shown in figure 4.2b (indicated by the red vertical dashed lines). This results suggest that oxygen deficient HfO_{2-x} layer is formed near the Ta₂O₅ layer during the deposition of Ta₂O₅ on HfO₂ layer. The impingement effect of plasma and de-oxidation effect during deposition of Ta₂O₅ leads the formation of defects in HfO₂. The detailed explanation about the shift of BEs of Hf *4f* near the Ta₂O₅ layer is

reported in previous study.[2] It is worth noting that more important change of BE of Hf $4f$ is observed near the Ti substrate region. The BE of Hf $4f$ near the Ti substrate slightly shifted into the low BE direction. Considering the formation of amorphous layer between HfO₂ and Ti shown in figure 4.1a, this slight change of Hf $4f$ core levels is evidently understood. This result is corresponded to the depth profiling atomic concentration data of HfO₂/Ti and HfO₂/TiN measured by MEIS shown in figure 4.3a and b. These two structure sample were fabricated through HfO₂ ALD process with same conditions and cycles on each substrates. There are two notable points are observed. First, the measured thickness of HfO₂ layer of HfO₂/Ti structure is somewhat thinner than that of HfO₂/TiN. Second, oxidized Ti region painted by green color with a certain degree of thickness is formed only in HfO₂/Ti structure. Since Ti is a very large reactive metal, while the HfO₂ is deposited on Ti, HfO₂ was deprived of oxygen ions and some amount of TiO_x layer is formed between HfO₂ and Ti. Therefore, some amount of oxygen deficient HfO_x layer which could be found as a result of slight shift of Hf $4f$ core levels near Ti shown in figure 4.2b are subsequently formed. Considering to the HRTEM image of this structure, amorphous interlayer formed between HfO₂ and Ti could be designated as TiO_x layer. Also, the result that chemical properties of HfO_{2-x} layer highly depends on the underlying substrate materials especially in this case Ti and TiN could be found through the secondary ion mass spectrometry (SIMS) data shown in figure 4.4. Although previous studies on the self-rectifying RS phenomena in Ta₂O₅/HfO₂/TiN structure is clearly interpreted

by the de-oxidation effect itself while depositing the PEALD Ta₂O₅ layer on top of ALD HfO₂. [2] In Pt/Ta₂O₅/HfO₂/Ti sample, formation of oxygen deficient HfO_x layer due to deprivation of oxygen ions into Ti is also a critical factor that affect the electrical performances of this device. Interlayer formed between HfO₂ and Ti can barely influence on electrical properties of the Pt/Ta₂O₅/HfO₂/Ti structure sample since it is highly oxygen deficient TiO_x phase and (quasi-) ohmic contact is formed at TiO_x/Ti interface.

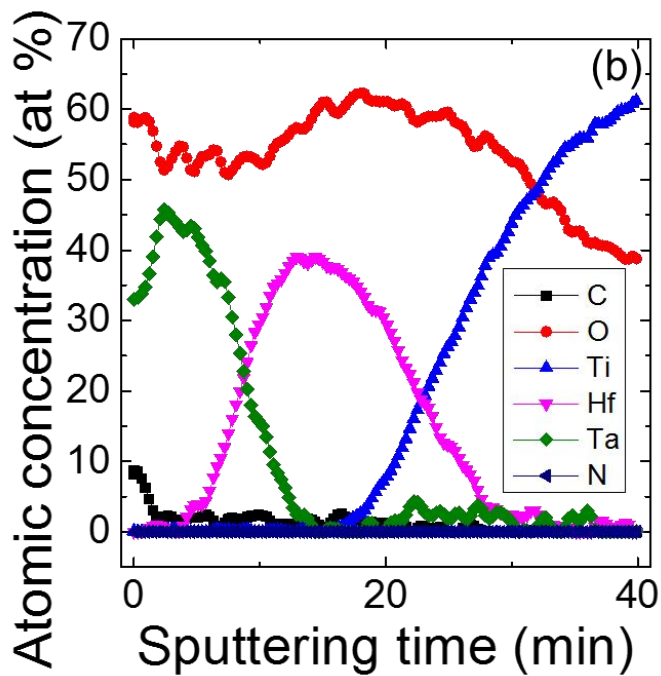
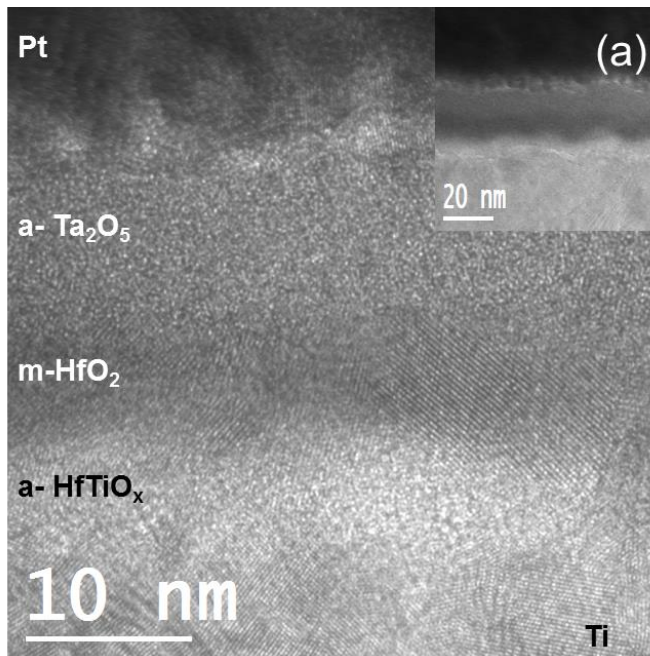
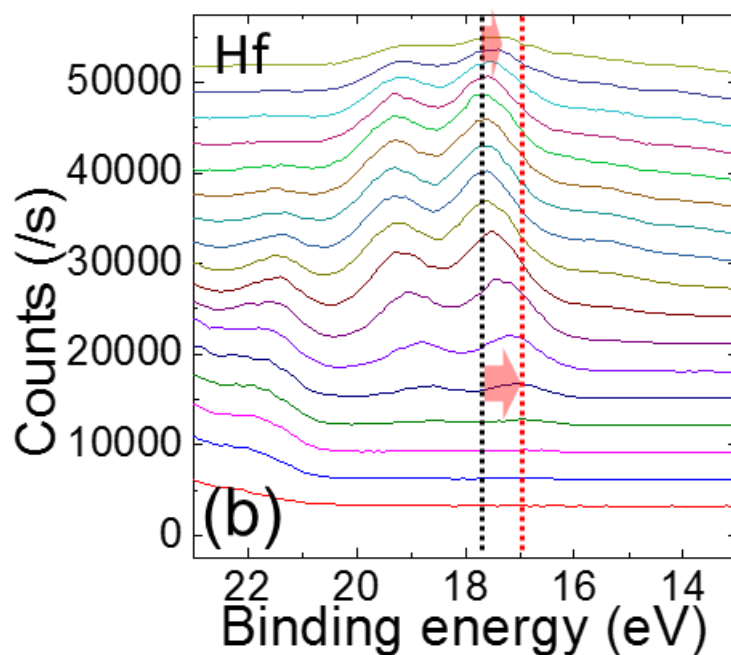
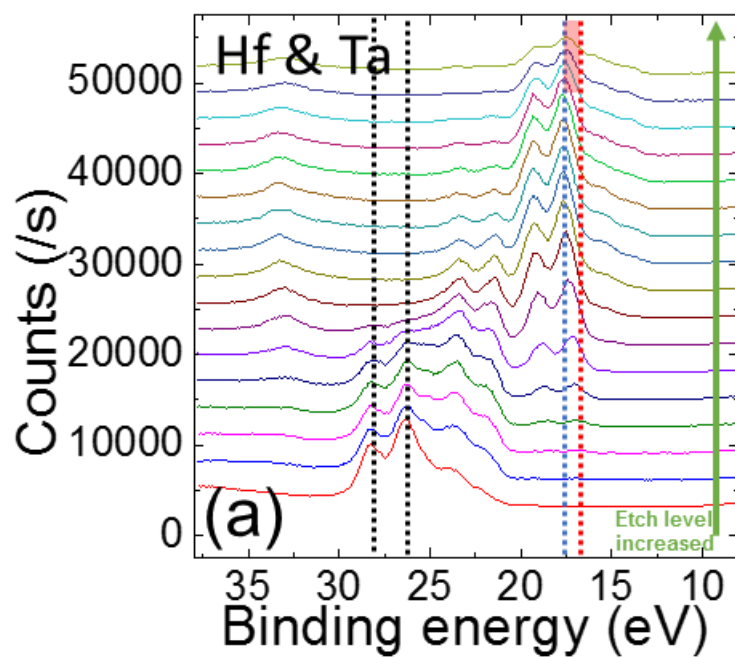


Figure 4. 1. (a) Cross-section TEM images and (b) depth profiling AES data of the Pt/Ta₂O₅(10nm)/HfO₂(10nm)/Ti sample



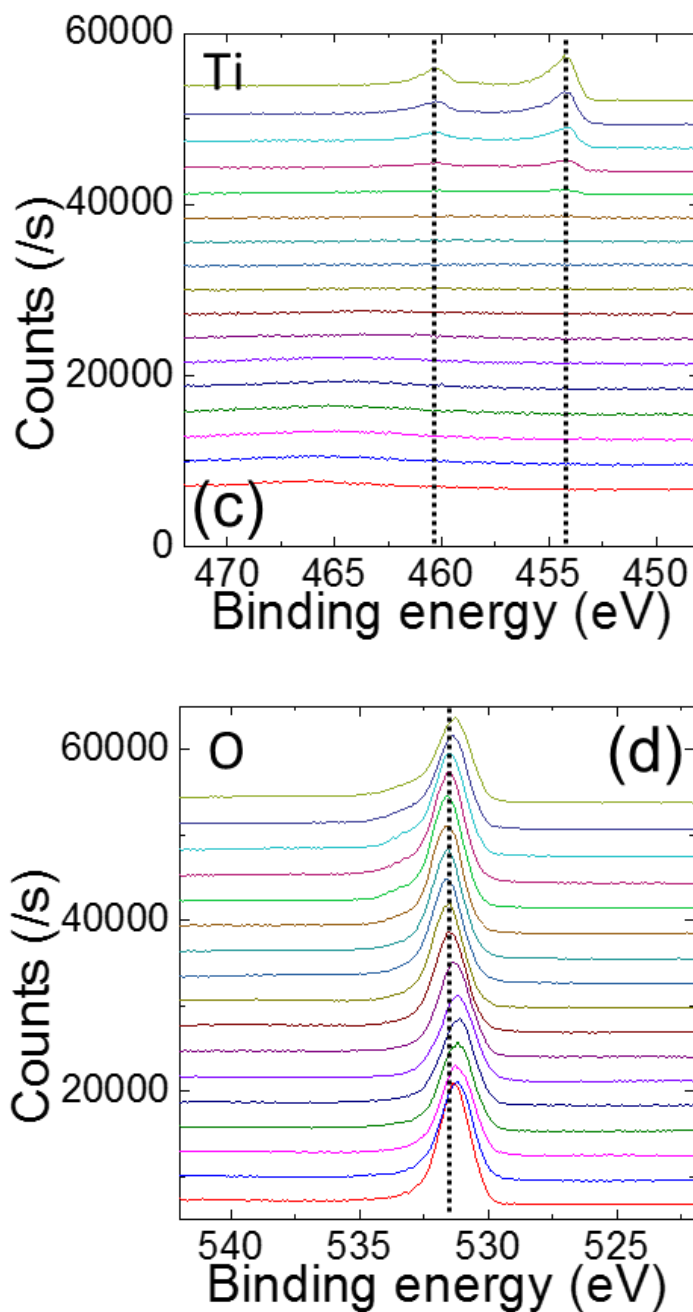


Figure 4. 2. (a) Ta 4*f*/ Hf 4*f*, (b) O 1*s*, (c) N 1*s* and (d) Ti 2*p* core levels in the XPS depth profile results of the Ta₂O₅(10nm)/HfO₂(10nm)/Ti sample

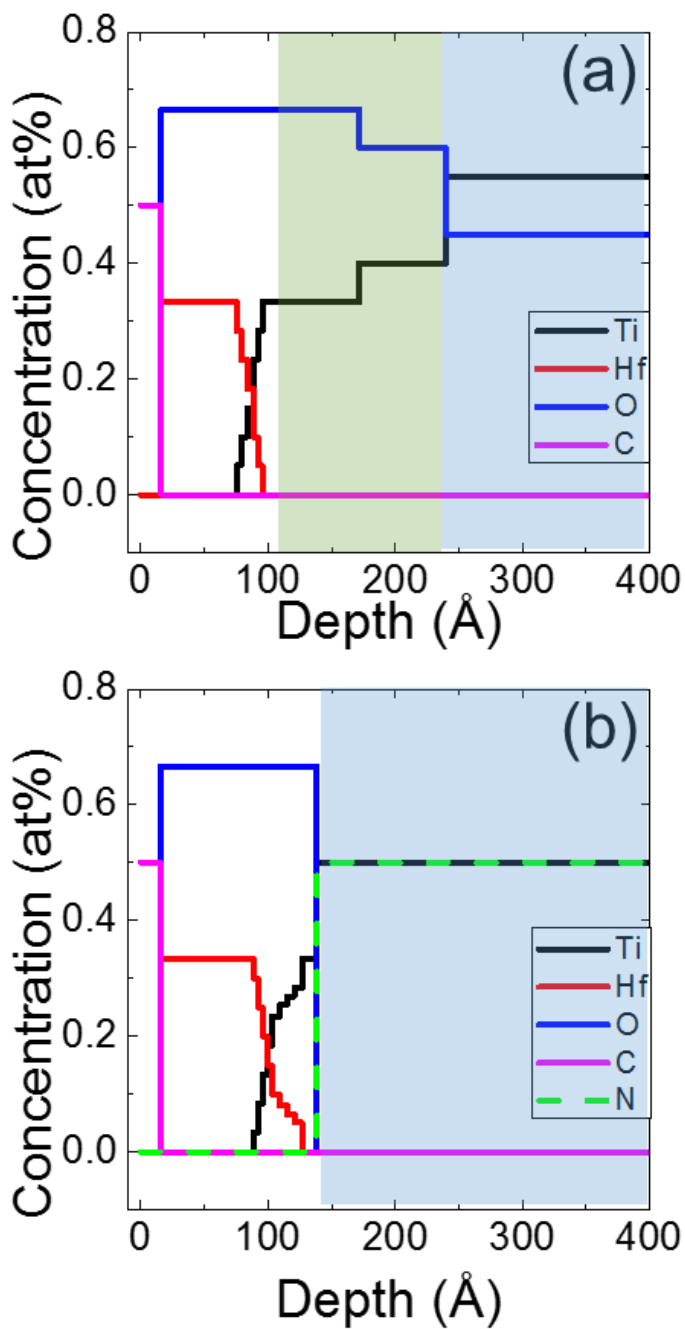


Figure 4. 3. Depth profiling atomic concentration data of (a) HfO₂/Ti and (b) HfO₂/TiN measured by MEIS

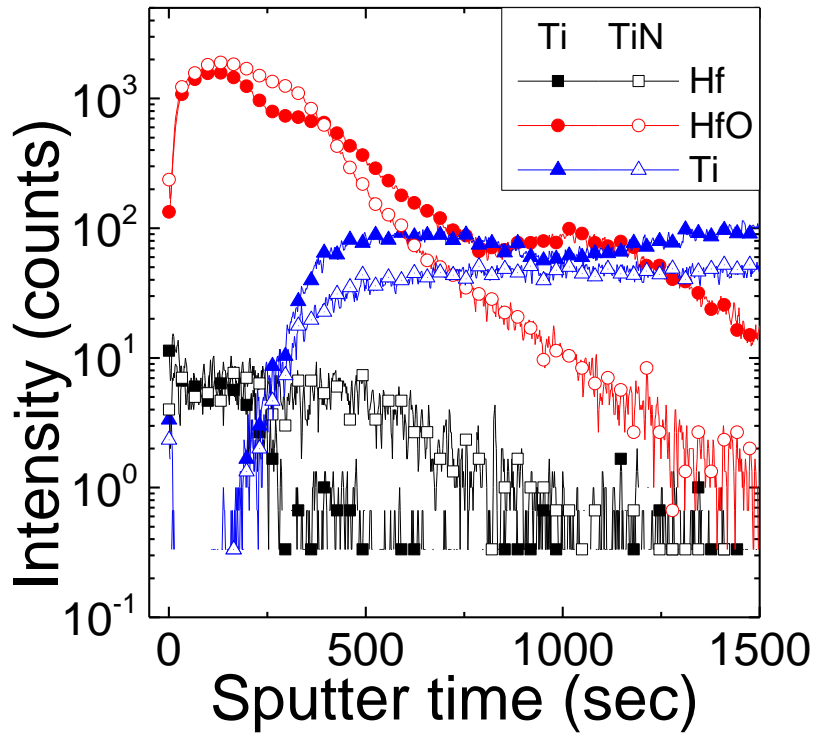


Figure 4. 4. SIMS data of HfO₂/Ti and HfO₂/TiN

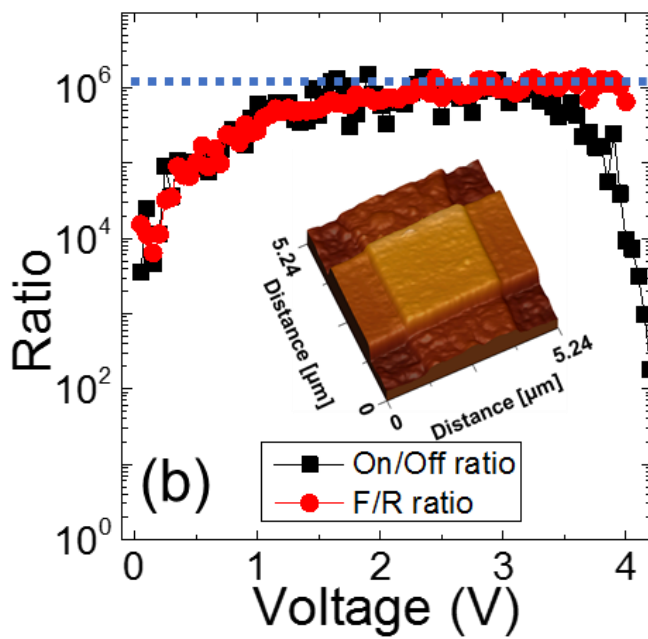
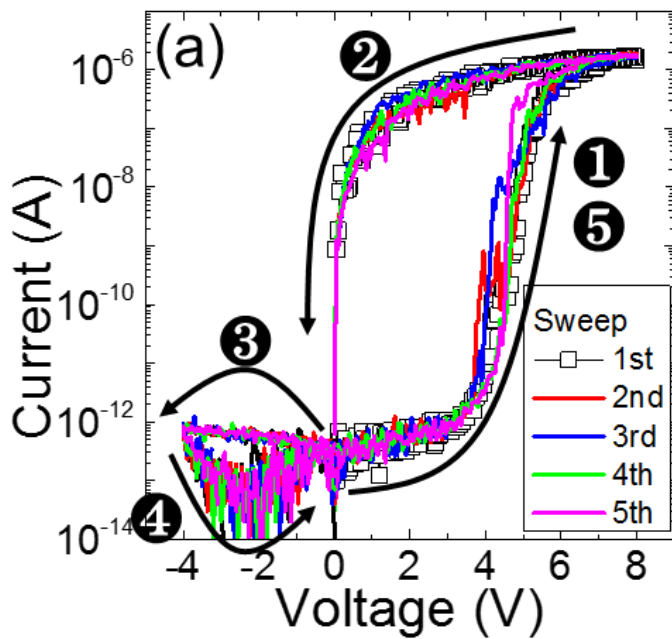
4.4. Electrical Performance of the Memory Cell

Figures 4.5a and b show the self-rectifying RS I-V curves and forward/reverse, on/off ratio of the Pt/Ta₂O₅/HfO₂/Ti. For these I-V measurements, Pt TE was biased while Ti BE was grounded. Most of the experimental data including RS behavior and parameters was obtained in 4 x 4 μm² cross-bar type cell shown in inset figure of figure 4.5b except for the result of area dependency. In this study, in order to avoid conventional operation sequence, different method that induce self-rectifying RS in Pt/Ta₂O₅/HfO₂/Ti is adopted. The general switching operation schemes are indicated by the numbers included in Figure 4.5a: the I-V curves of the pristine state (curve 1, open square symbol); the LRS (curve 2), which was induced by the first voltage sweep up to +8 V with no I_{cc}; the resetting curve (curve 3), where the voltage was swept down to -4 V; the HRS (curve 4), which was induced by the previous voltage sweep into the negative voltage direction; and the setting curve (curve 5) in the positive voltage region, which set the sample to the LRS again. The almost identical shapes of curves 1 and 5 reveal that this was the electroforming-free sample. This sample shows an asymmetric I-V shape. Considering the intrinsic property of Pt, Ta₂O₅, HfO₂, Ti and its band structure, it is clearly understood that the electron injection at the HfO₂/Ti is much more fluent under positive bias than at the Pt/HfO₂ interface under the negative bias. Two-layered dielectric structure shows feasible RS behavior. Although RS behavior in the positive region is clearly

shown while repeated switching cycles, leakage current is suppressed in the wide voltage range of negative voltage region. The detailed explanation about these asymmetric I-V and RS system is dealt with conduction mechanism analysis part. There are additional three notable points could be found in figure 4.5. First, highly improved on/off and forward/reverse resistance ratio between HRS and LRS could have been achieved (figure 4.5b) contrary to the previous result.[2] A maximum on/off resistance ratio and forward/reverse resistance ratio $\sim 10^6$ were achieved. These two most important factor that must be satisfied for the actual application of storage memory is competitive value as compared to the previous other results. Second, self-limited (-compliance) current curve is shown after sudden current jump while positive bias is induced in HRS. Actually, in order to switch the device from HRS into LRS, the magnitude of set voltage is enough with the value of around +6-7V. However, in figure 4.5a, the voltage is induced up to +8V while set operation to show the clear self-limited current behavior. It can be immediately understood that the Ta₂O₅ layer on the HfO₂ dominate the current conduction of LRS. Briefly, Ta₂O₅ acts as an external resistor that has been used in many other studies in terms of self-compliance RS behavior.[5] Also, it prevents the permanent breakdown of HfO₂ layer during the set operation. Third, operation voltage including electro-forming, set, reset and suitable read voltage is drastically decreased compared to the Pt/Ta₂O₅/HfO₂/TiN device. The voltage range for achieving self-rectifying RS operation in Ta₂O₅/HfO₂ structure with Pt and TiN as top and bottom electrode was too high and this is the major

problem that must be solved. Selecting the Ti material as BE is a key factor to solve the high operation voltage problem and increase on/off and forward/reverse resistance ratio. While HfO₂ layer is deposited on the Ti BE, Oxygen ions were migrated into the Ti electrode and thus content of defect state in HfO₂ layer is increased and this is the most crucial element that elucidate the RS phenomena in this device. The formation of amorphous layer and MEIS data shown in figure 4.1a, 4.3a and b clearly supports this deduction. Also, the fact that more stable (-quasi) ohmic contact is formed when HfO₂ layer is deposited on Ti rather than TiN is verified through the I – V curve of Pt/HfO₂/Ti and Pt/HfO₂/TiN shown in figure 4.6. Since electron is easily moved from BE to HfO₂ layer in HfO₂/Ti, higher current level of LRS and decreased operation voltages are simultaneously obtained. Figure 4.5c represents the exceptionally high uniformity of variation of current values in HRS and LRS at forward and reverse region. The cumulative probability of the current levels in LRS and HRS read at 2V shows extremely narrow distribution, suggesting the exceptional uniformity of each resistance states. Figure 4.5d shows the retention data of the LRS and HRS (measured at 2.5V) at 125, 150, 175 and 200°C up to > 10⁴ s. Since the degradation of current level in HRS and LRS at room temperature is not observed up to 10⁶ s as shown in figure 4.7, acceleration retention test with higher temperature was conducted. HRS and LRS maintained their current values even at the temperature as high as 200°C and 125°C up to 10⁴s, respectively. However, the degradation of current value in LRS is shown after 13000s at 125°C. The

degradation in the current values of LRS with time comes from the detrapping of the trapped electrons, which could be thermally activated process. In order to guarantee the retention time at room temperature, acceleration test was performed at higher temperature up to 200°C. The time when the current values was abruptly degraded is designated as retention time (detrapping time) and the plot of these retention time vs. $1/kT$ in the form of Arrhenius form is described in inset figure of figure 4.5d. The extracted activation energy for the detrapping as ~ 0.7 eV is almost exactly consistent with the extracted trap depth of Poole-Frenkel conduction in HRS which is investigated in switching mechanism analysis part. The intersection data point of extrapolation of the best-linear-fitting graph (red dashed line) of Arrhenius form plot and the vertical purple dashed line having value $\sim 38.94\text{eV}^{-1}$ ($1/kT$ values at room temperature) indicated that the retention time at the room temperature was $\sim 1.13 \times 10^7$ s. This is \sim one orders of magnitude lower than the 10-year-retention (3.2×10^8 s). Therefore, the study of further structure and process optimization should be conducted to improve retention property.



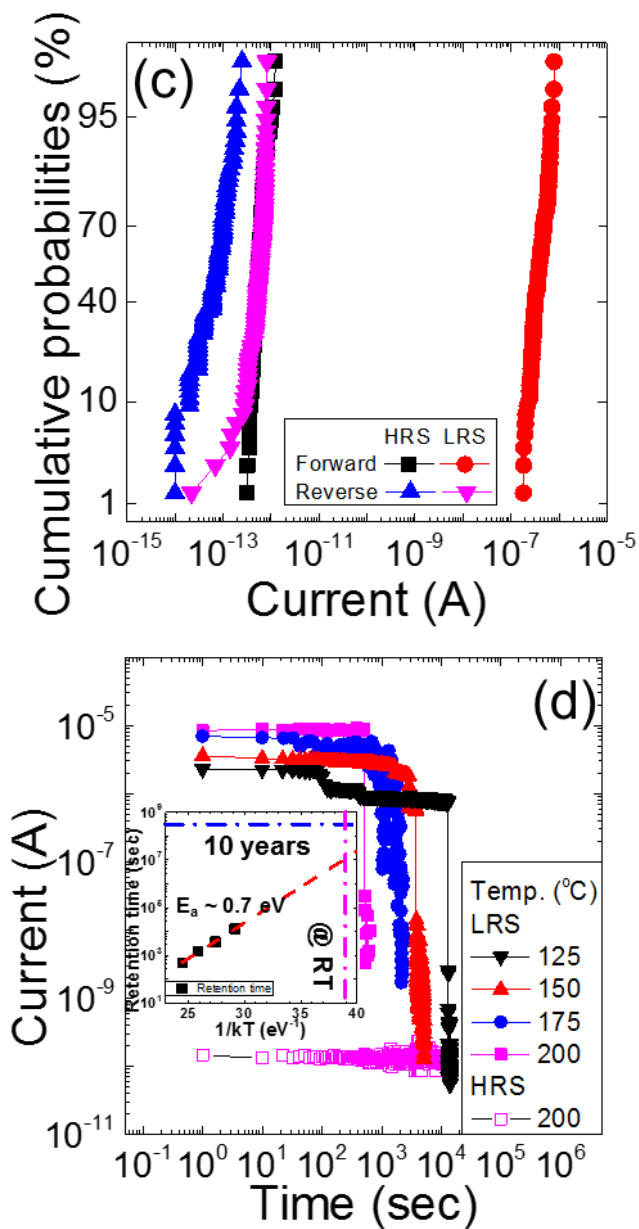


Figure 4. 5. (a) Resistive switching I-V curves, (b) on/off and F/R ratio, (c) cumulative probabilities at LRS and HRS and (d) retention properties of the Pt/10-nm-thick Ta₂O₅/10-nm-thick HfO₂/TiN structure. (Inset figure of figure (b)) AFM image of CBA type sample and (inset figure of figure (d)) retention time vs. 1/kT graph.

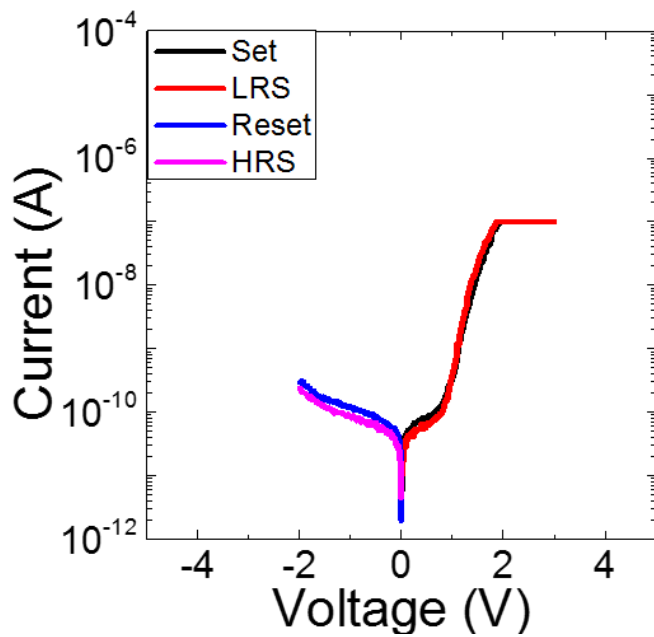
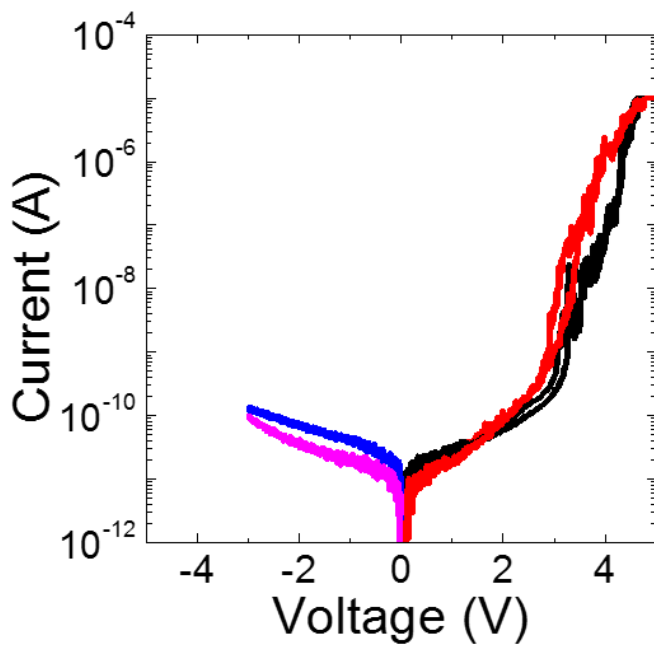


Figure 4. 6. I - V curves of (a) HfO₂/TiN and (b) HfO₂/Ti

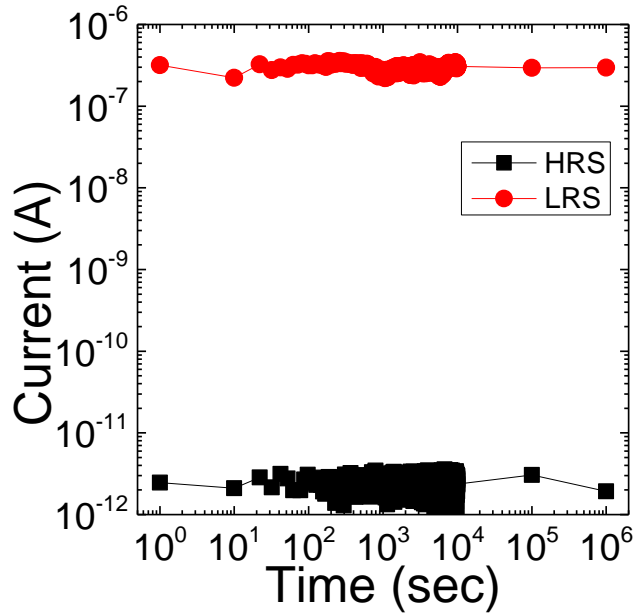


Figure 4. 7. Retention data at RT of Pt/Ta₂O₅/HfO₂/Ti structure sample

The conventional bipolar RS behavior could be derived in this sample even just changing the operation sequence. In figure 4.8, usual bipolar RS with self-compliance phenomena is shown. Electroforming process (not shown) is absolutely necessary, of course, in the negative bias voltage region with the typical electroforming voltage and the current levels of over $\sim -10V$ and $1\mu A$ to lead feasible RS curve contrary to the above self-rectifying RS case. This conventional bipolar RS is originated from the drifting movement of oxygen ions or oxygen vacancies at the active barrier (like schottky barrier). In this case, Pt/Ta₂O₅ interface act as an active barrier and thus oxygen ions or

vacancies modify the barrier height while the HfO_2/Ti interface having (quasi-) ohmic contact. Even though the electroforming process elicits the conventional bipolar RS, HfO_2 layer is expected to remain intact while repeated switching sequences. Self-compliance behavior is the clue that HfO_2 acts as the external resistor in conventional bipolar RS operation.

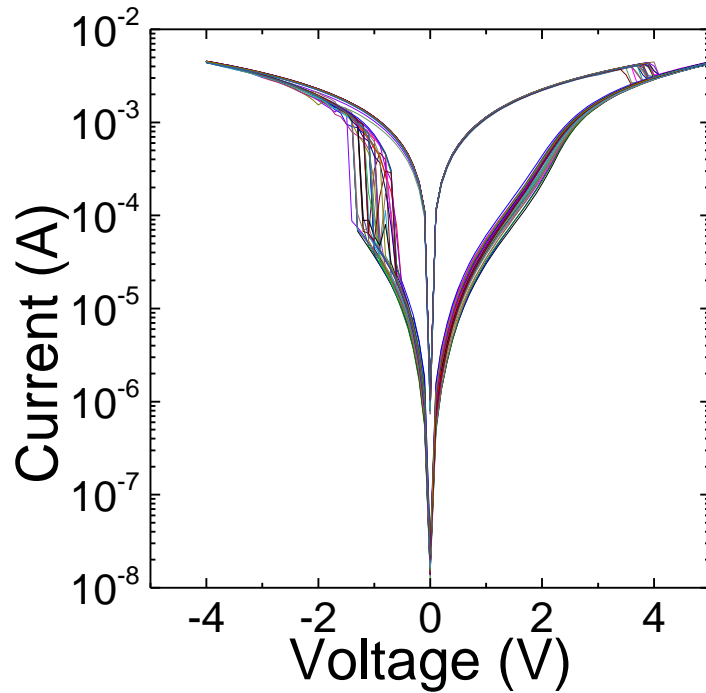


Figure 4. 8. Conventional bipolar RS I – V graph of Pt/Ta₂O₅/HfO₂/Ti structure sample

Multi-level switching functionality is another crucial property that should be necessary for the feasible storage memory device and further in order to replace the currently commercially used storage memory. For this purpose, the experiment on the possibility of multi-level switching characteristics in this Pt/Ta₂O₅/HfO₂/Ti device was carried out. Figure 4.9a shows the distribution of current values at read voltage 2V in several intermediate LRS that is originated from the different compliance current value while set operation. The mean value and variance of current levels at each states are obtained through a switching time of around 20. I – V curves of several intermediate LRS are shown in figure 4.9b. The current levels at each intermediate LRS is increased as the compliance current is increased from 100pA up to 10μA. When compliance current value exceed ~10μA, current level is saturated because of self-limited (-compliance) behavior in this self-rectifying RS device. Since variations of current level in each intermediate LRS itself while repeated switching are quite smaller than the difference of close two states that are only a 1 order difference of compliance current, these states could be considered as discrete states. Multi-level functionality in this device can easily be obtained simply by adjusting the compliance current while set operation. The area dependency of resistance in HRS and LRS is shown in the figure 4.9c. Unfortunately, fabricated cross-bar type sample having area size 4 ~ 100μm² has too low resistance value in HRS to measure the current value at read voltage 2V and thus this tendency of resistance value in HRS is reminiscent of non-area dependency. In order to

prevent misinterpretation, additional measurement of area dependency in HRS and LRS is carried out in a larger area $> 6000 \mu\text{m}^2$. It is worth noting that the current level of HRS completely depends on the area, suggesting that the HRS leakage current flowed uniformly along a whole area. On the other hand, LRS current clearly did not depend on the area, leading that limited local area formed during set operation is the only path that LRS current is flowed. An interesting finding is that when the intermediate state originated from different compliance current in set process also shows the area independency shown in inset figure of figure 4.9b. Once the deep traps in HfO_2 layer is trapped with the electron while set process, LRS current flows only the localized path. As area size is more scaled down, it lowers the current level in HRS but current level in LRS is maintained. Area dependency in HRS and LRS is one of the strong points of this device applying to the CBA or 3D vertical type integrated device having $\sim\text{nm}$ scale. In the following, the possible reasons for such exceptional performance are discussed, based on the electrical-conduction mechanisms of the HRS and LRS.

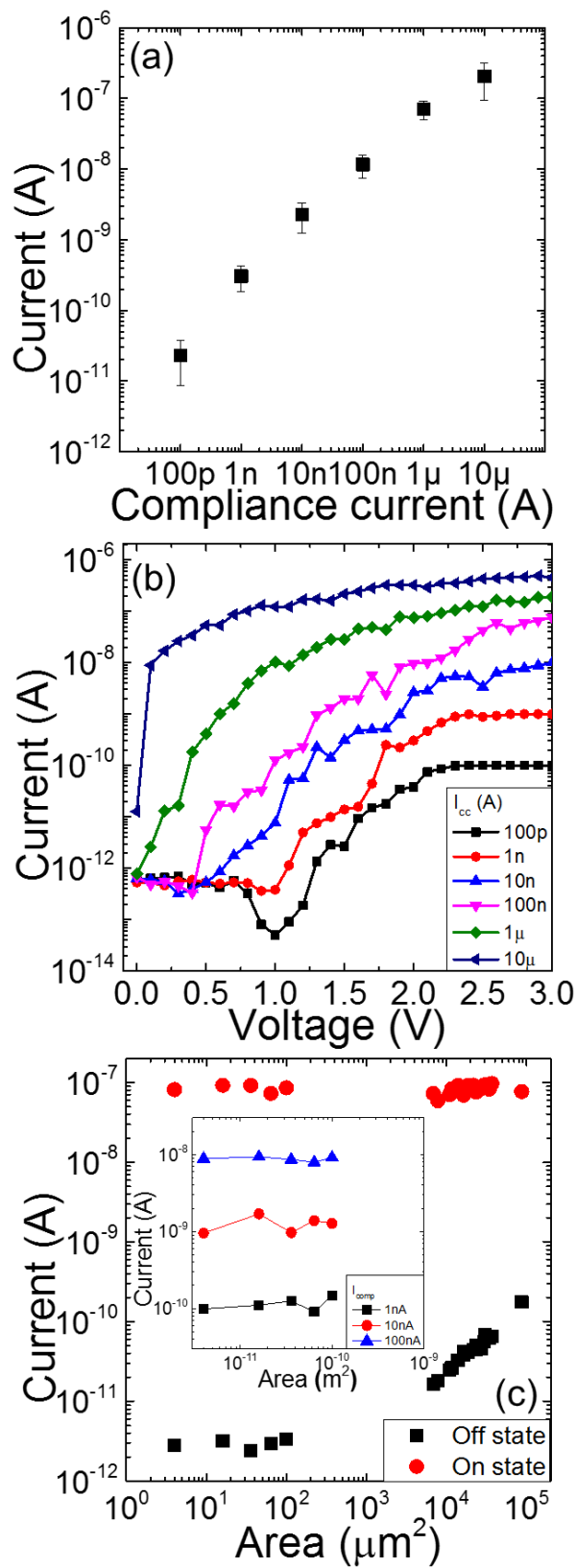


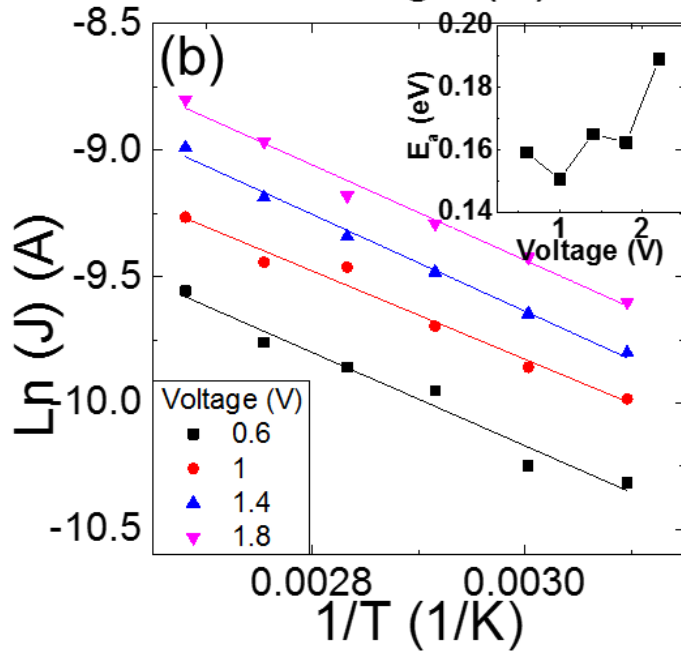
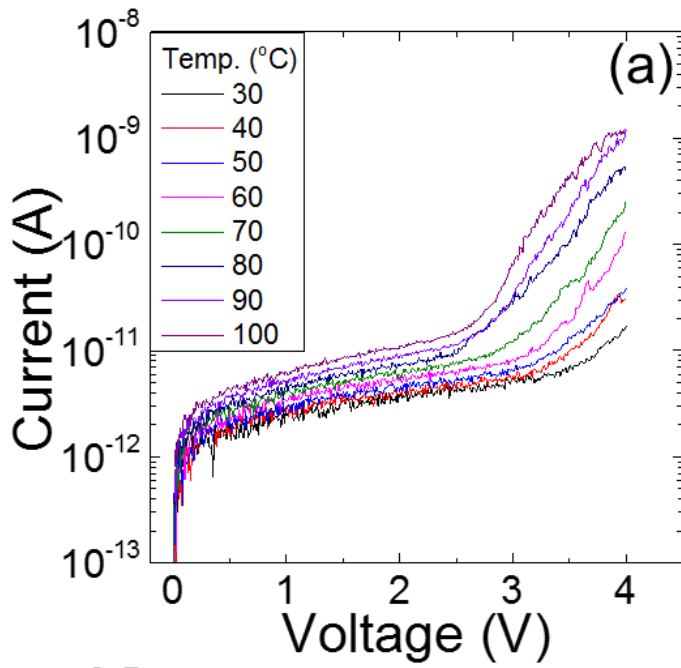
Figure 4. 9. (a) The mean value and distribution of current level at read voltage 2V in several intermediate LRS and (b) I – V curves at each intermediate LRS. Area dependency of (c) HRS and LRS and (inset figure of (c)) intermediate LRS

4.5. Switching Mechanism of the Memory Cell

Figure 4.10a shows the I-V curves of the HRS measured at different temperatures ranging from 30 to 100°C. The HRS is obtained from reset process with -4 V. It is evident that thermally activated mechanisms could elucidate the current conduction mechanism in HRS. The current level increased when the temperature is increased in the whole range. Furthermore, considering the increase rate of current, voltage region should be separated by two regions to interpret the current conduction mechanism easier. In order to make it easier to understand, voltage region < 3V and >3V are designated low-voltage-region and high-voltage-region, respectively. In low-voltage-region, the current gradually increased with the voltage and temperature. **Figure 4.10b** shows the Ln J vs. 1/T (Arrhenius plot) results at 0.6-1.8 V and the inset figure of figure 4.10b shows the extracted activation energies (E_a) at each voltage from the best-linear-fit graphs of the data. The activation energy obtained from Arrhenius form plot are relatively small values (~0.16eV). Also, not shown here, the slope of Ln I vs. Ln V graph, where the voltage is the

value applied to the HfO₂ layer, which is calculated from the series two capacitors model, is close to the value ~ 1 . These results suggest that the low-voltage-region follows the hopping conduction mechanism via trap sites of HfO₂ layer originated from the dispersed V_o. As the electron affinity of Ta₂O₅ is larger than HfO₂ ($\sim 3.2\text{eV}$ and $\sim 2.14\text{eV}$ in HfO₂ and Ta₂O₅, respectively) and band gap of Ta₂O₅ is smaller than that of HfO₂ ($\sim 4.2\text{eV}$ and $\sim 5.68\text{eV}$ in Ta₂O₅ and HfO₂, respectively) which are measured by Auger-electron spectroscopy reflective electron energy loss spectroscopy and spectroscopic ellipsometry, respectively, Ta₂O₅ layer cannot hinder the transportation of electrons and thus easily moved to Pt TE via the conduction band of the Ta₂O₅. In high-voltage-region, on the other hand, the current flow is dominated by Poole-Frenkel (P-F) conduction behavior. For the rigorous verification of conduction behavior in high-voltage-region other thermally activated conduction fitting was attempted to be fit with (not shown here) but did not fit well with the result except P-F conduction fitting. The parallel curves with the same slope at high-electric field-region of the $\text{Ln}(J/E)$ vs. $E^{1/2}$ plot shown in **Figure 4.10c** suggest that P-F conduction is well fit with the result. Inset figure of figure 4.10c shows the optical dielectric constant values extracted from the slope of $\text{Ln}(J/E)$ vs. $E^{1/2}$ plot at each temperature. The estimated values of 3.5-4.5 coincided well with the reported optical dielectric constant of ~ 3.9 calculated from the square of the refractive index ($n \sim 1.9$) of HfO₂. $\text{Ln}(J/(E \cdot T^{3/2}))$ vs. $1/T$ according to the P-F equation for the voltage ranging from 3.5-3.8 V are shown in **Figure 4.10d**. The extracted activation energy,

which is trap depth of HfO_2 layer, from the slope of best-linear-fitted graphs at each voltage could be achieved and described in inset figure of figure 4.10d. The energy level of trap depth in HfO_2 layer is $\sim 0.75\text{eV}$. Here, the trap depth of $\sim 0.75\text{ eV}$ well coincided with the energy distance between the V_o from the CB edge of HfO_2 . [6] Defects of HfO_2 layer which could be V_o formed during PEALD process of Ta_2O_5 and ALD of HfO_2 on Ti works as electron traps in HRS.



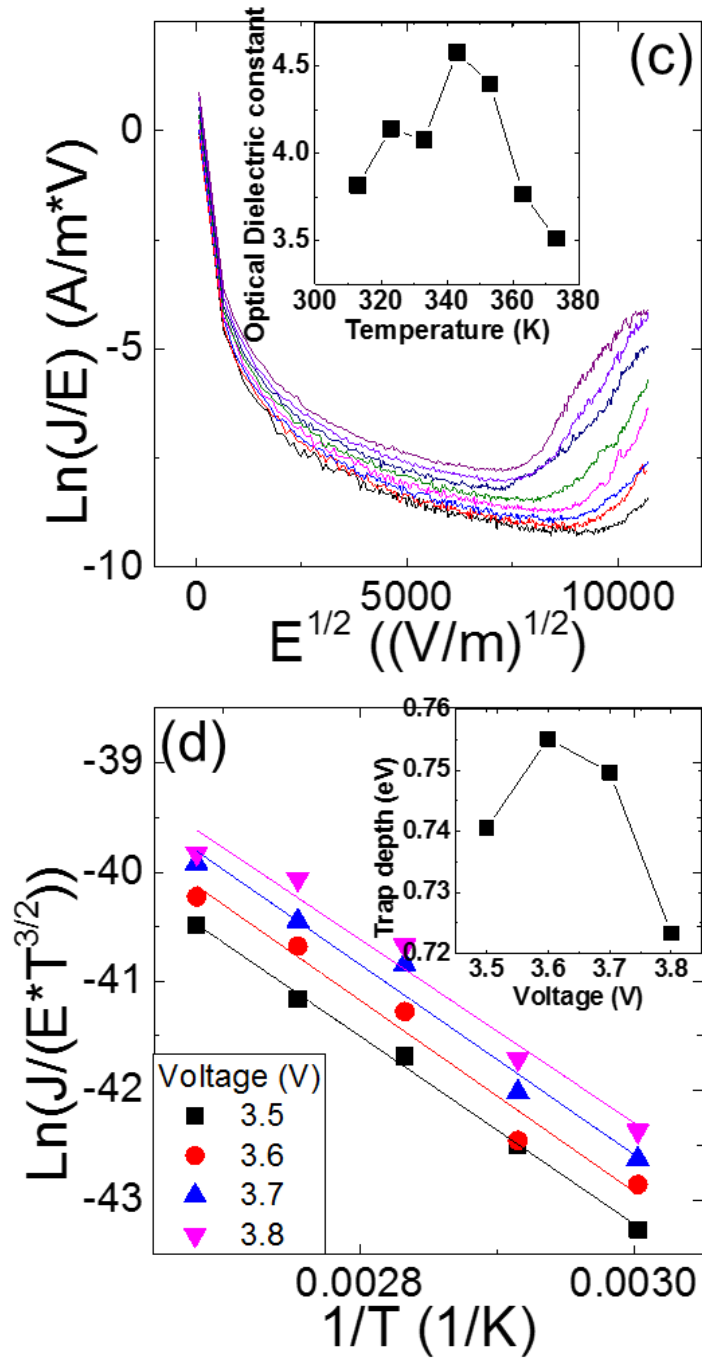


Figure 4. 10. (a) I-V curves of the HRS samples measured at different temperatures ranging from 30 to 100°C. Arrhenius form ($\text{Ln } I$ vs. $1/T$) plot in (b) HRS, and (inset figures of (b)) activation energies (E_a) extracted at each

voltage from the best-linear-fitting of the data in HRS. (c) P-F fitting and (d) the plots in the form of $\ln(I/(E \cdot T^{3/2}))$ vs. $1/T$ according to the P-F equation for the voltages ranging from 3.5 to 3.8 V in HRS. (inset figure of (c)) dielectric constant at each temperature and (inset figure of (d)) Activation energy, corresponding to the trap depth at each voltage in HRS.

Similar conduction mechanism fitting could be made for the LRS, which showed the suitability of the hopping conduction mechanism. **Figure 4.11a** shows the $\ln I - \ln V$ curves of the LRS measured at different temperatures ranging from 50 to 90°C and the slope is close to the value ~ 1 at each temperature. The voltage shown on the x axis of figure 4.11a is the value dropped to the Ta_2O_5 layer, which is also calculated from the above two capacitors model. Arrhenius plot ($\ln(J)$ vs. $1/T$) at 5-6 V and extracted E_a , which is small value ~ 0.157 eV, are shown in **figure 4.11b** and inset figure, respectively. These results suggest that LRS current is actually governed by Ta_2O_5 layer and flowed through the trap sites for hopping conduction in Ta_2O_5 . It is evident that the distinctive self-limited (-compliance) RS behavior is originated from the Ta_2O_5 that acts as an external resistor, which is intact while switching operation is repeated. The current conduction which follows the specific current conduction mechanism changes depending on the state; In HRS, current is flowed through the traps in HfO_2 layer following the P-F conduction. In LRS, on the other hand, P-F conduction is vanished and

hopping conduction in Ta₂O₅ govern the current flow.

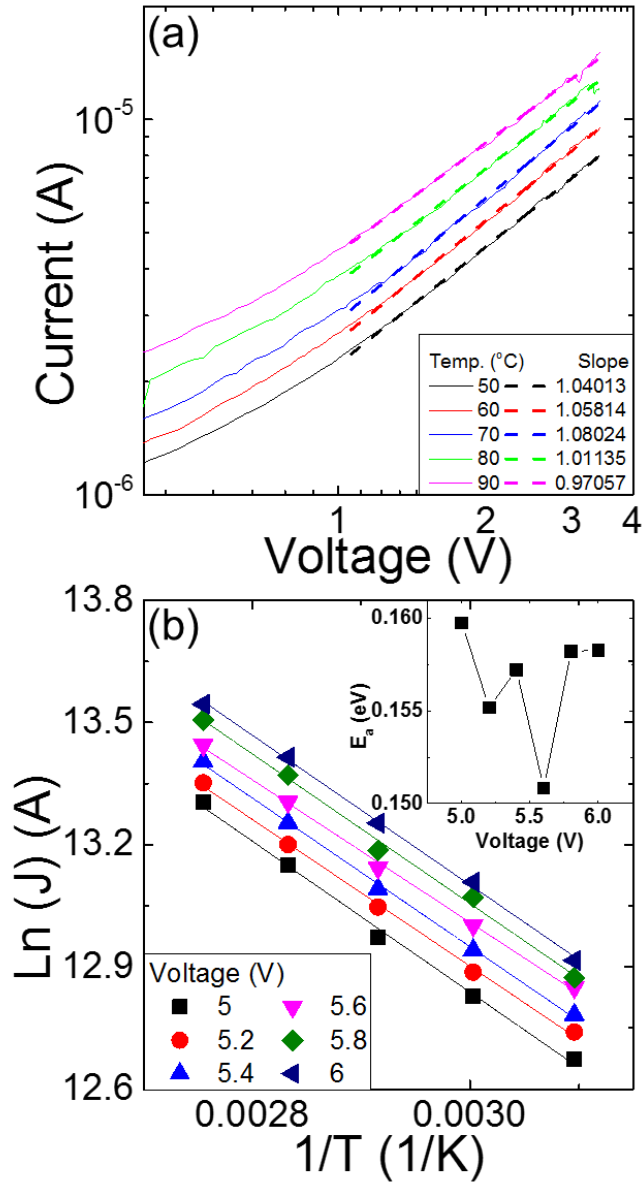


Figure 4. 11. (a) I-V curves of the LRS samples measured at different temperatures ranging from 50 to 90°C. Arrhenius form (Ln I vs. 1/T) plot in (b) LRS, and (inset figures of (b)) activation energies (E_a) extracted at each voltage from the best-linear-fitting of the data in LRS

Conduction mechanism analysis was similarly attempted, when negative bias voltage is induced, as shown in **figure 4.12a**. Figure 4.12a shows the I - absolute V curves measured at different temperature ranging from 110 to 150°C. The current was suppressed in a whole voltage region, and voltage region $> -8\text{V}$ shows hopping conduction having the activation energy $\sim 0.15\text{eV}$ obtained from the slopes of the best-linear-fitting of Arrhenius plot graph (not shown here). Also, the slope of $\log I - \log V$ is close to the value ~ 1 , suggesting that trap-assisted hopping conduction through traps in HfO_2 layer govern the current conduction. In low-voltage region (high absolute-voltage region), on the other hand, current increase rate is quite higher. Various thermally activated current conduction system is attempted to confirm the desirable conduction system. Any other conduction systems did not fit well with the result except schottky emission conduction fitting. $\ln(J/T^2)$ was plotted vs. $1/T$ at voltages ranging from 8 to 8.5V (**Figure 4.12b**). Slopes of the best-linear-fit graphs at each voltage could be represented by $\psi_0 - \beta_s E^{1/2}$ from the schottky emission equation. $\psi_0 - \beta_s E^{1/2}$ values were plotted vs. $E^{1/2}$ in the inset figure in figure 4.12b. ($\psi_0 - \beta_s E^{1/2}$, where ψ_0 and β_s are the zero-field Schottky barrier height and Schottky coefficient, which is determined by the optical dielectric constant) These values, which are optical dielectric constant from slope and Schottky barrier height from y-intercept value, are ~ 4.36 and $\sim 0.69\text{eV}$, respectively. Of course, the electric field E, which is applied to the Ta_2O_5 layer, is calculated using two capacitors model. This optical dielectric constant value is quite reasonable considering the estimated value with the

refractive index (~ 2.0) of Ta_2O_5 from the ellipsometry. Although the schottky barrier height value is somewhat smaller than the ideal values estimated considering the intrinsic properties of Pt and Ta_2O_5 , 0.69eV is quite sufficient value that give this device self-rectification. These results suggest that relatively higher schottky barrier at the Pt/ Ta_2O_5 is remained intact while RS operation is repeated and the current when negative bias voltage is induced is highly suppressed in the whole voltage region.

The above estimations unveil the switching mechanism in this material system. In positive bias region, the current flows through the hopping trap sites in low-voltage region and the bulk traps having depth of 0.75eV in high-voltage region in HRS. The identification of trap level (0.75eV) and its area-dependent HRS resistance revealed that the current is flowed through not localized paths but whole area. In LRS, on the other hand, the hopping conduction through the hopping trap sites in Ta_2O_5 govern the current conduction and non-area-dependence suggests that spatially localized related with the several areas along the grain boundaries or defects of the crystallized HfO_2 is the current path. In negative bias region, the whole leakage current is highly suppressed by the schottky barrier at Pt/ Ta_2O_5 , and it gives the device self-rectification property. Furthermore, the whole states are induced from the change in the charge state of the electron traps and whole switching system is led by only pure electronic mechanism. This is the strong point of this device suggesting the reason which elucidate the highly uniform RS behavior and electroforming-free property.

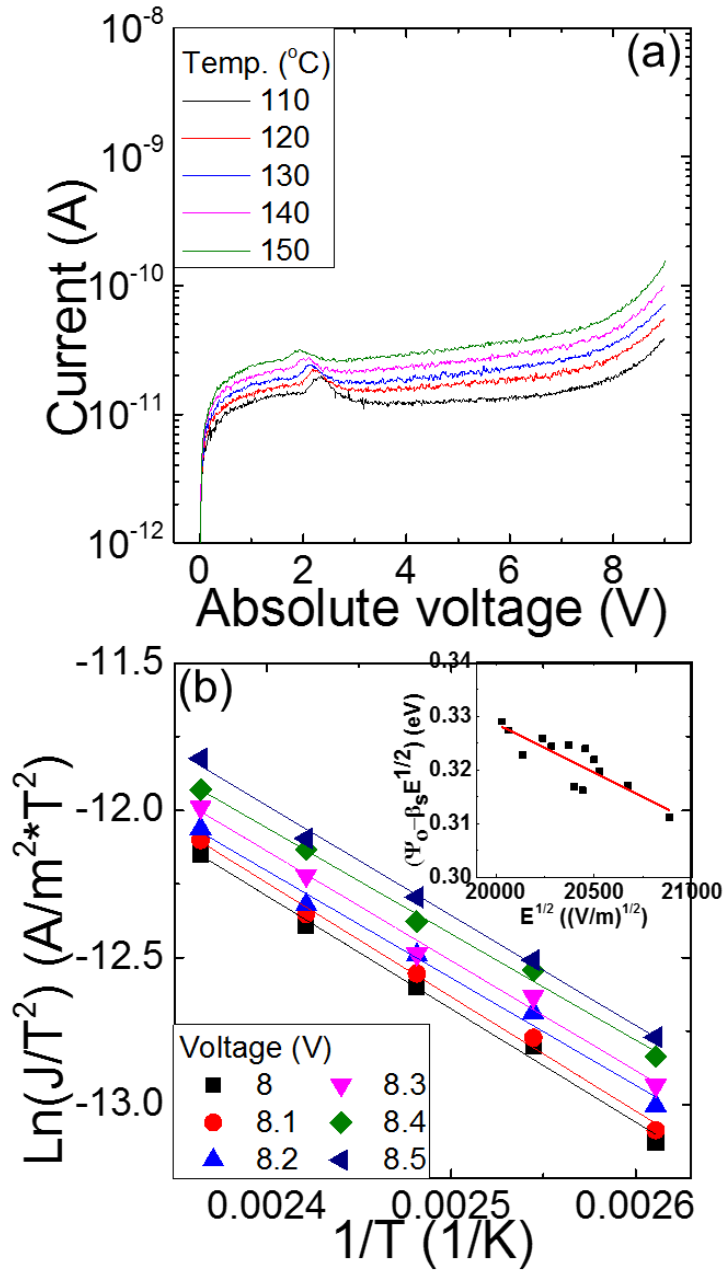


Figure 4. 12. (a) I-V curves and under a negatively biased condition measured at different temperatures ranging from 110 to 150°C. (b) Schottky type form $\text{Ln}(J/T^2)$ vs. $1/T$ plot at voltages ranging from 8 to 8.5 V. (Inset figure of (c)) $\Psi_0 - \beta_s E^{1/2}$ values plotted as a function of $E^{1/2}$

4.6. Summary

In this work, four successful outcomes are reported. First, a desirable structure Pt/Ta₂O₅/HfO₂/Ti that achieving a highly uniform, electroforming-free, self-limited and self-rectifying RS memory device is fabricated. Simple two-layered capacitor type structure is a strong candidate which fits perfectly to apply this structure to the cross-bar array or 3D vertical type ReRAM. Second, new feasible operation method prompted not conventional bipolar RS which is occurred by ionic switching mechanism but just electronic switching which is elucidated by the changing of charge states. Third, each states and its operation is easily understood through analysis of current conduction mechanism that govern the current flow. Last thing is the self-rectifying RS property with drastically improved on/off and F/R ratio and decreased operation voltage. The present combination of the Ta₂O₅ and HfO₂ layers, which were in contact with the Pt and Ti, respectively, is the most appropriate structure for achieving the feasible self-rectifying RS system. From previous study, scaling voltage and widening the on/off and F/R window for storage memory are the impending tasks to solve. It could be nicely resolved by using Ti as BE which influenced on the chemical states of HfO₂ layer and formed stable (quasi-) ohmic contact at HfO₂/Ti. Consequently, The magnitude of operation voltage is drastically decreased and the on/off and F/R ratio is also larger as the current level of LRS is increased. The result can be competitive with the conventional ReRAM device and even flash memory devices.

4.7. Bibliography

- [1] G. H. Kim, et al., *Adv. Funct. Mater.*, **2012**, 23, 1440-1449.
- [2] J. H. Yoon, et al., *Adv. Funct. Mater.*, **2013**, 24, 5086-5095.
- [3] S. F. Ho, S. Contarini, and J. W. Rabalais, *J. Phys. Chem.*, **1987**, 91, 4779
- [4] J. Lim, B. Oh, W. Lee, K. Lee, H. Na, B. Kim, D. Seo, J. Han and J. Hwang, *Appl. Phys. Lett.*, **2009**, 95, 123503.
- [5] C. B. Lee, et al., *IEEE Electron Device Letters*, **2011**, 32, 399-401.
- [6] J. L. Gavartin, D. Munoz Ramo, A. L. Shluger, G. Bersuker and B. H. Lee, *Appl. Phys. Lett.*, **2006**, 89, 082908.

5. Conclusions

In this work, two feasible methods to solve two most important problems of present ReRAM are proposed. In order to improve the non-uniformity problem of the switching performance originated from the random formation of CFs, Ru NDs which acts as an electric field concentrator or suppressor depending on the location are embedded in TiO₂ film and thus improved uniformity. Also, unprecedented concept of ReRAM structure having bi-layered insulator structure composed of HfO₂ (RS layer) and Ta₂O₅ (rectification layer) which is suitable for the 3D type planar or vertical CBA structure device with excellent uniformity, electroforming-free and self-rectification functionality is presented.

In chapter 2, the RS memory cells consisting of TiO₂ film and Pt electrodes (metal-insulator-metal (MIM) configuration) with the configurations of a planar capacitor and crossbar arrays are fabricated. In order to control the locations where the CFs are formed and achieve different phases of the TiO₂ film (anatase or rutile), Ru nano-dots (Ru-ND) with varying sizes and densities are embedded in the film at two different positions along the film thickness direction. All the functional films and NDs were grown by atomic layer deposition (ALD). It was found that embedded Ru-NDs greatly improved the RS uniformity. The electrode area also played a certain role, but it was relatively minor. Also, it was clarified, in this work, that the phases of

TiO₂ barely had any control over the RS performance, meaning that the geometry effect, i.e. confining the CF formation to a certain limited area, overwhelms the RS performance by changing the density and location of the Ru-NDs along the TiO₂ film thickness direction. Depending on their locations relative to the cathode interface, the role of Ru-NDs changes from field-enhancer to field-suppressor. It must be noted that continuous intermediate metal layer cannot play such a role, so that nano-scale dots are necessary for this purpose. A similar improvement could be expected from other types of metal NDs as long as they can be embedded in an appropriate shape and density as in this work. The development of memory cell structure of truly nano-scale size having such a limiting factor for the electric-field distribution can solve the non-uniformity issue of future ReRAM.

The implementation of new concept of RS structure cell is also a crucial point in this work. A feasible method of achieving a highly uniform, electroforming-free, multi-level switching and self-rectifying RS memory cell is presented in chapter 3 and 4. The method can be generally stated as having a two-layered dielectric structure, where one layer (in this case, HfO₂) works as the resistance switching layer by trapping and detrapping the trap sites while the other dielectric layer (in this case, Ta₂O₅) remains intact during the whole switching cycle and creates a high Schottky barrier with a high-work-function metal (in this case, Pt) to constitute the rectifying functionality. In addition, the RS layer should have a lower dielectric constant compared with the rectifying oxide layer for the effective application of the integral part of

the voltage over the RS layer. In addition, the energy gap of the RS layer should be higher than that of the rectifying oxide layer to ensure that the carrier transport in the forward (or switching) bias polarity will not be disturbed by the conduction band offset between the two dielectric layers.

The present combination of the Ta₂O₅ and HfO₂ layers, which were in contact with the Pt and TiN, Ti electrode, respectively, nicely fitted the above-mentioned conditions for achieving the desired multitude of functionality from one RS system. In addition, the appropriate deoxidation effect of the PEALD process for Ta₂O₅ on the underlying HfO₂, while the deoxidation effect on Ta₂O₅ itself was minimized by the optimized process conditions, made the HfO₂ have just enough density of oxygen vacancies to induce the fluent RS within the layer. With all these optimized structure and operation conditions for the given structure, excellent RS uniformity and electroforming-free and self-rectifying functionality could be simultaneously achieved from the Pt/Ta₂O₅/HfO₂/TiN, Pt/Ta₂O₅/HfO₂/Ti structure, which could be attributed to the electronic switching mechanism, where the disturbance by the uncontrolled ion migration could be largely suppressed.

Curriculum Vitae

Jung Ho Yoon

Dielectric Thin Film Laboratory

E-mail: yjh1309@snu.ac.kr

Department of Materials Science and Engineering

Tel.: +82-2-880-8643

Seoul National University

Fax: +82-2-880-8643

Seoul, Korea

I. Educations

2006. 03. - 2010. 02. B.S., Department of Materials Science and Engineering

Seoul National University, Seoul, Korea

2010. 03. - 2015. 02. M.S. & Ph. D. course, Department of Materials Science and

Engineering, Seoul National University, Seoul, Korea

II. RESEARCH AREAS

1. Atomic layer deposition of resistive switching materials for non-volatile resistive switching memories

- Depositing oxide thin films and optimizing the property of TiO_2 and HfO_2 oxide thin film for resistive switching memory.
- Deposition of metal (Ru) nano-dots using ALD for improving and analyzing resistive switching behavior in TiO_2 .

2. Device fabrication and analyzing mechanisms of resistive switching behavior

- Fabrication and Analysis of oxide resistive switching memory doped by metal nano-dots.
- Fabrication and characterization of cross-bar array structure resistive switching memory devices.
- Fabrication and characterization of vertical structure resistive switching memory devices.

3. Development and characterization of self-rectifying resistive switching device

- Fabrication and characterization of two-layered dielectric structure ($\text{Ta}_2\text{O}_5/\text{HfO}_2$, $\text{TiO}_2/\text{HfO}_2$) for self-rectifying resistive switching device.
- Analyzing conduction mechanisms of two-layered self-rectifying resistive switching device.

III. RESEARCH DESCRIPTIONS

1. Improving resistive switching parameters and analyzing resistive switching behavior

The research is mainly focused on the improving uniformity in the resistive switching (RS) parameters of TiO_2 thin films by inserting Ru nano-dots and controlling the formation of conducting filaments.

The understanding of RS mechanisms in many oxide materials and its application to resistance switching random access memory (ReRAM) have been greatly improved over the last decade. This has been attributed to the improvement in the device fabrication methods and application of various state-of-the-art analysis techniques. But there are still several key concerns remaining with RS materials in addition to device integration and architecture issues, including inappropriate repeatability of the RS parameters and insufficient endurance, which are material-property-related problems. The possible influence of various crystallographic phases of the oxide materials on the RS performance has not been clarified either.

The substantial improvement in the RS uniformity of TiO₂ memory cells was achieved by adopting Ru NDs embedded in the TiO₂ layer. It was concluded that limiting the location where electron injection occurs at the cathode interface to a narrower region was the key factor for achieving highly improved RS performance, which can be achieved by including the Ru-NDs. However, depending on their locations relative to the cathode interface, the role of Ru-NDs changes from field enhancer to field-suppressor. It must be noted that continuous intermediate metal layer cannot play such a role, so that nano-scale dots are necessary for this purpose. The phases of TiO₂ can hardly influence the RS performances. Therefore, a similar improvement could be expected from other types of metal NDs as long as they can be embedded in an appropriate shape and density. The development of memory cell structure of truly nanoscale size having such a limiting factor for the electric-field distribution can solve the non-uniformity issue of future ReRAM. The detailed research result is published in *Advanced Materials*. (*Advanced Materials*, 25, 1987-

1992 (2013))

2. Development of self-rectifying resistive switching device

The research is mainly focused on the developing self-rectifying resistive switching memory for cross-bar array and vertical structure memory.

ReRAM is attracting a great deal of attention as one of the most promising next-generation non-volatile memory devices especially in the crossbar array (CBA) configuration. It currently has several obstacles to overcome, however, such as the high variability in electrical performances, the requirement of an electroforming step, and the necessary integration of a memory cell with selector devices to alleviate the sneak currents in CBA. These problems become even more serious when a vertical type resistive switching memory. Therefore, the development of a RS memory cell that simultaneously contains rectification functionality in itself (self-rectification), highly reproducible RS performance, and electroforming-free characteristics is an impending tasks.

A two-layered dielectric structure consisting of HfO₂ and Ta₂O₅ layers, which are in contact with the TiN and Pt electrode, is presented for achieving these tasks simultaneously in one simple configuration. The HfO₂ layer works as the resistance switching layer by trapping and detrapping of electronic carriers, whereas the Ta₂O₅ layer remains intact during the whole switching cycle, which provides the rectification. With the optimized structure and operation conditions for the given materials, excellent RS uniformity, electroforming-free, and self-rectifying functionality could be simultaneously achieved from the Pt/Ta₂O₅/HfO₂/TiN

structure. And this recent work was published in Advanced Functional Materials.

(Advanced Functional Materials, DOI: 10.1002/adfm.201400064 (2014))

The ongoing research scope includes improving resistive switching property of two-layered type self-rectifying resistive switching memory and fabrication and characterization of vertical type resistive switching memory device.

IV. TECHNICAL SKILLS

1. Deposition methods

- Thermal ALD and plasma-enhanced ALD for resistive switching materials (TiO₂, HfO₂, Ta₂O₅, Al₂O₃)
- Thermal ALD for metal nano-dots (Ru)
- E-beam evaporation for metal electrode (Pt, Al, Au, Ti, W, Cr)

2. Device fabrication methods

- MA6-II aligner for photolithography (ultra violet)
- Wet etching and cleaning system
- Reactive ion etching system

3. Analysis methods

Direct operation and data analysis

- Atomic Force Microscopy (AFM, JEOL, JSPM-5200) for analysis of the topography

- Spectroscopic Ellipsometer (SE, J.A. Woollam, M-2000) for analysis of optical properties of thin films
- X-Ray Fluorescence Analyzer (XRF, Thermo scientific, ART Quant'X EDXRF) for analysis of composition and layer density of film
- X-ray Diffractometer (PANalytical, X'Pert PRO MPD) for measurement of X-ray diffraction and X-ray reflection
- Pulse/pattern generator (Agilent, 81110A/81111A) and digital oscilloscope for pulse switching measurement of resistive switching memory cell
- HP4194A for C-V and impedance measurement of capacitors
- HP4145B, 4155A for I-V measurement of resistive switching devices
- Four-point probe with heating stage (4PP, Lap-made) for real-time resistivity-temperature measurement

Indirect operation and data analysis

- Auger Electron Spectroscopy (AES, Perkin-Elmer, PHI 660) for analysis of composition of film
- Focused Ion Beam etching (FIB, SII NanoTechnology, SMI3050SE) for fabrication of TEM specimen
- Transmission Electron Microscopy (TEM, Technai, F20) for imaging and local composition analysis by energy dispersive spectroscopy (EDS)
- Transmission Electron Microscopy (TEM, JEOL, JEM-3000F, JEM-2100F) for imaging
- X-ray photoelectron spectroscopy (XPS, Thermo VG scientific, Sigma

probe) for chemical analysis

V. WORK EXPERIENCES

- “Development of a mass production compatible capacitor for next generation DRAM sponsored by the Korea Ministry of Knowledge and Economy”, **2010. 03 - 2012. 02**
- “Development of novel 3D stacked devices and core materials for next generation flash memory sponsored by the Korea Ministry of Knowledge and Economy”, **2010. 03 – (present)**
- “Fabrication and characterization of functional electronic thin films through molecular manipulation technology sponsored by the Ministry of Education, Science and Technology”, **2010. 07 – 2014. 06**
- “Development of Precursor and ALD process for PRAM and ReRAM devices, the National Research Program for the Nano Semiconductor Apparatus Development sponsored by the Korea Ministry of Knowledge and Economy, the Convergent Research Center program”, **2011. 11 – 2012. 10**
- “Future memories free from scaling limitation, Global Research Laboratory Program of National Research Foundation of Korea funded by Ministry of Education, Science and Technology”, **2012. 08 – (present)**

List of publications

1. Refereed Journal Articles (SCI)

1.1 Domestic

1.2. International

1. **Jung Ho Yoon**, Seul Ji Song, Sijung Yoo, Jun Yeong Seok, Kyung Jean Yoon, Dae Eun Kwon, Tae Hyung Park, Young Jae Kwon and Cheol Seong Hwang, "Highly Uniform, Electroforming-Free, Self-limited and Self-Rectifying Resistive Memory in the Pt/Ta₂O₅/HfO_{2-x}/Ti Structure" in preparation.
2. **Jung Ho Yoon**, Seul Ji Song, Il-Hyuk Yoo, Jun Yeong Seok, Kyung Jean Yoon, Dae Eun Kwon, Tae Hyung Park and Cheol Seong Hwang, "Highly Uniform, Electroforming-Free, and Self-Rectifying Resistive Memory in the Pt/Ta₂O₅/HfO_{2-x}/TiN Structure", Advanced Functional Materials, DOI: 10.1002/adfm.201400064 (2014)
3. Jun Yeong Seok, Seul Ji Song, **Jung Ho Yoon**, Kyung Jean Yoon, Tae Hyung Park, Dae Eun Kwon, Hyungkwang Lim, Gun Hwan Kim, Doo Seok Jeong, and Cheol Seong Hwang, "A Review of Three-Dimensional Resistive Switching Cross-Bar Array Memories from the Integration and Materials Property Points of View", Advanced Functional materials, DOI: 10.1002/adfm.201303520 (2014)
4. Ji-Wook Yoon, **Jung Ho Yoon**, Jong-Heun Lee, and Cheol Seong Hwang, "Impedance spectroscopic analysis on effects of partial oxidation of TiN

- bottom electrode and microstructure of amorphous and crystalline HfO₂ thin films on their bipolar resistive switching", *Nanoscale*, 6, 6668 (2014)
5. Kyung Jean Yoon, Seul Ji Song, Jun Yeong Seok, **Jung Ho Yoon**, Tae Hyung Park, Dae Eun Kwon and Cheol Seong Hwang, "Evolution of the shape of the conducting channel in complementary resistive switching transition metal oxides", *Nanoscale*, 6, 2161-2169 (2014)
 6. Seul Ji Song, Jun Yeong Seok, **Jung Ho Yoon**, Kyung Min Kim, Gun Hwan Kim, Min Hwan Lee and Cheol Seong Hwang, "Real-time identification of the evolution of conducting nano-filaments in TiO₂ thin film ReRAM", *Scientific reports*, 3, 3443 (2013)
 7. **Jung Ho Yoon**, Jeong Hwan Han, Ji Sim Jung, Woojin Jeon, Gun Hwan Kim, Seul Ji Song, Jun Yeong Seok, Kyung Jean Yoon, Min Hwan Lee and Cheol Seong Hwang, "Highly Improved Uniformity in the Resistive Switching Parameters of TiO₂ Thin Films by Inserting Ru Nanodots", *Advanced Materials*, 25, 1987-1992 (2013)
 8. Gun Hwan Kim, Jong Ho Lee, Youngbae Ahn, Woojin Jeon, Seul Ji Song, Jun Yeong Seok, **Jung Ho Yoon**, Kyung Jean Yoon, Tae Joo Park, and Cheol Seong Hwang, "32x32 Crossbar Array Resistive Memory Composed of a Stacked Schottky Diode and Unipolar Resistive Memory", *Adv. Funct. Mater.* 23, 1440-1449, (2013)
 9. Kyung Jean Yoon, Seul Ji Song, Jun Yeong Seok, **Jung Ho Yoon**, Gun Hwan Kim, Jong Ho Lee and Cheol Seong Hwang, "Ionic bipolar resistive switching modes determined by the preceding unipolar resistive switching reset behavior

- in Pt/TiO₂/Pt", Nanotechnology, 24, 145201 (2013)
10. Seul Ji Song, Sang Woon Lee, Gun Hwan Kim, Jun Yeong Seok, Kyung Jean Yoon, **Jung Ho Yoon**, Cheol Seong Hwang, Julien Gatineau, and Changhee Ko, " Substrate Dependent Growth Behaviors of Plasma-Enhanced Atomic Layer Deposited Nickel Oxide Films for Resistive Switching Application", Chem. Mater., 24, 4675-4685, (2012)
 11. Woo Young Park, Min Hyuk Park, Jong Ho Lee, **Jung Ho Yoon**, Jeong Hwan Han, Jung-Hae Choi and Cheol Seong Hwang, "Strain evolution of each type of grains in poly-crystalline (Ba,Sr)TiO₃ thin films grown by sputtering", Scientific Reports, 2, 939 (2012)
 12. Gun Hwan Kim, Jong Ho Lee, Woojin Jeon, Seul Ji Song, Jun Yeong Seok, **Jung Ho Yoon**, Kyung Jean Yoon, Tae Joo Park, and Cheol Seong Hwang, "Optimization of Chemical Structure of Schottky-Type Selection Diode for Crossbar Resistive Memory", ACS Appl. Mater. Interfaces, 4, 5338 (2012)
 13. Seong Keun Kim, Sora Han, Woojin Jeon, **Jung Ho Yoon**, Jeong Hwan Han, Woongkyu Lee, and Cheol Seong Hwang, "Impact of Bimetal Electrodes on Dielectric Properties of TiO₂ and Al-Doped TiO₂ Films", ACS Appl. Mater. Interfaces, 4, 4726 (2012)
 14. Deok-Yong Cho, Hyung Suk Jung, Il-Hyuk Yu, **Jung Ho Yoon**, Hyo Kyeom Kim, Sang Young Lee, Sang Ho Jeon, Seungwu Han, Jeong Hwan Kim, Tae Joo Park, Byeong-Gyu Park, and Cheol Seong Hwang, "Stabilization of Tetragonal HfO₂ under Low Active Oxygen Source Environment in Atomic Layer Deposition", Chem. Mater. 3534 (2012)

15. Gun Hwan Kim, Jong Ho Lee, Jeong Hwan Han, Seul Ji Song, Jun Yeong Seok, **Jung Ho Yoon**, Kyung Jean Yoon, Min Hwan Lee, Tae Joo Park, and Cheol Seong Hwang, "Schottky diode with excellent performance for large integration density of crossbar resistive memory", *Appl. Phys. Lett.*, 100, 213508 (2012)
16. Kyung Jean Yoon, Min Hwan Lee, Gun Hwan Kim, Seul Ji Song, Jun Yeong Seok, Sora Han, **Jung Ho Yoon**, Kyung Min Kim and Cheol Seong Hwang, "Memristive tri-stable resistive switching at ruptured conducting filaments of a Pt/TiO₂/Pt cell", *Nanotechnology*, 23, 185202 (2012)
17. Jun Yeong Seok, Gun Hwan Kim, Jeong Hwan Kim, Un Ki Kim, Yoon Jang Chung, Seul Ji Song, **Jung Ho Yoon**, Kyung Jean Yoon, Min Hwan Lee, Kyung Min Kim, and Cheol Seong Hwang, "Resistive Switching in TiO₂ Thin Films Using the Semiconducting In-Ga-Zn-O Electrode", *Electron Device Letters*, 33, 582-584 (2012)
18. Gun Hwan Kim, Jong Ho Lee, Jun Yeong Seok, Seul Ji Song, **Jung Ho Yoon**, Kyung Jean Yoon, Min Hwan Lee, Kyung Min Kim, Hyung Dong Lee, Seung Wook Ryu, Tae Joo Park, and Cheol Seong Hwang, "Improved endurance of resistive switching TiO₂ thin film by hourglass shaped Magneli filaments", *Appl. Phys. Lett.*, 98, 262901 (2011)
19. Kyung Min Kim, Byung Joon Choi, Min Hwan Lee, Gun Hwan Kim, Seul Ji Song, Jun Yeong Seok, **Jung Ho Yoon**, Seungwu Han and Cheol Seong Hwang, "A detailed understanding of the electronic bipolar resistance switching behavior in Pt/TiO₂/Pt structure" , *Nanotechnology*, 22 , 254010

(2011)

20. Kyung Min Kim, Seul Ji Song, Gun Hwan Kim, Jun Yeong Seok, Min Hwan Lee, **Jung Ho Yoon**, Jucheol Park, and Cheol Seong Hwang, "Collective Motion of Conducting Filaments in Pt/n-Type TiO₂/p-Type NiO/Pt Stacked Resistance Switching Memory", *Adv. Funct. Mater.*, 21, 1587–1592 (2011)
21. Min Hwan Lee, Kyung Min Kim, Seul Ji Song, Sang Ho Rha, Jun Yeong Seok, Ji Sim Jung, Gun Hwan Kim, **Jung Ho Yoon**, and Cheol Seong Hwang, "Surface redox induced bipolar switching of transition metal oxide films examined by scanning probe microscopy", *Appl. Phys. A*, 102, 827 (2011)
22. **Jung Ho Yoon**, Kyung Min Kim, Min Hwan Lee, Seong Keun Kim, Gun Hwan Kim, Seul Ji Song, Jun Yeong Seok, and Cheol Seong Hwang, "Role of Ru nano-dots embedded in TiO₂ thin films for improving the resistive switching behavior", *Appl. Phys. Lett.*, 97, 232904 (2010)
23. Kyung Min Kim, Min Hwan Lee, Gun Hwan Kim, Seul Ji Song, Jun Yeong Seok, **Jung Ho Yoon**, and Cheol Seong Hwang, "Understanding structure-property relationship of resistive switching oxide thin films using a conical filament model", *Appl. Phys. Lett.*, 97, 162912 (2010).
24. Kyung Min Kim, Gun Hwan Kim, Seul Ji Song, Jun Yeong Seok, Min Hwan Lee, **Jung Ho Yoon** and Cheol Seong Hwang, "Electrically configurable electroforming and bipolar resistive switching in Pt/TiO₂/Pt structures", *Nanotechnology*, 21, 305203 (2010)
25. Min Hwan Lee, Seul Ji Song, Kyung Min Kim, Gun Hwan Kim, Jun Yeong Seok, **Jung Ho Yoon**, and Cheol Seong Hwang, "Scanning probe based

observation of bipolar resistive switching NiO films", Appl. Phys. Lett., 97, 062909 (2010)

26. Min Hwan Lee, Kyung Min Kim, Gun Hwan Kim, Jun Yeong Seok, Seul Ji Song, **Jung Ho Yoon**, and Cheol Seong Hwang, "Study on the electrical conduction mechanism of bipolar resistive switching TiO₂ thin films using impedance spectroscopy", Appl. Phys. Lett. 96, 152909 (2010).

2. CONFERENCES

2.1 Domestic

1. Dae Eun Kwon, Jong Ho Lee , **Jung Ho Yoon**, Seul Ji Song, Kyung Jean Yoon, Tae Hyung Park, Tae Joo Park and Cheol Seong Hwang, "S-Doped TiO₂ as a Selection Diode for ReRAM", Feb. 24-26, Seoul, Korea, 21th Korea semiconductor conference (2014)
2. **Jung Ho Yoon**, Seul Ji Song, Il.Hyuk Yoo, Jun Yeong Seok, Kyung Jean Yoon, Tae Eun Kwon, Tae Hyung Park, and Cheol Seong Hwang, "Highly Uniform, Electroforming-Free, and Self-Rectifying Resistive Memory in Pt/Ta₂O₅/HfO_{2-x}/TiN Structure" Feb. 24-26, Seoul, Korea, 21th Korea semiconductor conference (2014)
3. Kyung Jean Yoon, Seul Ji Song, Jun Yeong Seok, **Jung Ho Yoon**, Tae Hyung Park, Dae Eun Kwon, Cheol Seong Hwang, "Evolution of the Shape of the Conducting Channel in Complementary Resistive Switching Transition Metal Oxides" Feb. 24-26, Seoul, Korea, 21th Korea semiconductor conference (2014)
4. Taehyung Park, Seul Ji Song, Jun Yeong Seok, **Jung Ho Yoon**, Kyung Jean

- Yoon, Dae Eun Kwon, and Cheol Seong Hwang "Identification of Controlling Parameters on Self-Compliance Resistive Switching in a Pt/TaO_x/Ta₂O₅/Pt Structure", Feb. 24-26, Seoul, Korea, 21th Korea semiconductor conference (2014)
5. Kyung Jean Yoon, Seul Ji Song, Jun Yeong Seok, **Jung Ho Yoon**, Jong Ho Lee, and Cheol Seong Hwang, "Variation in the bipolar resistive switching behavior according to the former unipolar resistive switching reset in a Pt/TiO₂/Pt", Feb. 4-6, Korea, 20th Korea semiconductor conference (2013)
 6. Jun Yeong Seok, Gun Hwan Kim, Seul Ji Song, **Jung Ho Yoon**, Kyung Jean Yoon and Cheol Seong Hwang, "Resistive switching phenomena in binary oxide thin films with semiconducting In₂Ga₂ZnO₇ electrode", Feb. 4-6, Korea, 20th Korea semiconductor conference (2013)
 7. **Jung Ho Yoon**, Seul Ji Song, Jun Yeong Seok, Kyung Jean Yoon, Jong Ho Lee and Cheol Seong Hwang, "Self-rectifying resistive switching behavior in bi-layer structure based on HfO₂ thin film", Feb. 4-6, Korea, 20th Korea semiconductor conference (2013)
 8. Seul Ji Song, Kyung Jean Yoon, Jun Yeong Seok, **Jung Ho Yoon** and Cheol Seong Hwang, "Self-rectifying resistive switching behaviors in NiO/insulator stacked devices", Feb. 4-6, Korea, 20th Korea semiconductor conference (2013)
 9. Gun Hwan Kim, Jong Ho Lee, Jeong Hwan Han, Seul Ji Song, Jun Yeong Seok, **Jung Ho Yoon**, Kyung Jean Yoon, Min Hwan Lee, Tae Joo Park, and Cheol Seong Hwang, "Cross bar resistive memory using TiO₂ thin films", Feb.

- 15-17, Seoul, Korea, 19th Korea semiconductor conference (2012)
10. Jun Yeong Seok, Gun Hwan Kim, Seul Ji Song, **Jung Ho Yoon**, Kyung Jin Yoon, Min Hwan Lee, and Cheol Seong Hwang, "A novel cross-bar array scheme to suppress sneak path current in memory operation", Feb. 15-17, Seoul, Korea, 19th Korea semiconductor conference (2012)
 11. Kyung Jean Yoon, Min Hwan Lee, Gun Hwan Kim, Seul Ji Song, Jun Yeong Seok, **Jung Ho Yoon**, and Cheol Seong Hwang, "Memristive tri-stable resistive switching at ruptured conducting filaments of a Pt/TiO₂/Pt cell" Feb. 15-17, Seoul, Korea, 19th Korea semiconductor conference (2012)
 12. **Jung Ho Yoon**, Hyung Seok Jung, Min hwan Lee, Gun Hwan Kim, Seul Ji Song, Jun Yeong Seok, Kyung Jean Yoon, and Cheol Seong Hwang, "Resistive switching characteristics in HfO₂ thin films depending on the crystalline structure", Feb. 15-17, Seoul, Korea, 19th Korea semiconductor conference (2012)
 13. Gun Hwan Kim, Kyung Min Kim, Jun yeong Seok, Seul Ji Song, **Jung Ho Yoon**, and Cheol Seong Hwang, "Electrical endurance characteristic and conductive-atomic force microscopy study of resistance switching cross bar array structure", Feb. 16-18, 18th Korea semiconductor conference (2011)
 14. Seul Ji Song, Jun Yeong Seok, **Jung Ho Yoon**, Kyung Min Kim, Gun Hwan Kim, Min Hwan Lee and Cheol Seong Hwang, "Johnson-Mehl-Avrami type kinetic model for identifying the evolution of conducting nanofilaments in TiO₂ ReRAM" , Feb. 16-18, 18th Korea semiconductor conference (2011)
 15. Gun Hwan Kim, Kyung Min Kim, Jun yeong Seok, Seul Ji Song, **Jung Ho**

Yoon, and Cheol Seong Hwang, "A Review on Cross-bar Array Memory using Resistance Switching Thin Films", Feb. 16-18, 18th Korea semiconductor conference (2011)

2.2 International

1. **Jung Ho Yoon**, Jeong Hwan Han, Ji Sim Jung, Woojin Jeon, Gun Hwan Kim, Seul Ji Song, Jun Yeong Seok, Kyung Jean Yoon, Min Hwan Lee and Cheol Seong Hwang, "Highly Uniform, Electroforming-Free, and Self-Rectifying Resistive Memory in the Pt/Ta₂O₅/HfO_{2-x}/TiN Structure", May 26-30, Lille, France, 2014 E-MRS (2014)
2. Kyung Jean Yoon, Seul Ji Song, Jun Yeong Seok, **Jung Ho Yoon**, Tae Hyung Park, Dae Eun Kwon and Cheol Seong Hwang, "Evolution of the shape of the conducting channel in complementary resistive switching transition metal oxides", April 21-25, San Francisco, US, MRS SPRING MEETING & EXHIBIT (2014)
3. Seul Ji Song, Sang Woon Lee, Jun Yeong Seok, **Jung Ho Yoon**, Kyung Jean Yoon, Clement Lansalot, Chang Hee Ko, and Cheol Seong Hwang, "Atomic Layer deposition of Tantalum oxide film using Ta(N(C₄H₉))(C₅H₄)(N(C₂H₅)₂)₂ and plasma-activated H₂O", July 28-31, San Diego, US, ALD 2013 (2013)
4. Gun Hwan Kim, Jong Ho Lee, Youngbae Ahn, Woojin Jeon, Seul Ji Song, Jun Yeong Seok, **Jung Ho Yoon**, Kyung Jean Yoon, Tae Joo Park, and Cheol Seong Hwang*, "Crossbar array ReRAM composed of stacked Schottky diode and unipolar resistive memory", Dec 9-14, Pattaya, Thailand, The 8th Asian

Meeting on Ferroelectrics(AMF-8) (2012)

5. Gun Hwan Kim, Jong Ho Lee, Jeong Hwan Han, Seul Ji Song, Jun Yeong Seok, **Jung Ho Yoon**, Kyung Jean Yoon, and Cheol Seong Hwang, "Crossbar memory using TiO₂ thin film-based Schottky diode and unipolar switching cell", Oct. 7-12, Honolulu, Hawaii, ECS 2012 (2012)
6. Jun Yeong Seok, Gun Hwan Kim, Seul Ji Song, **Jung Ho Yoon**, Kyung Jin Yoon and Cheol Seong Hwang, "STUDY ON RESISTIVE SWITCHING OF BINARY OXIDE THIN FILMS USING SEMICONDUCTING In₂Ga₂ZnO₇ ELECTRODE", June 17-20, Aachen, Germany, Nature Conference 2012 (2012)
7. **Jung Ho Yoon**, Hyung-Suk Jung, Min Hwan Lee, Gun Hwan Kim, Seul Ji Song, Jun Yeong Seok, Kyung Jean Yoon and Cheol Seong Hwang, "RESISTIVE SWITCHING CHARACTERISTICS IN HfO₂ THIN FILMS DEPENDING ON THEIR CRYSTALLINE STRUCTURE", June 17-20, Aachen, Germany, Nature Conference 2012 (2012)
8. Kyung Jean Yoon, Seul Ji Song, Gun Hwan Kim, Jun Yeong Seok, **Jung Ho Yoon**, and Cheol Seong Hwang, "A STUDY UPON THE SWITCHING CHARACTERISTICS AT RUPTURED CONDUCTING FILAMENTS REGION IN A Pt/TiO₂/Pt MEMRISTIVE DEVICE", June 17-20, Aachen, Germany, Nature Conference 2012 (2012)
9. Seul Ji Song, Gun Hwan Kim, Jun Yeong Seok, Kyung Jean Yoon, **Jung Ho Yoon**, and Cheol Seong Hwang, "Bipolar resistive switching behaviors of plasma-enhanced atomic layer deposited NiO films on tungsten substrate",

June 17-20, Aachen, Germany, Nature Conference 2012 (2012)

10. Gun Hwan Kim, Jong Ho Lee, Jeong Hwan Han, Seul Ji Song, Jun Yeong Seok, **Jung Ho Yoon**, Kyung Jean Yoon, Min Hwan Lee, Tae Joo Park, and Cheol Seong Hwang, "Cross-bar resistive memory using TiO₂ thin film", Dec. 1-3, Arlington, US, 42nd IEEE Semiconductor Interface Specialists Conference (2011)
11. Seul Ji Song, Jun Yeong Seok, Kyung Min Kim, Gun Hwan Kim, Min Hwan Lee, **Jung Ho Yoon** and Cheol Seong Hwang, "Kinetic study on the formation and rupture of conducting nano-filaments in RRAM", July 31 - August 4, Cambridge, England, International Symposium on Integrated Functionalities(ISIF) 2011 (2011)
12. Kyung Jean Yoon, Seul Ji Song, Kyung Min Kim, Min Hwan Lee, Gun Hwan Kim, Jun Yeong Seok, **Jung Ho Yoon**, and Cheol Seong Hwang, "Memristive Switching utilizing the bipolar resistive switching in Titanium dioxide ", July 31 - August 4, Cambridge, England, International Symposium on Integrated Functionalities(ISIF) 2011 (2011)
13. **Jung Ho Yoon**, Kyung Min Kim, Min Hwan Lee, Seong Keun Kim, Ji Sim Jung, Gun Hwan Kim, Seul Ji Song, Jun Yeong Seok, and Cheol Seong Hwang, "Role of Ru nano-dots embedded in TiO₂ thin films for improving the resistive switching behavior", July 31 - August 4, Cambridge, England, International Symposium on Integrated Functionalities(ISIF) 2011 (2011)
14. Cheol Seong Hwang, Kyung Min Kim, Seul Ji Song, Gun Hwan Kim, Jun Yeong Seok, Min Hwan Lee, **Jung Ho Yoon**, and Jucheol Park, "Collective

- motion of nano-filaments in Pt/n-type TiO₂/p-type NiO/Pt stacked resistance switching memory", July 24-27, Vancouver, Canada, ISAF-PFM-2011 (2011)
15. Seul Ji Song, Gun Hwan Kim, Jun Yeong Seok, **Jung Ho Yoon**, Kyung Jean Yoon, Julien Gatineau and Cheol Seong Hwang, "Plasma enhanced atomic layer deposition of NiO thin films for resistive switching memory devices", June 26-29, Cambridge, England, ALD 2011 (2011)
 16. Minhwan Lee, Kyung Min Kim, **Jung Ho Yoon** and Cheol Seong Hwang, "Impedance Spectroscopy Observation for Examining Resistive Switching Mechanism in TiO₂ Thin Films.", April 7, San Francisco, US, MRS spring meeting 2010 (2010)

3. AWARDS & RESEARCH HIGHLIGHTS

1. 2011. 02. : "Role of Ru nano-dots embedded in TiO₂ thin films for improving the resistive switching behavior" - research highlights in Appl. Phys. Lett.
2. 2014. 04. : Excellent graduate student award from department of materials science and engineering in Seoul National University.
3. 2014. 09. : Excellent paper award from NCIRF in Seoul National University.

Abstract (in Korean)

저항변화 메모리는 확장성과 성능이 뛰어나고 저비용에 비교적 간단한 구조로 구현할 수 있다는 장점을 기반으로 하여 차세대 메모리 분야에서 가장 유력한 소자로 주목되었다. 하지만 근래의 괄목할만한 성능 개선과 동작 메커니즘 이해에도 불구하고, 몇 가지 해결해야 할 문제가 남아있는 실정이다. 그 중 대표적인 두 가지 문제는 다음과 같다. 하나는, 저항변화 동작에서의 균일성 문제이고 다른 하나는, 3D 구조의 평면 혹은 수직 크로스바 구조에 적합한 저항변화 메모리 구조를 구현하는 것이다.

최근 몇 년간 여러 종류의 산화물 박막에서의 저항변화 거동과 특성이 소자의 다양한 제작 방법의 개발과 여러 종류의 분석 기술을 바탕으로 하여 연구되었다. 그 중 이온의 이동에 의한 저항변화 거동 형태는 저항변화층에서 산소 공공 혹은 결함의 이동으로 형성되는 전도성을 가지는 나노 크기의 필라멘트에 의해 저항변화 특성이 나타난다는 것이 밝혀졌고, 이를 통해 저항변화 현상의 불균일성이 반복된 저항변화소자의 동작에서의 전도 필라멘트의 임의의 성장과 소멸에서 기인한다는 결과를 알 수 있었다. 즉, 이는 전도 필라멘트의 형성 영역을 특정하게 한정할 수 있다면 그 소자의 반복 동작의 불균일성을 해결할 수 있다는 것을 시사하는 것이다. 이 연구에서는 이러한 저항변화소자의 동작특성 불균일성을 해결하기 위한 방법으로 많은 연구가 진행된 대표적인

저항변화 물질인 TiO_2 내부에 Ru 나노닷을 삽입하여 불균일성 문제를 해결하고자 하였다. 결과적으로, Ru 나노닷의 TiO_2 내부에서의 두께 방향에서의 위치에 따라서 전자가 주입되는 음극에서의 전계 집중 및 분산 역할을 하는 것을 확인할 수 있었고 이를 이용해 저항변화 특성을 향상시킬 수 있었다. 전도성 필라멘트의 생성에 전자가 주입되는 위치는 매우 중요하고 Ru 나노닷의 위치에 따라 전계가 집중되는 영역을 한정할 수 있기에 결과적으로 전도성 필라멘트의 생성을 조절할 수 있게 되고 균일성 문제 및 특성을 향상시키는 결과를 유도할 수 있었다.

가장 널리 알려진 저항변화 소자의 형태인 크로스바 구조에서는 sneak 전류 문제를 해결하기 위해 메모리 소자의 전기적 특성 다양화에 따른 적합한 선택 소자를 찾고 접합하는 것이 당연한 과제로 생각되고 있었다. 이러한 문제는 3D 수직 구조 형태를 가지게 되면 점차 심화될 것으로 생각되었고, 이를 해결하기 위해 자가 정류 현상을 보이며 안정적 저항변화 거동을 보이고 electroforming 과정이 불필요하며 multi-level 동작이 가능한 소자를 개발이 필요성이 대두되었다. 이 연구에서는 서로 다른 유전체인 HfO_2 와 Ta_2O_5 를 적층하고 이를 각각 TiN, Ti를 하부전극으로 Pt를 상부전극으로 구성하여 필요한 모든 특성을 동시에 확보하였다. HfO_2 층은 저항변화층으로써 전자의 trapping과 detrapping에 의해 저항 상태 변화를 유도하였고, 동시에 Ta_2O_5 는 자가 정류 층으로써 Pt와의 계면에 형성된 Schottky barrier에 의해 반복된 동작에서도 누설 전류를 억제하는 작용을 하였다. 최적화된 구조에서 전자

이동에 의해서만 유도되는 이 Pt/Ta₂O₅/HfO₂/Ti, Pt/Ta₂O₅/HfO₂/TiN 소자에서의 저항변화 거동은 매우 균일한 저항변화 특성을 보이고 electroforming이 필요하지 않으며 multi-level 동작이 가능하며 자가 정류 특성을 얻을 수 있다.

주요어: 저항 변화 소자, 자가 정류 현상, 균일성, 크로스바 어레이, Ru 나노닷, Multi level 동작

학 번: 2010-20619

윤 정 호

